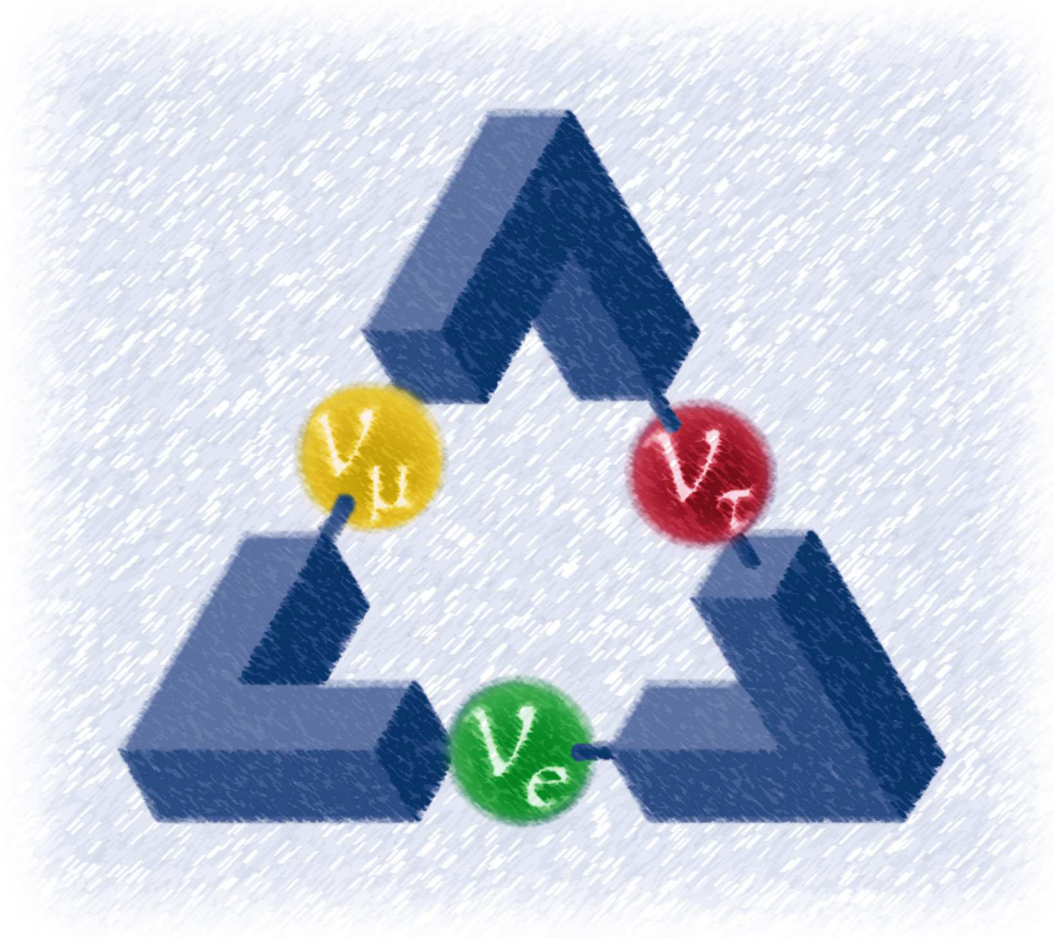


Joachim Kopp

# PHENOMENOLOGY OF THREE-FLAVOUR NEUTRINO OSCILLATIONS

Diploma Thesis

May 2006



Technische Universität München  
Physik-Department T30d  
Prof. Dr. Manfred Lindner



# Abstract

In this work, we study the phenomenology of three-flavour neutrino oscillations, focusing in particular on the prospects of future experiments. After introducing the theoretical formalism and giving an overview of the present status of the field, we discuss the generic three-flavour effects appearing in  $\nu_e \rightarrow \nu_e$ ,  $\nu_\mu \rightarrow \nu_e$ , and  $\nu_\mu \rightarrow \nu_\tau$  oscillations. We have performed detailed simulations of the reactor experiments **Double Chooz** and **Triple Chooz**, which show that these experiments are excellent tools for a measurement of the mixing angle  $\theta_{13}$ .

Furthermore, we have developed the simulation program **INSANE** (INstrument for the Simulation of Atmospheric Neutrino Experiments), which we use to study the potential of atmospheric neutrino experiments to further constrain the oscillation parameters. We propose to use the **ATLAS** experiment at LHC as a detector for atmospheric neutrinos during the shutdown periods of the accelerator. Making reasonable assumptions on the experimental parameters, we estimate that **ATLAS** can detect neutrino oscillations and set limits on the oscillation parameters, which are however slightly worse than those from **Super-Kamiokande**. Finally, we show that it is in principle possible to detect three-flavour effects in very large atmospheric neutrino experiments, but that such experiments can never compete with a dedicated accelerator setup.



# Contents

<b>1</b>	<b>Introduction</b>	<b>9</b>
<b>2</b>	<b>Theoretical framework of neutrino oscillations</b>	<b>11</b>
2.1	Neutrino oscillations in vacuum . . . . .	11
2.1.1	The two-flavour case . . . . .	14
2.1.2	The three-flavour case . . . . .	15
2.2	Neutrino oscillations in matter . . . . .	15
2.2.1	Derivation of the matter potential . . . . .	15
2.2.2	The two-flavour case . . . . .	17
2.2.3	The three-flavour case . . . . .	19
2.3	Mathematical properties of the oscillation probabilities . . . . .	21
2.3.1	Oscillation probabilities for antineutrinos . . . . .	21
2.3.2	Interdependencies of oscillation channels . . . . .	21
<b>3</b>	<b>Current status of neutrino oscillation physics</b>	<b>23</b>
3.1	The atmospheric oscillation parameters . . . . .	23
3.2	The solar oscillation parameters . . . . .	25
3.3	Three-flavour fits and future challenges . . . . .	26
3.4	Non-standard neutrino oscillations . . . . .	29
<b>4</b>	<b>The three-flavour neutrino oscillation probabilities</b>	<b>31</b>
4.1	The $\nu_e \rightarrow \nu_e$ channel . . . . .	32
4.2	The $\nu_\mu \rightarrow \nu_e$ channel . . . . .	33
4.2.1	Three-flavour effects in vacuum . . . . .	33
4.2.2	Three-flavour effects in matter of constant density . . . . .	34
4.2.3	CP violation in the $\nu_\mu \rightarrow \nu_e$ channel . . . . .	35
4.2.4	Matter of varying density and the PREM profile . . . . .	38
4.3	The $\nu_\mu \rightarrow \nu_\tau$ channel . . . . .	42
4.3.1	Three-flavour effects in vacuum . . . . .	42
4.3.2	Three-flavour effects in matter of constant density . . . . .	44

<b>5</b>	<b>Prospects of future neutrino oscillation experiments</b>	<b>47</b>
5.1	Reactor neutrinos . . . . .	47
5.1.1	Systematical errors . . . . .	47
5.1.2	Double Chooz and Triple Chooz . . . . .	53
5.2	Atmospheric neutrinos . . . . .	55
5.2.1	General discussion . . . . .	55
5.2.2	Simulation of atmospheric neutrino experiments . . . . .	57
5.2.3	Analysis of simulated atmospheric neutrino data . . . . .	68
5.2.4	Event distributions in Super-Kamiokande and ATLAS . . . . .	71
5.2.5	Physics potential of atmospheric neutrino experiments . . . . .	75
<b>6</b>	<b>Summary and conclusions</b>	<b>83</b>
<b>A</b>	<b>Numerical calculation of oscillation probabilities</b>	<b>85</b>
A.1	Constant matter density . . . . .	85
A.2	Varying matter density . . . . .	88
A.3	Comparison of the algorithms . . . . .	90
<b>B</b>	<b>Geometry of atmospheric neutrino detectors</b>	<b>93</b>
B.1	Calculation of the muon range in matter . . . . .	93
B.2	Angular efficiencies for contained events . . . . .	94
B.3	Efficiencies for upward going muon events in Super-Kamiokande . . . . .	97
B.4	Efficiencies for upward going muon events in ATLAS . . . . .	98
<b>C</b>	<b>Neutrino oscillations in the three-layer model of the earth</b>	<b>101</b>
	<b>Index</b>	<b>107</b>
	<b>Bibliography</b>	<b>113</b>

## Cosmic Gall

Neutrinos, they are very small.  
They have no charge and have no mass  
And do not interact at all.  
The earth is just a silly ball  
To them, through which they simply pass,  
Like dustmaids down a drafty hall  
Or photons through a sheet of glass.  
They snub the most exquisite gas,  
Ignore the most substantial wall,  
Cold-shoulder steel and sounding brass,  
Insult the stallion in his stall,  
And scorning barriers of class,  
Infiltrate you and me! Like tall  
And painless guillotines, they fall  
Down through our heads into the grass.  
At night, they enter at Nepal  
And pierce the lover and his lass  
From underneath the bed — you call  
It wonderful; I call it crass.

John Updike, 1960



# Chapter 1

## Introduction

When John Updike wrote his poem “Cosmic Gall” in 1960, 30 years after Pauli had postulated the neutrino, he could hardly have anticipated that now, 56 years later, neutrinos are one of the most active areas of research in particle physics. Since the neutrino has first been discovered experimentally in 1956 by C. Cowan and F. Reines, numerous experiments have studied the properties of neutrinos originating from nuclear reactors, from the sun, from cosmic rays interacting with the atmosphere, from particle accelerators, from radioactive decays inside the Earth, and from a supernova explosion. It has been confirmed that neutrinos exist in three flavours, corresponding to the three families of the standard model. They are named electron neutrino ( $\nu_e$ ), muon neutrino ( $\nu_\mu$ ), and tau neutrino ( $\nu_\tau$ ).

It has been a long standing mystery whether neutrinos have exactly vanishing masses, as suggested in Updike’s poem, or only very small, but finite, masses. The first indication that the latter might be true, came from solar neutrino experiments which observed less than the expected  $\nu_e$  flux. This deficit could be explained by the phenomenon of neutrino oscillations, i.e. periodic conversions between the three neutrino flavours, which are a purely quantum mechanical process and are only possible if the neutrino mass matrix in the flavour basis is not proportional to the unit matrix. However, at the time of the first solar neutrino experiments, many other possible explanations were imaginable as well. The mystery was finally solved when the Super-Kamiokande experiment in Japan observed oscillations of atmospheric neutrinos in 1998, and when SNO in Canada showed in 2000 that the “missing” solar  $\nu_e$  have indeed oscillated into other flavours.

Today, neutrino physics is entering the stage of precision measurements. Of particular interest is the search for so-called three-flavour effects, i.e. effects which do not appear in a model with only two neutrino flavours. For solar neutrinos, a model containing only  $\nu_e$  and  $\nu_\mu$  has been sufficient up to now, and atmospheric neutrino oscillations could be explained with only  $\nu_\mu$  and  $\nu_\tau$ . It is however clear that these approximations will cease to be valid at some point, and therefore many new experiments are being designed and constructed at the moment to detect three-flavour effects.

In this work, we will first introduce the formalism of neutrino oscillations in chapter 2, and then give an overview of the present knowledge about the oscillation parameters and of the most important future projects in chapter 3. In chapter 4 we will discuss the

three-flavour neutrino oscillation probabilities from a phenomenological point of view, focusing in particular on features which are relevant to future experiments. Chapter 5 will contain the results of detailed simulations of the reactor experiments **Double Chooz** and **Triple Chooz**, and of atmospheric neutrino experiments. In particular, we propose to use the **ATLAS** detector at **LHC** to detect atmospheric neutrinos during the shutdown periods of the accelerator. We will show that in spite of the low statistics that are achievable in **ATLAS**, the experiment can provide an independent confirmation of neutrino oscillations with a detector technology that has never been used for this purpose before. Furthermore, a measurement of the atmospheric oscillation parameters  $\theta_{23}$  and  $\Delta m_{31}^2$  is possible with an accuracy that is comparable to that of **Super-Kamiokande** for  $\Delta m_{31}^2$  at the  $1\sigma$  level, but worse for higher confidence levels and for  $\theta_{23}$ . We will also study the prospects of a search for three-flavour effects in atmospheric neutrino oscillations, and show that it is only possible in huge detectors, and can never compete with the precision of dedicated accelerator experiments. In chapter 6, we will summarize our results and present some conclusions. Appendix A is devoted to a discussion of numerical algorithms for the calculation of neutrino oscillation probabilities, and appendix B contains details about the geometry of the **Super-Kamiokande** and **ATLAS** detectors, which are important for a proper treatment of their reconstruction efficiencies. Appendix C contains an approximate analytical derivation of two-flavour neutrino oscillation probabilities in the Earth.

## Chapter 2

# Theoretical framework of neutrino oscillations

Neutrino propagation and interactions are contained in the leptonic part of the standard model Lagrangian [1]

$$\mathcal{L} = i\bar{\nu}_{jL}\partial^\mu\gamma_\mu\nu_{jL} + i\bar{\nu}_{jR}\partial^\mu\gamma_\mu\nu_{jR} - \bar{\nu}_{jL}m_{jk}\nu_{kR} - \bar{\nu}_{jR}(m^\dagger)_{jk}\nu_{kL} + \left[ \frac{g}{\sqrt{2}}\bar{e}_{jL}\gamma^\mu W_\mu^- U_{jk}^* \nu_{kL} + \frac{g}{4\cos\theta_W}\bar{\nu}_{jL}\gamma^\mu Z_\mu^0 \nu_{jL} + h.c. \right]. \quad (2.1)$$

Here,  $e_{jL}$  are the left-handed components of the charged lepton fields ( $j = 1, 2, 3$ ).  $W^-$ ,  $W^+ = (W^-)^\dagger$  and  $Z^0$  are the weak gauge bosons,  $g$  is the weak coupling constant,  $\theta_W$  is the Weinberg angle, and  $\gamma_\mu$  are the usual gamma matrices.  $\nu_{jL}$  and  $\nu_{jR}$  are the Weyl spinors of the three left and right handed neutrino fields in a basis which is chosen such that the neutrino mass matrix  $m_{jk}$  is diagonal (for simplicity we have assumed only a Dirac mass term). Therefore these fields are called neutrino mass eigenstates. They are *different* from the eigenstates participating in the weak interactions, i.e. the weak partner of the electron is a state  $\nu_{eL}$ , called a flavour eigenstate, which is a mixture of  $\nu_{1L}$ ,  $\nu_{2L}$ ,  $\nu_{3L}$ . This mixing is parameterized by the unitary matrix  $U$ , which is called the PMNS (Pontecorvo-Maki-Nakagawa-Sakata) matrix.

### 2.1 Neutrino oscillations in vacuum

Let us consider how flavour mixing affects the propagation of neutrinos in vacuum. We take the initial state to be the flavour eigenstate

$$|\nu_\alpha(0)\rangle = U_{\alpha j}^* |\nu_j\rangle. \quad (2.2)$$

Here and in the following we denote flavour eigenstates ( $e, \mu, \tau$ ) by Greek indices and mass eigenstates (1, 2, 3) by Latin indices. After time  $t$  and distance  $\mathbf{x}$ , the state  $|\nu_\alpha(0)\rangle$  has evolved into

$$|\nu(t)\rangle = U_{\alpha j}^* e^{-i(E_j t - \mathbf{p}_j \cdot \mathbf{x})} |\nu_j\rangle, \quad (2.3)$$

where  $E_j$  and  $\mathbf{p}_j$  are the energy and momentum associated with the mass eigenstate  $j$ . They can be derived from the dynamics of the elementary process in which the neutrino is produced.

For example, in the case of pion decay at rest,  $\pi^+ \rightarrow \mu^+ + \nu_\mu$  or  $\pi^- \rightarrow \mu^- + \bar{\nu}_\mu$ , we have in the centre of mass system

$$m_\pi = E_j + E_\mu = \sqrt{m_j^2 + \mathbf{p}_j^2} + \sqrt{m_\mu^2 + \mathbf{p}_\mu^2}, \quad (2.4)$$

$$\mathbf{p}_\mu = -\mathbf{p}_j \quad (2.5)$$

Substituting Eq. (2.5) into Eq. (2.4) and taking the square we eventually obtain

$$m_\pi^2 = m_j^2 + \mathbf{p}_j^2 + m_\mu^2 + \mathbf{p}_j^2 + 2\sqrt{m_j^2 + \mathbf{p}_j^2}\sqrt{m_\mu^2 + \mathbf{p}_j^2} \quad (2.6)$$

$$4(m_j^2 + \mathbf{p}_j^2)(m_\mu^2 + \mathbf{p}_j^2) = (m_j^2 + m_\mu^2 - m_\pi^2 + 2\mathbf{p}_j^2)^2 \quad (2.7)$$

$$2m_j^2 m_\mu^2 = m_\pi^4 + m_j^4 + m_\mu^4 - 2m_\pi^2 m_j^2 - 2m_\pi^2 m_\mu^2 - 4\mathbf{p}_j^2 m_\pi^2. \quad (2.8)$$

Simplifying this leads to the following expressions for  $\mathbf{p}_j^2$  and  $E_j^2$ :

$$\mathbf{p}_j^2 = \frac{m_\pi^2}{4} \left(1 - \frac{m_\mu^2}{m_\pi^2}\right)^2 - \frac{m_j^2}{2} \left(1 + \frac{m_\mu^2}{m_\pi^2}\right) + \frac{m_j^4}{4m_\pi^2}, \quad (2.9)$$

$$E_j^2 = \frac{m_\pi^2}{4} \left(1 - \frac{m_\mu^2}{m_\pi^2}\right)^2 + \frac{m_j^2}{2} \left(1 - \frac{m_\mu^2}{m_\pi^2}\right) + \frac{m_j^4}{4m_\pi^2}. \quad (2.10)$$

By denoting the energy that would be obtained for massless neutrinos by  $E = \frac{m_\pi}{2}(1 - m_\mu^2/m_\pi^2)$  and keeping only terms up to second order in  $m_j$ , this simplifies to

$$\mathbf{p}_j = E - \frac{m_j^2}{2E} \left(\frac{1}{2} + \frac{m_\mu^2}{2m_\pi^2}\right) =: E - \frac{m_j^2}{2E} \cdot \xi, \quad (2.11)$$

$$E_j = E + \frac{m_j^2}{2E} \left(1 - \left[\frac{1}{2} + \frac{m_\mu^2}{2m_\pi^2}\right]\right) =: E + \frac{m_j^2}{2E} \cdot (1 - \xi). \quad (2.12)$$

If the neutrino is produced in some other process than pion decay,  $\xi$  will be different, but the structure of the equations remains the same. The exponent in the neutrino evolution equation (2.3) can now be rewritten as

$$E_j t - \mathbf{p}_j \mathbf{x} = Et + \frac{m_j^2}{2E}(1 - \xi)t - Ex + \frac{m_j^2}{2E}\xi x. \quad (2.13)$$

Although the group speeds of the neutrino wave packets differ from the speed of light by terms of order  $m_j^2$ , the time resolution in a realistic experiment is too poor to resolve this

difference. Therefore, quantum mechanical uncertainty justifies taking  $x = t$ .<sup>1</sup> Thus the terms proportional to  $\xi$  drop out, and we simply have

$$|\nu(t)\rangle = U_{\alpha j}^* e^{-i m_j^2 t / 2E} |\nu_j\rangle. \quad (2.14)$$

From this, the neutrino oscillation probability is obtained as

$$P(\nu_\alpha \rightarrow \nu_\beta) = |\langle \nu_\beta | \nu(t) \rangle|^2 \quad (2.15)$$

$$= \left| U_{\beta j} U_{\alpha j}^* e^{-i m_j^2 t / 2E} \right|^2. \quad (2.16)$$

In most textbooks, a different derivation of Eq. (2.16) is given, starting from the Schrödinger equation

$$i \frac{d}{dt} \psi = H \psi \quad (2.17)$$

with  $\psi = (\psi_e, \psi_\mu, \psi_\tau)^T$  and

$$H = U \begin{pmatrix} E + \frac{m_1^2}{2E} & 0 & 0 \\ 0 & E + \frac{m_2^2}{2E} & 0 \\ 0 & 0 & E + \frac{m_3^2}{2E} \end{pmatrix} U^\dagger. \quad (2.18)$$

In the standard notation used here,  $\psi_e$ ,  $\psi_\mu$  and  $\psi_\tau$  are the contributions of the neutrino flavour eigenstates to the wave function  $\psi$ , i.e.

$$\psi = \psi_e |\nu_e\rangle + \psi_\mu |\nu_\mu\rangle + \psi_\tau |\nu_\tau\rangle, \quad (2.19)$$

$E$  is the energy for massless neutrinos, and  $U$  is again the PMNS matrix relating the components in the flavour basis  $\psi_\alpha$  to those in the mass basis  $\psi_j$  via

$$\begin{pmatrix} \psi_e \\ \psi_\mu \\ \psi_\tau \end{pmatrix} = \begin{pmatrix} U_{e1} & U_{e2} & U_{e3} \\ U_{\mu1} & U_{\mu2} & U_{\mu3} \\ U_{\tau1} & U_{\tau2} & U_{\tau3} \end{pmatrix} \begin{pmatrix} \psi_1 \\ \psi_2 \\ \psi_3 \end{pmatrix}. \quad (2.20)$$

The neutrino evolution is given by the  $S$ -matrix

$$S = e^{-iH} = U \begin{pmatrix} e^{-i(E+m_1^2/2E)} & 0 & 0 \\ 0 & e^{-i(E+m_2^2/2E)} & 0 \\ 0 & 0 & e^{-i(E+m_3^2/2E)} \end{pmatrix} U^\dagger, \quad (2.21)$$

---

<sup>1</sup>Note that for supernova and solar neutrinos, the assumption  $x = t$  is no longer justified. The distances travelled by these neutrinos are so large that the wave packet components corresponding to different mass eigenstates become spatially separated due to their slightly different velocities. Quantum mechanical coherence is then lost, and the oscillation phenomenology changes. See refs. [2, 3] for a discussion of this effect.

and the oscillation probabilities are the squared moduli of the  $S$ -matrix elements,

$$P(\nu_\alpha \rightarrow \nu_\beta) = |S_{\beta\alpha}|^2 \quad (2.22)$$

$$= \left| U_{\beta j} U_{\alpha j}^* e^{-im_j^2/2E} \right|^2, \quad (2.23)$$

which is just Eq. (2.16). Note that all flavour-independent contributions to  $H$  have dropped out in the calculation of the oscillation probabilities, therefore it is often convenient to neglect them from the beginning.

The Schrödinger ansatz is not strictly correct because the  $\xi$ -term in the energy eigenvalues given by Eq. (2.12) is neglected in this approach. Furthermore, the  $\mathbf{x}$ -dependence of the wave functions is omitted, i.e. effectively all momenta  $\mathbf{p}_j$  are assumed to be equal, so the  $\xi$  term in Eq. (2.11) is neglected as well. However, the more accurate derivation leading to Eq. (2.14) shows that the combination of these two simplifications leads to the correct result since  $\xi$  drops out anyway.

### 2.1.1 The two-flavour case

To discuss the phenomenology of neutrino oscillations, let us start by applying Eq. (2.16) to a system of only two neutrino flavours  $\nu_e$  and  $\nu_\mu$ . The PMNS mixing matrix then simplifies to a 2-dimensional rotation,

$$U = \begin{pmatrix} \cos \theta & \sin \theta \\ -\sin \theta & \cos \theta \end{pmatrix}, \quad (2.24)$$

and the oscillation probability for an electron neutrino at baseline  $L$  is given by

$$P(\nu_e \rightarrow \nu_\mu) = \left| -\sin \theta \cos \theta e^{-im_1^2 L/2E} + \cos \theta \sin \theta e^{-im_2^2 L/2E} \right|^2 \quad (2.25)$$

$$= \sin^2 \theta \cos^2 \theta \left[ 2 - \cos \frac{(m_2^2 - m_1^2)L}{2E} \right] \quad (2.26)$$

$$= \sin^2 2\theta \sin^2 \frac{\Delta m^2 L}{4E}. \quad (2.27)$$

In the last step we have introduced the short hand notation  $\Delta m^2 = m_2^2 - m_1^2$ . Equation (2.27) shows that after a distance  $L_{\text{osc}}/2 = 2\pi E/\Delta m^2$  the probability for finding the neutrino in the state  $|\nu_\mu\rangle$  is maximal, while after a full oscillation length  $L_{\text{osc}}$ , the system is back in the initial state. The amplitude of the oscillations is determined by the mixing angle  $\theta$ , where  $\theta = \pi/4$  corresponds to maximal oscillations. Note that Eq. (2.27) does not depend on  $L$  and  $E$  independently, but only on the ratio  $L/E$ .

### 2.1.2 The three-flavour case

In a system with three neutrino flavours, mixing becomes more complicated. A general unitary  $n \times n$  mixing matrix of Dirac particles can be parameterized by  $n(n-1)/2$  rotation angles and  $n(n+1)/2$  complex phase factors, of which  $2n-1$  can be absorbed into a redefinition of the particle fields. For the  $3 \times 3$  case we thus have three mixing angles  $\theta_{12}$ ,  $\theta_{13}$  and  $\theta_{23}$ , and one complex phase  $\delta_{CP}$ , which is responsible for CP violation in the neutrino sector. The three flavour PMNS matrix is conveniently parameterized as

$$U = \begin{pmatrix} 1 & & \\ & c_{23} & s_{23} \\ & -s_{23} & c_{23} \end{pmatrix} \begin{pmatrix} c_{13} & & s_{13}e^{-i\delta_{CP}} \\ & 1 & \\ -s_{13}e^{i\delta_{CP}} & & c_{13} \end{pmatrix} \begin{pmatrix} c_{12} & s_{12} & \\ -s_{12} & c_{12} & \\ & & 1 \end{pmatrix} \quad (2.28)$$

$$= \begin{pmatrix} c_{12}c_{13} & & s_{12}c_{13} & s_{13}e^{-i\delta_{CP}} \\ -s_{12}c_{23} - c_{12}s_{13}s_{23}e^{i\delta_{CP}} & c_{12}c_{23} - s_{12}s_{13}s_{23}e^{i\delta_{CP}} & c_{13}s_{23} & \\ s_{12}s_{23} - c_{12}s_{13}c_{23}e^{i\delta_{CP}} & -c_{12}s_{23} - s_{12}s_{13}c_{23}e^{i\delta_{CP}} & c_{13}c_{23} & \end{pmatrix}, \quad (2.29)$$

with the abbreviations  $c_{ij} = \cos \theta_{ij}$  and  $s_{ij} = \sin \theta_{ij}$ . The oscillation probabilities can again be calculated from Eq. (2.16). A discussion of the rich phenomenology of three-flavour neutrino oscillations is deferred to chapter 4. There, we will also give some exact and approximate expressions for the most important oscillation probabilities.

## 2.2 Neutrino oscillations in matter

### 2.2.1 Derivation of the matter potential

The presence of matter leads to interesting phenomenological modifications of neutrino mixing and oscillations. It can be read off from Eq. (2.1) that neutrinos interact with matter through their neutral current (NC) coupling to the  $Z^0$  boson, and through their charged current (CC) coupling to the  $W^\pm$  bosons. Ordinary incoherent scattering processes are irrelevant for neutrino oscillations because they only lead to a decrease of the beam intensity, which can be described by a complex contribution to  $H$ . This contribution is proportional to the scattering amplitude, hence it is suppressed by the Fermi constant  $G_F$  and can be neglected. The situation is different for coherent forward scattering, where the contributions from many scattering centres add up *coherently*. Even though the amplitude for coherent forward scattering is also proportional to  $G_F$ , it is enhanced by the large number of scattering centres and can give a significant contribution to the Hamiltonian.

Coherent forward scattering is possible via NC interactions with leptons and quarks, and via CC interactions with leptons, but we can neglect neutral currents here because they lead to flavour-independent terms which are irrelevant for the oscillation probabilities. Only coherent CC interactions with charged leptons can contribute to the oscillation

probabilities. These are not flavour-independent because ordinary matter contains only electrons, but no muons and taus. In extreme environments such as supernovae or the early universe, also  $\mu$  and  $\tau$  leptons are present, but we will not consider this here.

If the neutrino energy is far below the masses of the  $W^\pm$  and  $Z^0$  bosons, the CC part of Eq. (2.1) can be approximated by

$$\mathcal{L}_{CC}^{\text{eff}} = -\frac{G_F}{\sqrt{2}} [\bar{e}_j \gamma^\mu (1 - \gamma^5) U_{jk}^* \nu_k] [\bar{\nu}_l U_{ml} \gamma_\mu (1 - \gamma^5) e_m], \quad (2.30)$$

where  $G_F = g^2 \sqrt{2} / 8M_W^2$  is the Fermi constant. As only electrons are present in ordinary matter, this simplifies to

$$\mathcal{L}_{CC}^{\text{eff}} = -\frac{G_F}{\sqrt{2}} [\bar{e} \gamma^\mu (1 - \gamma^5) \nu_e] [\bar{\nu}_e \gamma_\mu (1 - \gamma^5) e] + h.c. \quad (2.31)$$

$$= -\frac{G_F}{\sqrt{2}} [\bar{e} \gamma^\mu (1 - \gamma^5) e] [\bar{\nu}_e \gamma_\mu (1 - \gamma^5) \nu_e] + h.c. \quad (2.32)$$

In the second step, we have used the Fierz transform. For an effective description, the electron degrees of freedom can be replaced by their respective expectation values in the background matter field:

$$\langle \bar{e} \gamma^0 e \rangle = N_e \quad (2.33)$$

$$\langle \bar{e} \boldsymbol{\gamma} e \rangle = \langle \mathbf{v}_e \rangle \quad (2.34)$$

$$\langle \bar{e} \gamma^0 \gamma^5 e \rangle = \langle \frac{\sigma_e \mathbf{P}_e}{E_e} \rangle \quad (2.35)$$

$$\langle \bar{e} \boldsymbol{\gamma} \gamma^5 e \rangle = \langle \boldsymbol{\sigma}_e \rangle. \quad (2.36)$$

If the matter is unpolarized and at rest, only  $N_e$  is non-zero. Therefore, also in the neutrino part of Eq. (2.30), only the term containing  $\gamma_0$  survives. This term gives essentially the neutrino particle number, so the contribution to the energy of a single  $\nu_e$  is

$$V = -\mathcal{L}_{CC}^{\text{eff}} = \sqrt{2} G_F N_e. \quad (2.37)$$

For antineutrinos, the particle number is negative, and  $V$  acquires an additional minus sign. For practical calculations, it is sometimes convenient to express  $V$  in terms of the matter density  $\rho$  and the number of electrons per nucleon  $Y_e$ :

$$V = \pm 7.56 \cdot 10^{-14} \left( \frac{\rho}{\text{g/cm}^3} \right) Y_e \text{ eV}. \quad (2.38)$$

In the Earth, we have  $Y_e \approx 0.5$ .

Note that there are scenarios where the assumption of unpolarized matter at rest is not true, which can create interesting phenomenological implications. See e.g. ref. [4] and references therein.

### 2.2.2 The two-flavour case

With the inclusion of the matter potential  $V$  from Eq. (2.37) in the  $ee$  component, the neutrino Hamiltonian (2.18) reads

$$H = U \begin{pmatrix} 0 & 0 \\ 0 & \frac{\Delta m^2}{2E} \end{pmatrix} U^\dagger + \begin{pmatrix} V & \\ & 0 \end{pmatrix} \quad (2.39)$$

$$= \frac{\Delta m^2}{2E} \begin{pmatrix} 1 - \cos 2\theta + 2EV/\Delta m^2 & \sin 2\theta \\ \sin 2\theta & 1 + \cos 2\theta \end{pmatrix}. \quad (2.40)$$

Here we have already neglected flavour-independent contributions which would only contribute phase factors to the  $S$ -matrix. In order to calculate the oscillation probability, we diagonalize  $H$  to obtain the effective energy eigenvalues  $E_{1m}$  and  $E_{2m}$  and the effective mixing angle  $\theta_m$ . We can then write  $H$  in the form  $U_m \text{diag}(E_{1m}, E_{2m}) U_m^\dagger$ , which is similar to the vacuum Hamiltonian with  $\theta$  replaced by  $\theta_m$  and  $\Delta m^2/2E$  replaced by  $E_{2m} - E_{1m}$ . As long as  $V$  is constant, we can derive the oscillation probability exactly as in the vacuum case.

The eigenvalues of Eq. (2.40) are

$$E_{1m} = \frac{V}{2} + \frac{\Delta m^2}{4E} \left( 1 - \sqrt{\sin^2 2\theta + \left( \cos 2\theta - \frac{2EV}{\Delta m^2} \right)^2} \right) \quad (2.41)$$

$$E_{2m} = \frac{V}{2} + \frac{\Delta m^2}{4E} \left( 1 + \sqrt{\sin^2 2\theta + \left( \cos 2\theta - \frac{2EV}{\Delta m^2} \right)^2} \right), \quad (2.42)$$

and the mixing angle is given by

$$\sin 2\theta_m = \frac{\sin 2\theta}{\sqrt{\sin^2 2\theta + \left( \cos 2\theta - \frac{2EV}{\Delta m^2} \right)^2}} \quad (2.43)$$

$$\cos 2\theta_m = \frac{\cos 2\theta - \frac{2EV}{\Delta m^2}}{\sqrt{\sin^2 2\theta + \left( \cos 2\theta - \frac{2EV}{\Delta m^2} \right)^2}}. \quad (2.44)$$

This yields the oscillation probability

$$P(\nu_e \rightarrow \nu_\mu) = \sin^2 2\theta_m \sin^2 \left( \frac{\Delta m^2 L}{4E} \sqrt{\sin^2 2\theta + \left( \cos 2\theta - \frac{2EV}{\Delta m^2} \right)^2} \right). \quad (2.45)$$

It can be easily verified that in the limit  $V = 0$ , the vacuum oscillation probability from Eq. (2.27) is recovered.

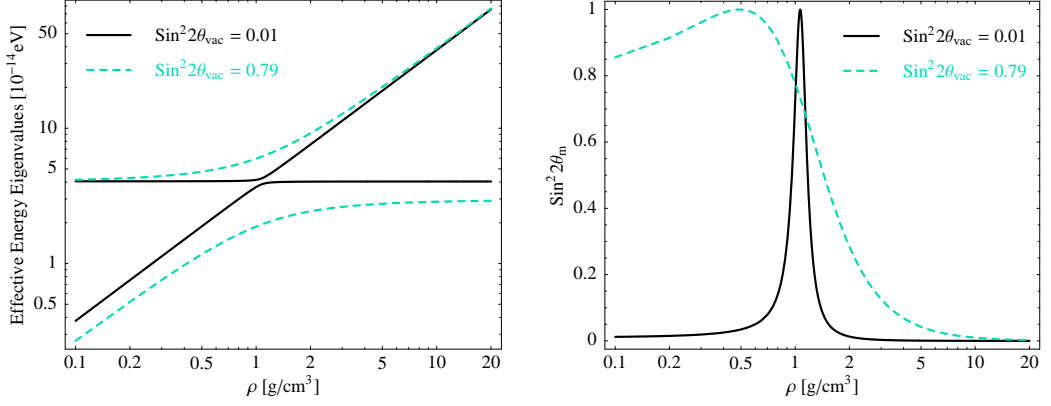


Figure 2.1: Left panel: The energy eigenvalues for neutrino propagation in matter for a two-flavour system. Right panel: The oscillation amplitude in matter. For the parameter values we chose  $\Delta m^2 = 8.1 \cdot 10^{-5} \text{ eV}^2$  and  $E = 1 \text{ GeV}$ .

$E_{1m}$ ,  $E_{2m}$  and  $\theta_m$  are shown in Fig. 2.1 as functions of the matter density  $\rho$ . For low densities, the effect of matter is small because  $\cos 2\theta \gg 2EV/\Delta m^2$ . At  $\cos 2\theta = 2EV/\Delta m^2$ , oscillations are resonantly enhanced because  $\sin^2 2\theta_m = 1$ . If  $\Delta m^2 > 0$ , this resonance occurs for neutrinos, while for  $\Delta m^2 < 0$  it moves to the antineutrino sector, where  $V < 0$ . The resonance is of course most obvious if the vacuum mixing angle is small (solid curves in Fig. 2.1). Note that the position of the resonance depends only on  $E$ , but not on  $L$ , so that the  $L/E$  dependence of the oscillation probabilities, which we have seen in Eq. (2.27), is broken. For very large  $\rho$ , the denominator of eqs. (2.43) and (2.44) is governed by the matter potential, so  $\theta_m \rightarrow \pi/2$  and mixing is suppressed, irrespective of the vacuum angle. If  $\theta$  was less than  $\pi/4$  in vacuum, the composition of the flavour eigenstates is now reversed compared to the vacuum case, i.e. the state that originally consisted mainly of  $|\nu_{1m}\rangle$  is now dominated by the  $|\nu_{2m}\rangle$  contribution, and vice versa.

This can lead to the MSW (Mikheyev-Smirnov-Wolfenstein) effect, where a neutrino flavour conversion in an inhomogeneous matter potential occurs by an adiabatic transition. Consider, for example, a scenario with  $\theta < \pi/4$ , and with neutrinos travelling through matter of slowly decreasing density. A  $\nu_e$  which is produced in the high density regime, well above the resonance, is initially mainly composed of the mass eigenstate  $|\nu_{m2}\rangle$  because  $\theta_m \approx \pi/2$  there. As the neutrino travels to regions of lower density, it remains in this state as long as the density varies slowly (i.e. adiabatically). In vacuum, however,  $|\nu_2\rangle$  is the main constituent of  $|\nu_\mu\rangle$ , not  $|\nu_e\rangle$ . So, a flavour transition has occurred. Adiabaticity is crucial for the MSW effect to take place. If the matter potential changes too quickly, the neutrino can “jump” to the other mass eigenstate. This is more likely to happen if  $\sin^2 2\theta$  is small, because in this case the gap between the two energy

eigenstates at the resonance, given by  $\Delta m^2/2E \cdot \sin 2\theta$ , is also small (see left panel of Fig. 2.1). The MSW effect is of practical importance for solar and supernova neutrinos. See ref. [5] for a more detailed discussion.

### 2.2.3 The three-flavour case

It is straightforward to generalize the discussion of neutrino oscillations in matter to a three-flavour system. The starting point is again the Hamiltonian in the flavour basis:

$$H = U \begin{pmatrix} 0 & 0 & 0 \\ 0 & \frac{\Delta m_{21}^2}{2E} & 0 \\ 0 & 0 & \frac{\Delta m_{31}^2}{2E} \end{pmatrix} U^\dagger + \begin{pmatrix} V & & \\ & 0 & \\ & & 0 \end{pmatrix} \quad (2.46)$$

Diagonalization of  $H$  yields the energy eigenstates and the mixing matrix in matter. As long as  $\rho$  is constant, these can be inserted into Eq. (2.16) to obtain the oscillation probabilities. It is in principle possible to perform this calculation analytically [6], but for practical purposes it is sufficient to make convenient approximations (see chapter 4), or to solve the problem numerically (see appendix A).

The phenomenology of three-flavour neutrino oscillations in matter will be discussed in chapter 4. Here, we will only show some general observations that can be made from a numerical diagonalization of  $H$ . In Fig. 2.2 we show the three energy eigenvalues  $E_{1m}$ ,  $E_{2m}$  and  $E_{3m}$  as functions of the matter density, in analogy with the left panel of Fig. 2.1. The curves show two resonances. The one at  $\rho \approx 0.5 \text{ g cm}^{-3}$  is called the solar resonance because its position is determined by the condition  $2EV/\Delta m_{21}^2 = \cos 2\theta_{12}$ , which depends on the parameters  $\Delta m_{21}^2$  and  $\theta_{12}$  which are also relevant for oscillations of solar neutrinos. The high density resonance at  $\rho \approx 29 \text{ g cm}^{-3}$  is called atmospheric resonance, but this name is a bit misleading because the resonance condition is  $2EV/\Delta m_{31}^2 = \cos 2\theta_{13}$ , while the parameters responsible for atmospheric neutrino oscillations are  $\Delta m_{31}^2$  and  $\theta_{23}$ . The gap between  $E_{1m}$  and  $E_{2m}$  at the solar resonance is  $\Delta m_{21}^2/2E \cdot \sin 2\theta_{12}$ , while the gap between  $E_{2m}$  and  $E_{3m}$  at the atmospheric resonance is given by  $\Delta m_{31}^2/2E \cdot \sin 2\theta_{13}$ .

The composition of the flavour eigenstates in matter is illustrated in figure 2.3. At the left edge of the plots, mixing is given by the PMNS matrix in vacuum, Eq. (2.29): The large  $\theta_{12}$ -rotation mixes the energy eigenstates  $E_1$  and  $E_2$ , and since the (13)-rotation is very small and the (23)-rotation does not affect electron neutrinos,  $\nu_e$  is basically given by this mixture.  $\nu_\mu$  and  $\nu_\tau$  are constructed by combining one of the mixed (12)-states with the  $E_3$  state. For  $\theta_{13} = 0$  and  $\theta_{23} = \pi/4$ , the composition of  $\nu_\mu$  and  $\nu_\tau$  would only differ in the phase factors associated with the components.

For matter densities above the solar resonance, the curves for  $E_{1m}$  and  $E_{2m}$  cross each other, i.e. the (12)-mixing gets reversed compared to the vacuum case, and finally vanishes as  $\rho$  increases further. We have already seen this effect for the two-flavour

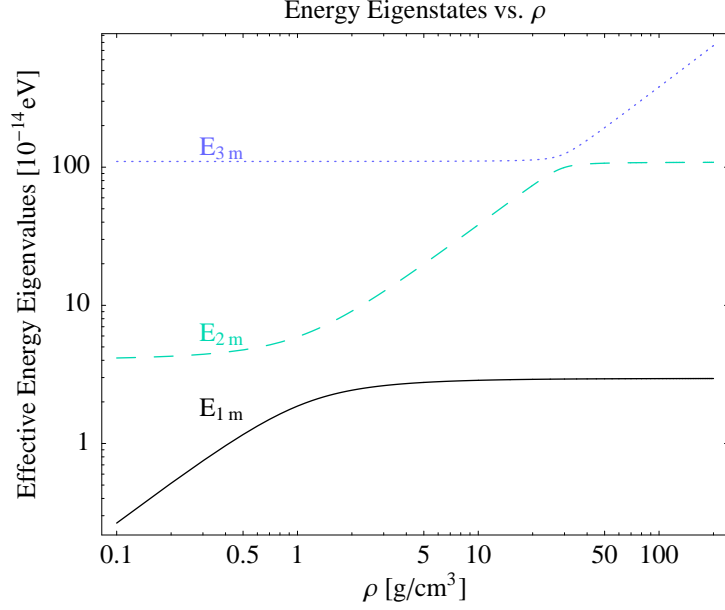


Figure 2.2: Energy eigenstates in matter for the three-flavour case. We used the following parameter values, which are suggested by global fits to neutrino oscillation data [7]:  $\sin^2 2\theta_{12} = 0.79$ ,  $\sin^2 2\theta_{23} = 1.0$ ,  $\sin^2 2\theta_{13} = 0.05$ ,  $\Delta m_{21}^2 = 8.1 \cdot 10^{-5} \text{ eV}^2$ ,  $\Delta m_{31}^2 = 2.2 \cdot 10^{-5} \text{ eV}^2$  and  $\delta_{CP} = 0.0$ . The neutrino energy was 1 GeV.

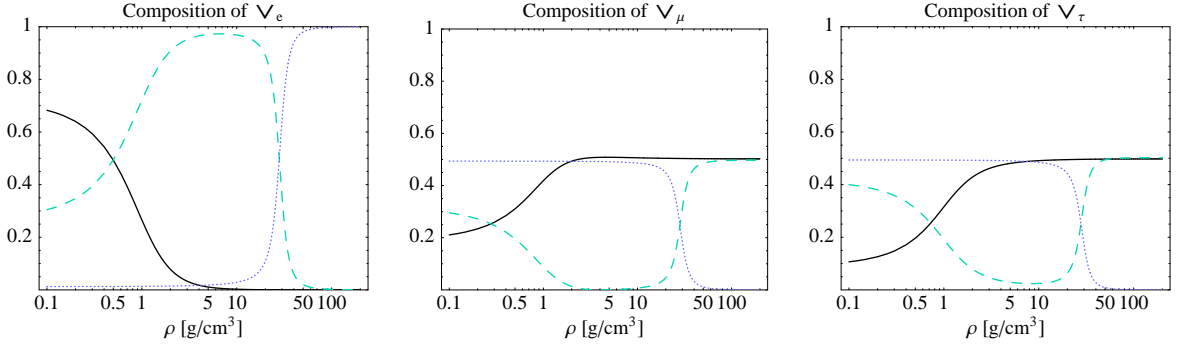


Figure 2.3: Squared moduli of the amplitudes of the energy eigenstates in the composition of the flavour eigenstates in matter for a three-flavour system. The solid black curve corresponds to mass eigenstate  $\nu_1$ , the cyan dashed curve to  $\nu_2$ , and the dotted blue curve to  $\nu_3$ . The sum of the squared moduli is always 1. For the oscillation parameters, we chose the same values as in Fig. 2.2.

system in Sec. 2.2.2. At the atmospheric resonance,  $E_{2m}$  and  $E_{3m}$  cross in a similar way.  $E_{1m}$  remains unaffected although the atmospheric resonance is driven by  $\theta_{13}$ , not  $\theta_{23}$ , because  $E_{1m}$  and  $E_{2m}$  have exchanged their places at the solar resonance.

## 2.3 Mathematical properties of the oscillation probabilities

The neutrino oscillation probabilities have many interesting mathematical features and interdependencies, which can greatly simplify calculations. Therefore we will give a brief overview of such properties here.

### 2.3.1 Oscillation probabilities for antineutrinos

We have already seen in Sec. 2.2 that the matter potentials for neutrinos and antineutrinos have different sign. In addition to this, also the sign of  $\delta_{CP}$  has to be reversed when considering antineutrinos. To understand this, note that antineutrino interactions are contained in the hermitian conjugate part of Eq. (2.1), so their mixing is described by the complex conjugate of the PMNS matrix. Since  $U$  gets its imaginary part solely through  $\delta_{CP}$ , complex conjugation is equivalent to reversing the sign of  $\delta_{CP}$ . In summary, the oscillation probabilities for neutrinos and antineutrinos therefore obey the relation

$$P_{\bar{\alpha}\bar{\beta}} = P_{\alpha\beta}(\delta_{CP} \rightarrow -\delta_{CP}, V \rightarrow -V). \quad (2.47)$$

### 2.3.2 Interdependencies of oscillation channels

Unitarity implies that the oscillation probabilities fulfill

$$\sum_{\alpha} P_{\alpha\beta} = \sum_{\beta} P_{\alpha\beta} = 1 \quad (2.48)$$

Of these six conditions, only five are independent, so we can express five of the nine oscillation probabilities by the remaining four [8]. A further simplification is possible due to the fact that the (23)-rotation in Eq. (2.29) commutes with the matter contribution  $\text{diag}(V, 0, 0)$  [9]. This reduces the number of independent oscillation probabilities to two. If we take these to be  $P_{e\mu}$  and  $P_{\mu\tau}$ , and introduce the notation

$$\tilde{P}_{\alpha\beta} = P_{\alpha\beta}(\theta_{23} \rightarrow \theta_{23} + \pi/2), \quad (2.49)$$

we have

$$P_{ee} = 1 - P_{e\mu} - \tilde{P}_{e\mu}, \quad (2.50)$$

$$P_{e\tau} = \tilde{P}_{e\mu}, \quad (2.51)$$

$$P_{\mu e} = P_{e\mu} - P_{\mu\tau} + \tilde{P}_{\mu\tau}, \quad (2.52)$$

$$P_{\mu\mu} = 1 - P_{e\mu} - \tilde{P}_{\mu\tau}, \quad (2.53)$$

$$P_{\tau e} = \tilde{P}_{e\mu} + P_{\mu\tau} - \tilde{P}_{\mu\tau}, \quad (2.54)$$

$$P_{\tau\mu} = \tilde{P}_{\mu\tau}, \quad (2.55)$$

$$P_{\tau\tau} = 1 - \tilde{P}_{e\mu} - P_{\mu\tau}. \quad (2.56)$$

Besides these relations, it is sometimes convenient to use the identity

$$P_{\beta\alpha} = P_{\alpha\beta}(\delta_{CP} \rightarrow -\delta_{CP}, V(x) \rightarrow V_{\text{rev}}), \quad (2.57)$$

which is discussed in [10]. Here,  $V_{\text{rev}}$  is the reversed matter potential which is obtained by interchanging the positions of the neutrino source and detector. For a constant (or symmetric) potential, Eq. (2.57) simplifies to

$$P_{\beta\alpha} = P_{\alpha\beta}(\delta_{CP} \rightarrow -\delta_{CP}). \quad (2.58)$$

# Chapter 3

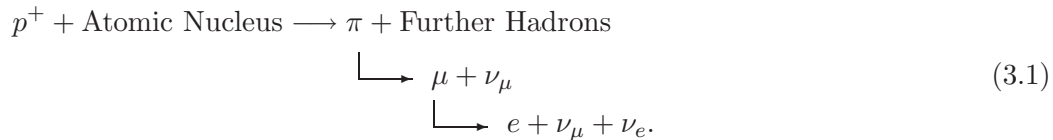
## Current status of neutrino oscillation physics

Since neutrino oscillations have first been established for atmospheric neutrinos by the Super-Kamiokande experiment in 1998 [11], and for solar neutrinos by the SNO experiment in 2002 [12], these observations have been confirmed by many other collaborations.

In this chapter, we will review the current knowledge about the oscillation parameters. We will show how the leading solar and atmospheric parameters have been measured, we will give limits on the yet unknown parameters, and discuss the open questions that will be addressed by future experiments.

### 3.1 The atmospheric oscillation parameters

The angular dependence of the counting rates of atmospheric neutrinos in the Super-Kamiokande detector in Japan provided the first compelling evidence for neutrino oscillations [11]. Atmospheric neutrinos are produced by interactions of cosmic rays with the atmosphere at a height of around 10 to 20 km above ground. The main production reaction is



Therefore the initial atmospheric neutrino flux consists of  $\nu_e$ ,  $\bar{\nu}_e$ ,  $\nu_\mu$  and  $\bar{\nu}_\mu$  with a ratio of  $(\nu_\mu + \bar{\nu}_\mu)/(\nu_e + \bar{\nu}_e) \approx 2$ . Atmospheric neutrinos cover a wide range of energies, and although their flux decreases rapidly for large  $E$ , neutrinos with several TeV can be observed. The distances travelled by atmospheric neutrinos before their detection range up to the Earth diameter of 12,742 km for upward going neutrinos. Super-Kamiokande detects neutrino interactions by the Čerenkov radiation emitted by secondary charged particles. The detector can distinguish  $\nu_e$  and  $\nu_\mu$ , but it cannot separate neutrino from antineutrino events. Furthermore it has virtually no capability of identifying  $\nu_\tau$  interactions [13].

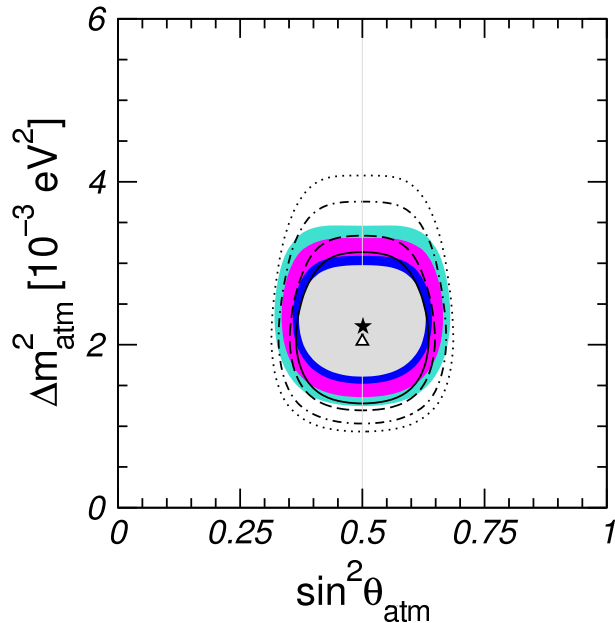


Figure 3.1: The current best fit values and allowed regions for the atmospheric parameters  $\sin^2 \theta_{23}$  and  $\Delta m_{31}^2$  at the 90%, 95%, 99% and  $3\sigma$  confidence levels, obtained from a two-flavour fit. The thin lines and the triangle correspond to atmospheric data only, while the coloured regions and the star also include K2K data. Plot taken from ref. [7].

The flux of upward going muon neutrinos in Super-Kamiokande is significantly below the expectations without neutrino oscillations, while the rates of downward going  $\nu_\mu$  events and of  $\nu_e$  events agree with expectations. This observation is consistent with two-flavour  $\nu_\mu \rightarrow \nu_\tau$  oscillations. Since in the vacuum approximation the oscillation probability depends only on  $L/E$ , it is possible to directly see the first oscillation maximum if the event rates are plotted over  $L/E$  [14]. The allowed ranges of the atmospheric oscillation parameters derived from Super-Kamiokande data are shown by the thin lines in Fig. 3.1.

Oscillations of  $\nu_\mu$  into  $\nu_\tau$  have been confirmed by the K2K accelerator experiment [15, 16], which sends a  $\nu_\mu$  beam with a mean energy of 1.3 GeV from the KEK accelerator centre to the Super-Kamiokande detector located at a baseline of 250 km. The results of K2K also show a significant lack of  $\nu_\mu$  and no corresponding  $\nu_e$  appearance.

The coloured regions in Fig. 3.1 show the constraints on  $\theta_{23}$  and  $\Delta m_{31}^2$  obtained from a combined analysis of atmospheric and K2K data. The best fit value for the mixing angle

is  $\pi/4$ , i.e. maximal mixing, while the best fit value for  $\Delta m_{31}^2$  is  $2.2 \cdot 10^{-3} \text{ eV}^2$ .<sup>1</sup> The uncertainties are about 10% for  $\theta_{23}$  and 50% for  $\Delta m_{31}^2$ . Note that the sign of  $\Delta m_{31}^2$  is yet unknown because the leading two-flavour vacuum oscillation probability is the same for both choices (cf. Eq. (2.27)). The issue of determining  $\text{sign}(\Delta m_{31}^2)$  experimentally will be discussed below.

## 3.2 The solar oscillation parameters

The sun is an intense source of electron neutrinos. The nuclear fusion reactions in which they are produced are quite complicated, but the net reaction is simply



Most solar neutrinos have energies below 0.5 MeV, but the spectrum extends up to about 19 MeV. Solar neutrino experiments were the first to report a deficit in the observed  $\nu_e$  flux compared to expectations [18–22], but at that time it was not possible to uniquely attribute this deficit to neutrino oscillations, because the theoretically predicted flux depends strongly on the details of the solar model which is used. A slight bias in the solar core temperature could for example explain the reduced neutrino flux. Besides this, a mere deficit can also be explained by other new processes such as neutrino decay. In 2002 the SNO collaboration proved experimentally that the missing  $\nu_e$  have indeed oscillated into other neutrino flavours [12]. They were the first to measure the flavour-independent neutral current interactions with sufficient accuracy to show that the total solar neutrino flux is in excellent agreement with the predictions from solar models, proving that the missing  $\nu_e$  must have been converted to  $\nu_\mu$  and  $\nu_\tau$ .

With this knowledge it is possible to extract bounds on the solar neutrino oscillation parameters  $\sin^2 2\theta_{12}$  and  $\Delta m_{21}^2$  from the data. The thin lines in Fig. 3.2 show the constraints that can be derived from a two-flavour analysis of the experiments Homestake [18, 23], SAGE [19, 24], GALLEX/GNO [20–22], Super-Kamiokande [25], and SNO [12, 26, 27]. In principle there are several distinct windows in the parameter space which all give good fits to the solar data. Figure 3.2 only shows the so-called LMA-MSW (large mixing angle Mikheyev-Smirnov-Wolfenstein) region since all the others have been ruled out by the KamLAND experiment [28, 29], which observed oscillations in the  $\bar{\nu}_e$  flux from several nuclear reactors. The coloured regions in the plot show the parameter constraints from a combined analysis of solar and KamLAND data. The best fit values are  $\sin^2 \theta_{12} = 0.29$  and  $\Delta m_{21}^2 = 8.1 \cdot 10^{-5} \text{ eV}^2$ . The uncertainties are about 10% for both the mixing angle and the mass squared difference.

---

<sup>1</sup>Recently, new results on  $\theta_{23}$  and  $\Delta m_{31}^2$  have been published by MINOS [17], an accelerator experiment in the United States. These results indicate that  $\Delta m_{31}^2 = (3.05 \pm 0.7) \cdot 10^{-3} \text{ eV}^2$ , i.e. the global best fit value will shift to larger values. The MINOS bound on  $\theta_{23}$  is still consistent with maximal mixing.

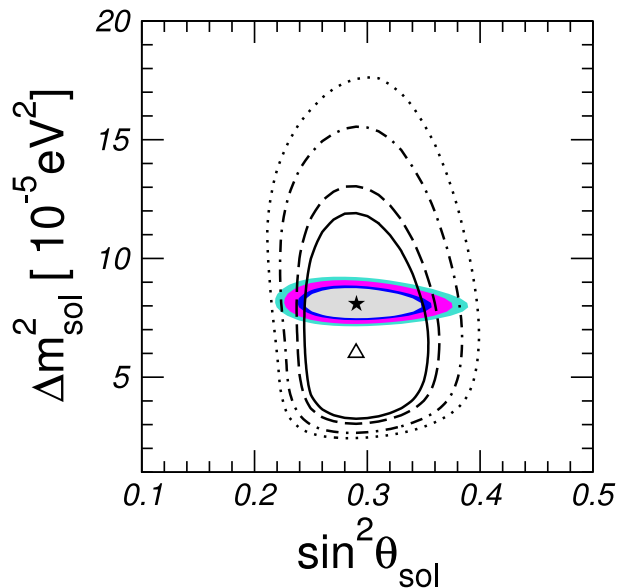


Figure 3.2: The current best fit values and allowed regions for the parameters  $\sin^2 \theta_{12}$  and  $\Delta m_{21}^2$  at the 90%, 95%, 99% and  $3\sigma$  confidence levels, obtained from a two-flavour fit. The thin lines and the triangle correspond to solar data only, while the coloured regions and the star also include KamLAND data. Plot taken from ref. [7].

In contrast to the atmospheric case, the sign of  $\Delta m_{21}^2$  is known to be positive because resonant matter effects inside the sun are necessary to explain the solar neutrino data. If  $\text{sign}(\Delta m_{21}^2)$  were negative, the resonance condition  $2EV/\Delta m_{21}^2 = \cos 2\theta_{12}$  could only be fulfilled in the antineutrino sector, where  $V < 0$ , so it would be irrelevant to solar neutrinos.

### 3.3 Three-flavour fits and future challenges

The most stringent bounds on the neutrino oscillation parameters can be obtained from three-flavour fits to all of the existing data. The results of such a fit are shown in tab. 3.1. As expected, the values for the leading solar and atmospheric parameters are similar to those discussed in the previous sections. For  $\theta_{13}$  an upper bound of  $\sin^2 2\theta_{13} \lesssim 0.2$  exists from the CHOOZ reactor experiment, but  $\delta_{CP}$  is completely unknown so far.

A precise measurement of all oscillation parameters is particularly important to discriminate between the plethora of theoretical models trying to explain the phenomenology of the neutrino sector by introducing new physics beyond the standard model. The

parameter	best fit	$2\sigma$	$3\sigma$	$4\sigma$
$\Delta m_{21}^2 [10^{-5} \text{ eV}^2]$	7.9	7.3–8.5	7.1–8.9	6.8–9.3
$\Delta m_{31}^2 [10^{-3} \text{ eV}^2]$	2.2	1.7–2.9	1.4–3.3	1.1–3.7
$\sin^2 \theta_{12}$	0.30	0.25–0.34	0.23–0.38	0.21–0.41
$\sin^2 \theta_{23}$	0.50	0.38–0.64	0.34–0.68	0.30–0.72
$\sin^2 \theta_{13}$	0.000	$\leq 0.031$	$\leq 0.051$	$\leq 0.073$

Table 3.1: Current experimental values for the three-flavour neutrino oscillation parameters, together with their uncertainties. Table taken from ref. [7].

most prominent concepts are grand unification, supersymmetry, flavour symmetries, and extra dimensions. Each model makes specific predictions for the values of at least some of the oscillation parameters, which need to be tested precisely in order to find out which extension of the standard model is the correct one. See ref. [30] for a recent review of models for neutrino masses and mixings.

The bound on the solar mixing angle  $\theta_{12}$  will be improved when SNO has gathered more statistics, and KamLAND has the potential to further constrain  $\Delta m_{21}^2$ . It is also imaginable to build a new dedicated reactor experiment to measure the solar oscillation parameters [31]. An improvement of the atmospheric parameters  $\theta_{23}$  and  $\Delta m_{31}^2$  will be provided by MINOS [32] and by the upcoming superbeam experiments T2K [33] in Japan and NO $\nu$ A [34]. All these experiments use an accelerator-produced  $\nu_\mu$  beam.

Besides constraining the atmospheric parameters, beam experiments also have the chance to finally measure  $\theta_{13}$ . Figure 3.3 shows the anticipated evolution of the discovery potential and sensitivity to this parameter for the coming decade. The discovery potential of an experiment is defined as the minimum value of  $\theta_{13}$  for which this experiment is able to rule out the hypothesis  $\theta_{13} = 0$  at a given confidence level. The sensitivity is the limit it can set on  $\theta_{13}$ , assuming the true value is zero. The plots show that MINOS might obtain early results, but only for a very small fraction of the parameter space. Chances are however high that  $\theta_{13}$  can be measured by T2K and NO $\nu$ A. Unfortunately the discovery potential of these experiments depends strongly on the value of  $\delta_{CP}$ , as indicated by the coloured bands in Fig. 3.3. This problem is not present in reactor experiments, which use the  $\bar{\nu}_e$  disappearance channel which is independent of  $\delta_{CP}$ . The most advanced reactor experiments are currently Double Chooz [35] and its possible upgrade Triple Chooz [36].

If  $\theta_{13}$  turns out to be large, the combination of superbeam and reactor data will also provide information on  $\delta_{CP}$  [38]. If in contrast  $\theta_{13}$  is small, this will not be possible because in the three-flavour mixing matrix Eq. (2.29), all terms containing  $\delta_{CP}$  are suppressed by  $\sin \theta_{13}$ . For small  $\theta_{13}$ , a more sophisticated experiment such as a neutrino factory or an advanced beta beam is required [39].

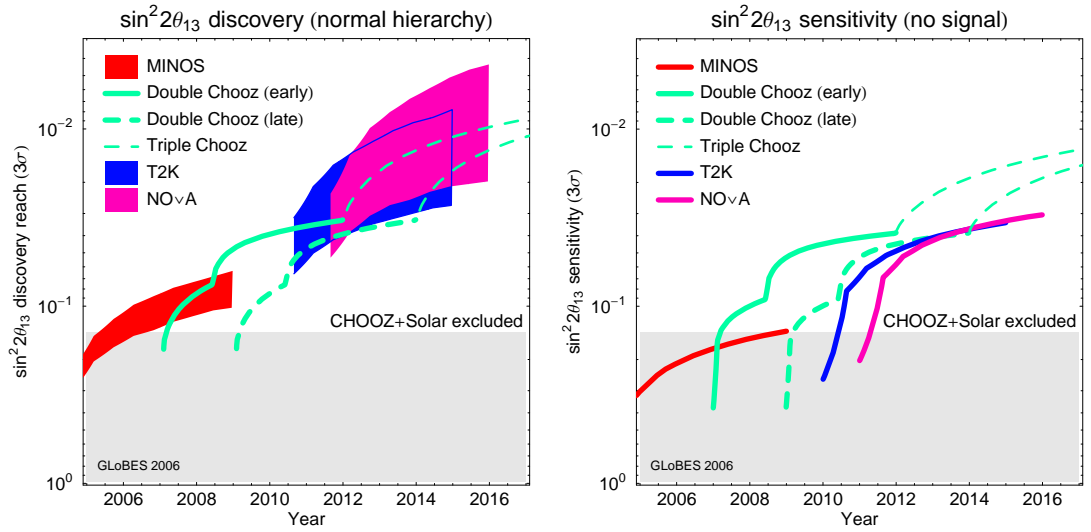


Figure 3.3: A possible evolution of the  $\sin^2 2\theta_{13}$  discovery potential (left) and  $\sin^2 2\theta_{13}$  sensitivity (right) at  $3\sigma$  obtained from simulations with GLoBES [37]. The bands reflect for the neutrino beam experiments the dependence on the unknown value of  $\delta_{CP}$ , i.e. the actual discovery potential will lie in between the best case (upper) and worst (lower) curve depending on the value of  $\delta_{CP}$  chosen by nature. A normal mass hierarchy is assumed in the plots. If the true hierarchy is inverse, the curves for the accelerator experiments become slightly worse. The figure is taken from ref. [36]. Further details on the simulations can be found in this paper and the references therein.

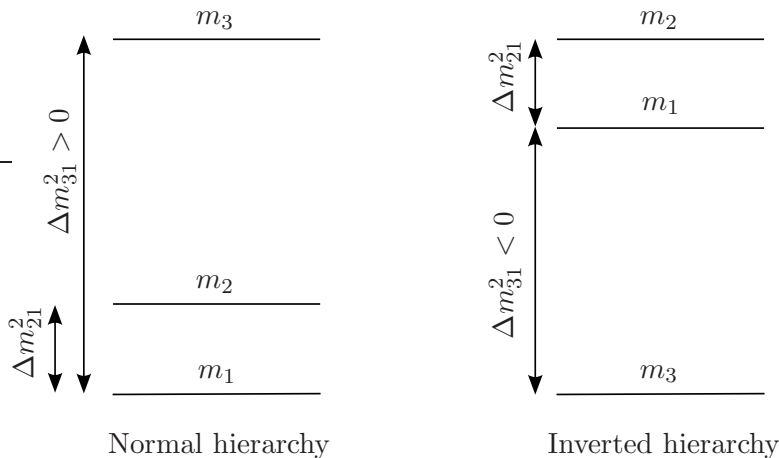


Figure 3.4: Illustration of the normal and inverted neutrino mass hierarchies.

Finally there is the question whether  $\text{sign}(\Delta m_{31}^2)$  is positive or negative. The two possible scenarios termed “normal mass hierarchy” (NH) and “inverted mass hierarchy” (IH) are depicted in Fig. 3.4. For the normal hierarchy, we have

$$\Delta m_{31}^2 > 0, \quad m_1 < m_2 \ll m_3, \quad (3.3)$$

while for the inverted hierarchy

$$\Delta m_{31}^2 < 0, \quad m_3 \ll m_1 < m_2. \quad (3.4)$$

As we have discussed in the context of solar neutrinos, one can distinguish these two possibilities most easily if strong matter effects are observed, which requires very long baselines. Therefore, it is hard to determine the mass hierarchy in an accelerator experiment, but unless  $\theta_{13}$  is extremely small (below  $10^{-5}$ ), it can be extracted from the neutrino signal of a nearby supernova [40, 41].

### 3.4 Non-standard neutrino oscillations

In addition to the clearly established oscillations with mass-squared differences  $\Delta m_{21}^2$  and  $\Delta m_{31}^2$ , there has been a hint for oscillations with a much larger  $\Delta m^2$  from the LSND experiment [42]. The allowed parameter ranges from a fit to the LSND data are shown in Fig. 3.5 together with constraints from atmospheric neutrino experiments, K2K, and various experiments reporting no evidence for neutrino oscillations. Although most of the region allowed by LSND is ruled out by other experiments, there is still the possibility that indeed a fourth neutrino flavour exists that mixes with the three known

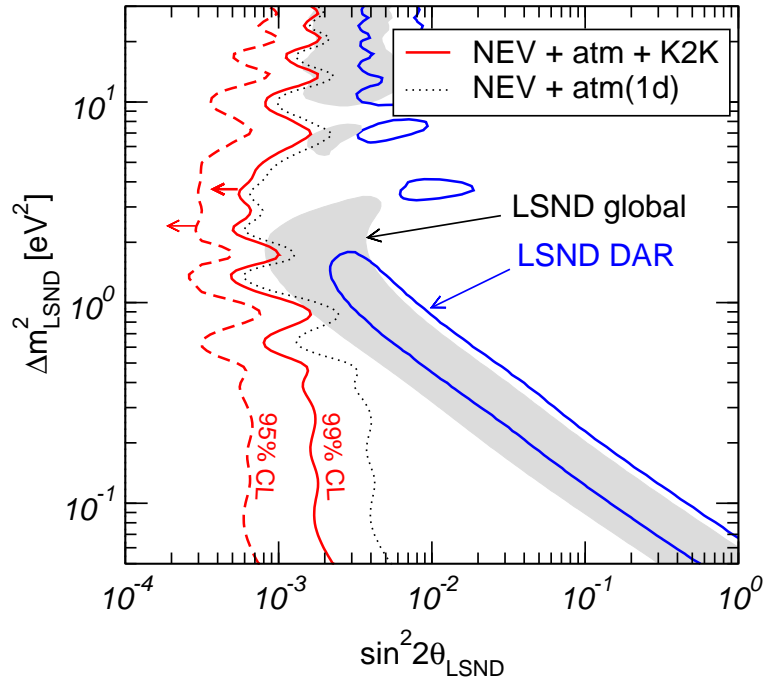


Figure 3.5: Parameter regions suggested by LSND, together with constraints from atmospheric neutrino experiments, K2K, and various experiments that have not found evidence for neutrino oscillations (“NEV”). The plot shows that most of the LSND-allowed region is already ruled out. Figure taken from ref. [7].

species. Such a neutrino would be called “sterile” because it could not participate in standard model weak interactions in order not to violate the bound on the number of neutrino species, which has been obtained from the measurement of the  $Z^0$  decay width at LEP [43]. It is expected that LSND will soon be either confirmed or disproved by the MiniBOONE experiment [44] at Fermilab.

Besides the existence of sterile neutrinos, there might be other non-standard interactions that can lead to neutrino flavour transitions. Even if these are only subdominant compared to the standard oscillations, they might nevertheless be relevant for precision experiments. A discussion of such effects can be found in refs. [45, 46].

## Chapter 4

# The three-flavour neutrino oscillation probabilities

We have seen in chapter 3 that up to now all experimental data on neutrino oscillations can be explained by two-flavour models. This will no longer be true for future precision experiments, which will also be sensitive to generic three-flavour effects such as the presence of the two oscillation lengths,  $4\pi E/\Delta m_{21}^2$  and  $4\pi E/\Delta m_{31}^2$ , in the same channel, leptonic CP violation, and matter effects in  $\nu_\mu \rightarrow \nu_\tau$  oscillations. In the following sections, we will give an overview of the phenomenology of two- and three-flavour effects in the  $\nu_e \rightarrow \nu_e$ ,  $\nu_\mu \rightarrow \nu_e$ , and  $\nu_\mu \rightarrow \nu_\tau$  channels. The other channels can of course be treated in a similar way, but no new effects will occur because of the interdependencies given in eqs. (2.50) to (2.56).

To simplify the discussion, we introduce the following notational conventions

$$\begin{aligned}\alpha &= \frac{\Delta m_{21}^2}{\Delta m_{31}^2} \\ \Delta &= \frac{\Delta m_{31}^2 L}{4E} \\ A &= \frac{2EV}{\Delta m_{31}^2} \\ C_{12} &= \sqrt{\sin^2 2\theta_{12} + (\cos 2\theta_{12} - A/\alpha)^2} \\ C_{13} &= \sqrt{\sin^2 2\theta_{13} + (\cos 2\theta_{13} - A)^2}.\end{aligned}\tag{4.1}$$

$\Delta$  is the phase factor for atmospheric oscillations,  $A$  is a dimensionless quantity associated with the matter potential, and  $C_{12}$  and  $C_{13}$  are the shifts of the solar and atmospheric mass squared differences in matter. We have encountered similar quantities in the discussion of pure two-flavour oscillations in matter in section 2.2.2 (cf. eqs. (2.43), (2.44) and (2.45)). Throughout this section, we will use the following numerical values for the oscillation parameters:

## 4.1 The $\nu_e \rightarrow \nu_e$ channel

The  $\nu_e \rightarrow \nu_e$  channel, which is important for reactor neutrino experiments aiming at the measurement of the solar parameters and of  $\theta_{13}$ , is particularly easy to treat analytically because the expressions in the first row of the PMNS matrix are quite simple. For the vacuum case, we find from eqs. (2.16) and (2.29):

$$P(\nu_e \rightarrow \nu_e) = \left| c_{12}^2 c_{13}^2 + s_{12}^2 c_{13}^2 e^{-2i\alpha\Delta} + s_{13}^2 e^{-2i\Delta} \right|^2 \quad (4.2)$$

$$= c_{12}^4 c_{13}^4 + s_{12}^4 c_{13}^4 + s_{13}^4 + 2c_{12}^2 s_{12}^2 c_{13}^4 \cos 2\alpha\Delta \\ + 2c_{12}^2 c_{13}^2 s_{13}^2 \cos 2\Delta + 2s_{12}^2 s_{13}^2 c_{13}^2 \cos 2(\alpha - 1)\Delta \quad (4.3)$$

$$= c_{13}^4 \left(1 - \frac{1}{2} \sin^2 2\theta_{12}\right) + s_{13}^4 + \frac{1}{2} \sin^2 2\theta_{12} c_{13}^4 \cos 2\alpha\Delta \\ + \frac{1}{2} \sin^2 2\theta_{13} [c_{12}^2 \cos 2\Delta + (1 - c_{12}^2) \cos 2(\alpha - 1)\Delta] \quad (4.4)$$

$$= 1 - c_{13}^4 \sin^2 2\theta_{12} \sin^2 \alpha\Delta - \sin^2 2\theta_{13} \sin^2(\alpha - 1)\Delta \\ + \frac{1}{2} c_{12}^2 \sin^2 2\theta_{13} [\cos 2\Delta - \cos 2(\alpha - 1)\Delta]. \quad (4.5)$$

This expression is plotted in Fig. 4.1 as a function of the baseline  $L$ , and for different energies covered by the reactor neutrino spectrum. The main features of the plot can be easily understood from the terms in Eq. (4.5): The second term, which is proportional to  $\sin^2 \alpha\Delta$ , is responsible for the dominant oscillations with oscillation length  $4\pi E/\Delta m_{21}^2$  and amplitude  $c_{13}^4 \sin^2 2\theta_{12} \approx \sin^2 2\theta_{12}$ . The position of the first oscillation maximum varies from 30 km to 100 km for the energies considered here, so the optimum baseline for a reactor measurement of  $\theta_{12}$  is at several tens of kilometers. The exact value depends also on the shape of the reactor neutrino spectrum, the energy dependence of the cross sections, the flux decreasing with  $1/L^2$ , and the spectra of background sources [31]. The superimposed weak oscillations in Fig. 4.1 originate from the terms proportional to  $\sin^2 2\theta_{13}$ .

For short baselines of less than 2 km, which are typical for reactor measurements of  $\theta_{13}$ , the  $\alpha$ -contributions in Eq. (4.5) can be neglected, and the expression simplifies to  $1 - \sin^2 2\theta_{13} \sin^2 \Delta$ , which corresponds to two-flavour oscillations with the atmospheric oscillation length  $4\pi E/\Delta m_{31}^2$  and the amplitude  $\sin^2 2\theta_{13}$ .

Note that according to Eq. (4.5),  $P(\nu_e \rightarrow \nu_e)$  does not depend on the CP phase  $\delta_{CP}$ . This is still true if matter effects are taken into account.

For larger baseline and higher energies,  $P(\nu_e \rightarrow \nu_e)$  changes significantly if matter is present. However, since most realistic future experiments (except beta beams) do not use the electron disappearance channel at high energies and long baselines, we will not consider these effects here, but rather proceed by studying the  $\nu_\mu \rightarrow \nu_e$  channel, where similar effects appear, and which is much more important for future experiments.

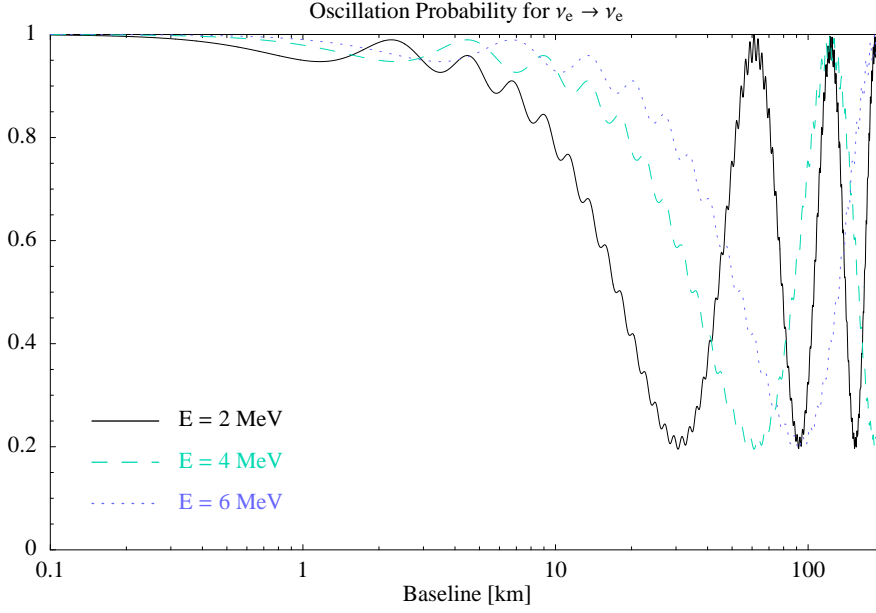


Figure 4.1: The three-flavour oscillation probability for the  $\nu_e \rightarrow \nu_e$  channel as a function of the baseline. The dominant oscillations are driven by the solar parameters, while the superimposed weak oscillations depend on  $\theta_{13}$  and  $\Delta m_{31}^2$ . We have used the following numerical values:  $\sin^2 2\theta_{12} = 0.79$ ,  $\sin^2 2\theta_{23} = 1.0$ ,  $\sin^2 2\theta_{13} = 0.05$ ,  $\Delta m_{21}^2 = 8.1 \cdot 10^{-5} \text{ eV}^2$ ,  $\Delta m_{31}^2 = 2.2 \cdot 10^{-3} \text{ eV}^2$ , and  $\delta_{CP} = 0$ .

## 4.2 The $\nu_\mu \rightarrow \nu_e$ channel

### 4.2.1 Three-flavour effects in vacuum

Generic three-flavour effects are most easily accessible experimentally in the  $\nu_\mu \rightarrow \nu_e$  channel because it is relatively easy to prepare a high energy  $\nu_\mu$  beam and observe the resulting  $\nu_e$  and  $\nu_\mu$ .

In vacuum, it is straightforward to calculate the oscillation probability  $P(\nu_\mu \rightarrow \nu_e)$  in analogy to the derivation of Eq. (4.5). We obtain

$$\begin{aligned}
P_{\text{vac}}(\nu_\mu \rightarrow \nu_e) &= \sin^2 2\theta_{12} c_{23}^2 c_{13}^2 \sin^2 \alpha \Delta \\
&\quad - \frac{1}{2} \sin 2\theta_{12} \sin 2\theta_{13} \sin 2\theta_{23} c_{13} \sin \alpha \Delta \left[ \sin[(\alpha - 2)\Delta - \delta_{CP}] \right. \\
&\quad \quad \quad \left. + \sin \delta_{CP} \cos \alpha \Delta - \cos 2\theta_{12} \cos \delta_{CP} \sin \alpha \Delta \right] \\
&\quad + \frac{1}{4} \sin^2 2\theta_{13} s_{23}^2 \left[ 2 - \sin^2 2\theta_{12} \sin^2 \alpha \Delta - 2c_{12}^2 \cos 2\Delta - 2s_{12}^2 \cos 2(\alpha - 1)\Delta \right] \quad (4.6)
\end{aligned}$$

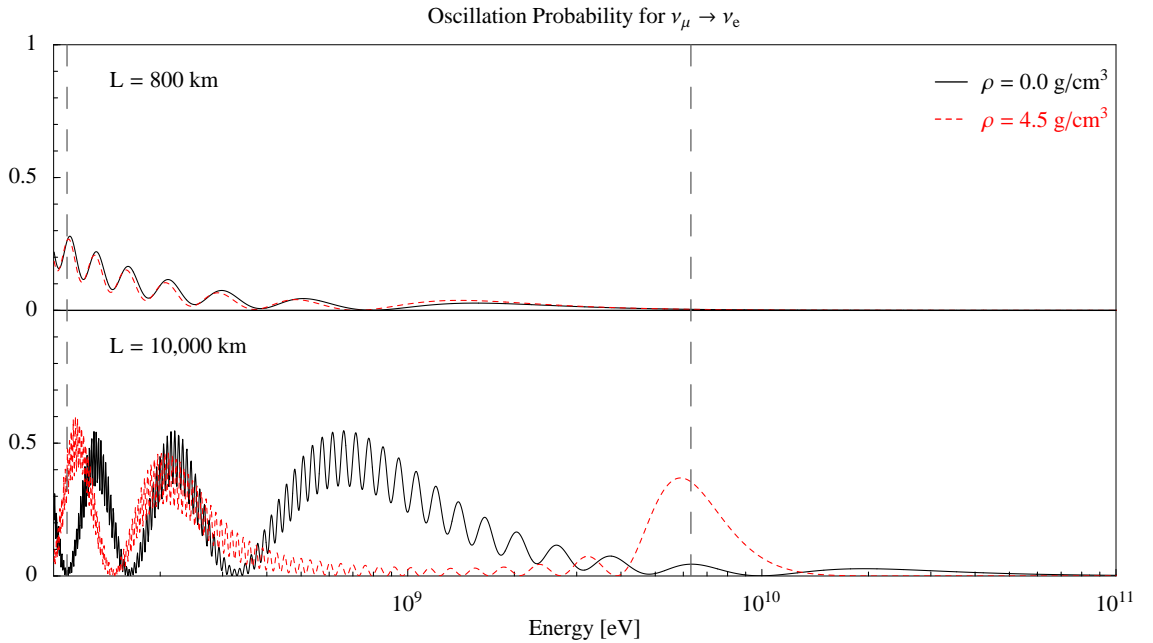


Figure 4.2: The three-flavour oscillation probability for the  $\nu_\mu \rightarrow \nu_e$  channel as a function of the energy. The vertical grey lines indicate the positions of the solar and atmospheric resonances. For the oscillation parameters, we have chosen the same values as in Fig. 4.1.

This probability is shown in the black curves of Fig. 4.2 as a function of the energy and for two different baselines: 800 km (top panel) is roughly the baseline envisaged for the NO $\nu$ A experiment [34], while 10,000 km (bottom panel) is currently only relevant to atmospheric neutrinos, but may be accessible for accelerator projects in the distant future. The features of the curves can be understood from Eq. (4.6). The first term corresponds to solar oscillations, which are the dominating contribution for long baselines and low energies. The solar oscillations are distorted by a contribution proportional to  $\sin 2\theta_{13}$ , with an oscillation frequency which is close to the atmospheric one. The terms containing  $\sin \delta_{CP}$  and  $\cos \delta_{CP}$  cause a slight change in the phase and amplitude of the solar oscillations. Finally, there are contributions proportional to  $\sin^2 2\theta_{13}$ , which are only relevant at the lowest order atmospheric maxima, where all other terms are suppressed by the smallness of  $\sin \alpha\Delta$ .

#### 4.2.2 Three-flavour effects in matter of constant density

If neutrinos oscillate in matter rather than in vacuum, new effects appear as can be seen from the red dashed curves in Fig. 4.2 and from Fig. 4.3, which shows the oscillation

probabilities in matter of constant density for a wide range of energies and baselines. For  $E$  well below 1 GeV, but very long baselines, solar oscillations are still dominant, with a distortion proportional to  $\sin 2\theta_{13}$ . However, for  $E \gtrsim 1$  GeV, i.e. well above the solar resonance, they get completely suppressed due to matter effects. This behaviour can be understood analytically if we neglect the  $\theta_{13}$  contributions for the moment. Then the oscillation probability in matter reads [9]

$$P_{\text{mat}}(\nu_\mu \rightarrow \nu_e) = c_{23}^2 \frac{\sin^2 2\theta_{12}}{C_{12}^2} \sin^2 \alpha C_{12} \Delta. \quad (4.7)$$

If we furthermore introduce the effective mixing angle  $\sin 2\theta_{12}^m = C_{12}^{-1} \sin 2\theta_{12}$  as in Eq. (2.43), we obtain

$$P_{\text{mat}}(\nu_\mu \rightarrow \nu_e) = c_{23}^2 \sin^2 2\theta_{12}^m \sin^2 \alpha C_{12} \Delta. \quad (4.8)$$

This equation describes two-flavour oscillations in matter. As was discussed in section 2.2.2,  $\sin^2 2\theta_{12}^m$  goes to zero above the resonance, so oscillations will vanish there.

However, for energies of several GeV, the *atmospheric* contributions become strong due to the resonant enhancement in matter. For the case of the normal mass hierarchy which is discussed here, the resonance lies in the neutrino sector, but one has to keep in mind that for the inverted hierarchy, it occurs for antineutrinos. The enhancement is only small at the short baseline of 800 km, but it reaches more than 30% at  $L = 10,000$  km. Analytically, the oscillation probability in the resonance region can be approximated by setting  $\alpha = 0$ , neglecting the suppressed solar oscillations, so that

$$P_{\mu e}^{\text{mat}} = s_{23}^2 \sin^2 2\theta_{13}^m \sin^2 \alpha C_{13} \Delta, \quad (4.9)$$

which is again a two-flavour oscillation probability. Although  $\sin^2 2\theta_{13}$  is small in vacuum, it gets maximal at the resonance. All effects that are usually suppressed by  $\theta_{13}$  will therefore be sizeable in the resonance region. This is a great handle for measuring three-flavour effects experimentally.

### 4.2.3 CP violation in the $\nu_\mu \rightarrow \nu_e$ channel

Besides the measurement of  $\theta_{13}$ , the possible discovery of leptonic CP violation is another great challenge for future experiments. Let us consider the effects that a non-zero value of  $\delta_{CP}$  has on the oscillation probability. In Fig. 4.4, we have plotted  $P_{\mu e}$  in matter for a baseline of 800 km and for three different values of  $\delta_{CP}$ .

To understand the features of this plot, let us consider the expansion of  $P_{\mu e}$  up to second order in  $\alpha$  and  $s_{13}$  derived in ref. [9], which gives a good approximation to the

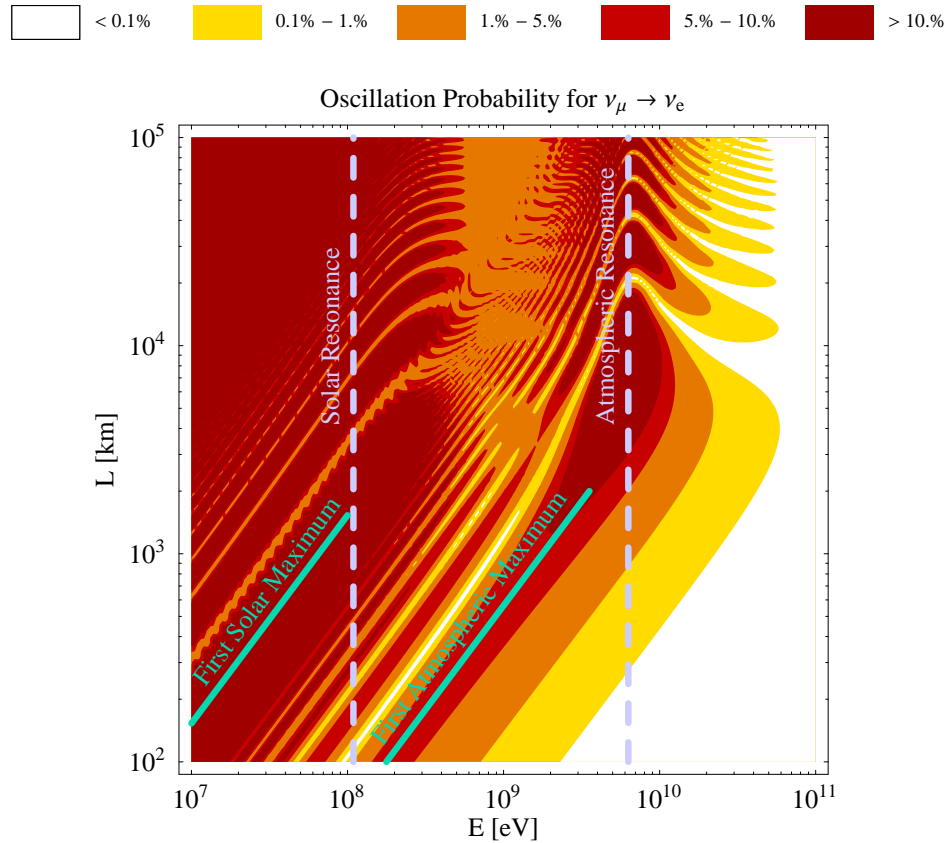


Figure 4.3: Contour Plot of the  $\nu_\mu \rightarrow \nu_e$  oscillation probability in matter of constant density  $\rho = 4.5 \text{ g cm}^{-3}$ . The diagonal structures correspond to lines of constant  $L/E$ , while deviations from this  $L/E$  scaling are caused by matter effects. The probabilities have been folded with a 1% Gaussian energy resolution function to suppress aliasing effects in the sub-GeV region. The colour-coding is non-linear in order to reveal small three-flavour effects. The values of the oscillation parameters are the same as in Fig. 4.1.

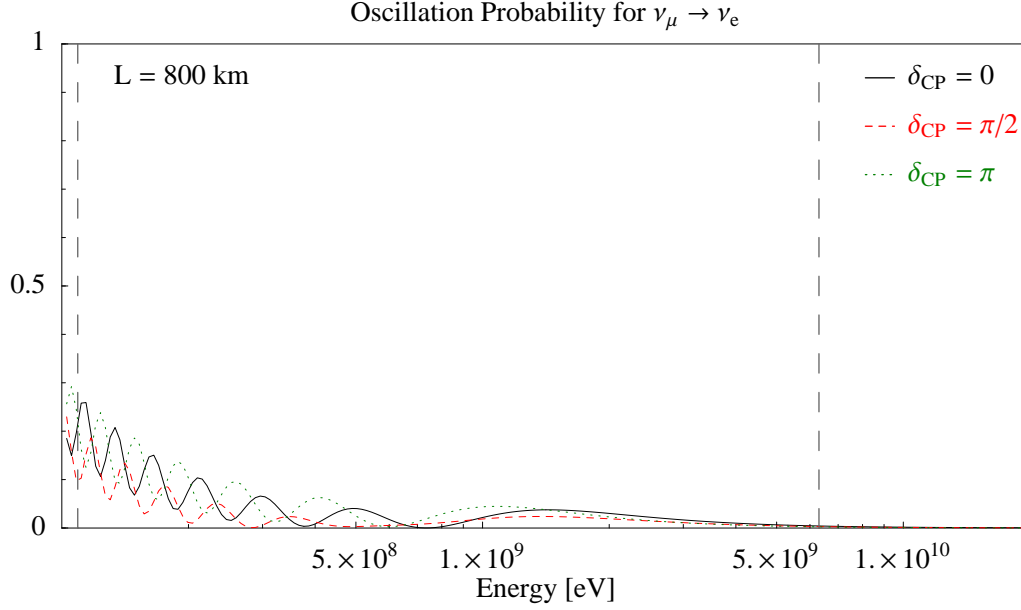


Figure 4.4: CP violation in the  $\nu_\mu \rightarrow \nu_e$  channel. The values of the oscillation parameters are the same as in Fig. 4.1.

full expression in the energy and baseline range considered here:

$$P_{\mu e} = \alpha^2 \sin^2 2\theta_{12} c_{23}^2 \frac{\sin^2 A\Delta}{A^2} + 4s_{13}^2 s_{23}^2 \frac{\sin^2(A-1)\Delta}{(A-1)^2} + 2\alpha s_{13} \sin 2\theta_{12} \sin 2\theta_{23} \cos(\Delta + \delta_{CP}) \frac{\sin A\Delta}{A} \frac{\sin(A-1)\Delta}{A-1}. \quad (4.10)$$

As long as matter effects are small, i.e.  $A \ll 1$ , as is the case here, this simplifies to

$$P_{\mu e} = \alpha^2 \Delta^2 \sin^2 2\theta_{12} c_{23}^2 + 4s_{13}^2 s_{23}^2 \sin^2 \Delta + \alpha \Delta s_{13} \sin 2\theta_{12} \sin 2\theta_{23} [\sin(2\Delta + \delta_{CP}) - \sin \delta_{CP}], \quad (4.11)$$

so CP violation modifies the atmospheric oscillations by introducing a phase shift and a constant offset. For the normal mass hierarchy, the phase shifted contribution interferes constructively with the  $\sin^2 \Delta$  term for  $\delta_{CP}$  around  $-\pi/2$ , while the interference is destructive for  $\delta_{CP} \approx +\pi/2$ . The inverted mass hierarchy can be introduced in Eq. (4.11) by replacing  $2\Delta + \delta_{CP}$  by  $2|\Delta| + \pi - \delta_{CP}$  in the phase shifting term. This implies that the oscillation probability remains unchanged for  $\delta_{CP} = \pm\pi/2$ , while the effects of the phase shifted contribution at  $\delta_{CP} = 0$  and  $\delta_{CP} = \pi$  are interchanged.

For both mass hierarchies, the constant shift  $-\alpha\Delta s_{13} \sin 2\theta_{12} \sin \delta_{CP}$  is negative for  $0 < \delta_{CP} < \pi$ , and positive otherwise.

For high energies (and short baselines), the factor  $\alpha\Delta$  in the last term of Eq. (4.10) becomes small, so CP violation becomes negligible there.

Let us emphasize that although both  $\delta_{CP} = 0$  and  $\delta_{CP} = \pi$  correspond to no CP violation (the Hamiltonian is real in both cases), the oscillation probability is not the same for these two cases. Furthermore, our discussion shows that a distinction between the normal and inverted mass hierarchy is in principle possible even in vacuum.

Note that in Eq. (4.10),  $\delta_{CP}$  enters only in the term proportional to both  $\alpha$  and  $s_{13}$ . The proportionality to  $s_{13}$  is already present in Eq. (2.29). If on the other hand  $\alpha$  is set to zero, the mass eigenstates  $|\nu_1\rangle$  and  $|\nu_2\rangle$  are degenerate, so  $\theta_{12}$  is meaningless and can be chosen to be zero. Then  $\delta_{CP}$  can be absorbed by changing the phase of  $|\nu_e\rangle$  by  $-\delta_{CP}$  and that of  $|\nu_1\rangle$  by  $\delta_{CP}$ . This transformation modifies  $U_{PMNS}$  of Eq. (2.28) in the following way:

$$\begin{aligned} U_{PMNS} &= \begin{pmatrix} e^{i\delta_{CP}} & & \\ & 1 & \\ & & 1 \end{pmatrix} \begin{pmatrix} 1 & & \\ & c_{23} & s_{23} \\ & -s_{23} & c_{23} \end{pmatrix} \begin{pmatrix} c_{13} & & s_{13} e^{-i\delta_{CP}} \\ & 1 & \\ -s_{13} e^{i\delta_{CP}} & & c_{13} \end{pmatrix} \begin{pmatrix} e^{-i\delta_{CP}} & & \\ & 1 & \\ & & 1 \end{pmatrix} \\ &= \begin{pmatrix} 1 & & \\ & c_{23} & s_{23} \\ & -s_{23} & c_{23} \end{pmatrix} \begin{pmatrix} c_{13} & s_{13} \\ & 1 \\ -s_{13} & c_{13} \end{pmatrix}, \end{aligned} \quad (4.12)$$

so no complex phase is left in the mixing matrix.

For the experimental measurement of  $\delta_{CP}$  it is important to keep in mind that CP violation can be mimicked by a variation in the other parameters. For example, a deficit in the total event rate around the first atmospheric maximum could be attributed either to CP violation or to a smaller value of  $\theta_{13}$ . This type of correlations is a severe limitation to future neutrino oscillation experiments.

#### 4.2.4 Matter of varying density and the PREM profile

For many scenarios, the approximation of constant matter density is not valid. Such scenarios are for example neutrino propagation in stars or supernovae, but also in the Earth if the baseline is very long, as is the case e.g. for upward going atmospheric neutrinos. The matter density profile of the Earth is shown in Fig. 4.5. It is taken from the Preliminary Reference Earth Model PREM [47], which is based on worldwide seismological data. The model divides the Earth into several layers with different physical properties, in particular with different matter densities. For neutrino oscillations, the most important feature is the transition from the mantle to the core at a radius of about  $R_{\text{core}} = 3480$  km, where  $\rho$  changes abruptly from  $5.5 \text{ g cm}^{-3}$  to  $10 \text{ g cm}^{-3}$ . A simple geometrical argument reveals that neutrinos can only pass through the core for baselines

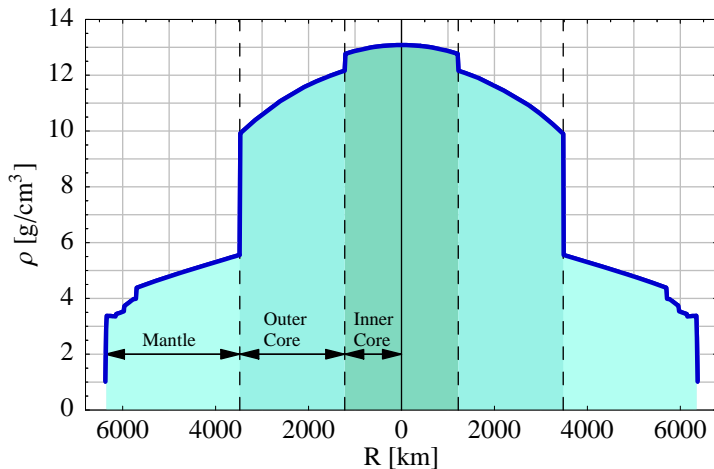


Figure 4.5: The Earth matter density profile as given by the Preliminary Reference Earth Model [47]. The boundary of the core is clearly visible as the steep density step at around  $R_{\text{core}} = 3480$  km.

$L^2 > 4(R_{\text{Earth}}^2 - R_{\text{core}}^2) = 10,673$  km, which is only slightly shorter than the Earth diameter  $2R_{\text{Earth}} = 12,742$  km.

The effects of the core transition on  $\nu_\mu \rightarrow \nu_e$  oscillations are shown in the black curve in Fig. 4.6. This curve has been calculated numerically by dividing the neutrino trajectory into small sections with a length of 10 km, over which the matter density was assumed to be constant. Equivalently one could also directly solve the Schrödinger equation numerically as discussed in appendix A. For a more efficient calculation as well as for an analytical discussion, it is however desirable to simplify the problem. Therefore we show in Fig. 4.6 two approximations to the oscillation probability using only three layers of constant density: Two for the mantle, and one for the core in between. In the “simple” model (green dotted curve), the mantle and core densities have the constant values  $\rho_{\text{mantle}} = 4.66$  g cm $^{-3}$  and  $\rho_{\text{core}} = 11.84$  g cm $^{-3}$ , which are the averages over the respective parts of Fig. 4.5. In the optimized model (red dashed curve),  $\rho_{\text{mantle}}$  and  $\rho_{\text{core}}$  are calculated specifically for the chosen baseline by averaging the PREM profile along the actual neutrino trajectory. For  $L = 2R_{\text{Earth}}$ , the two models would consequently be identical. For comparison, we also show the oscillation probability in matter of constant density  $\rho = 4.66$  g cm $^{-3}$ .

To understand the properties of Fig. 4.6 analytically, we will consider a three-layer approximation in a two-flavour system. This is reasonable above the solar resonance, but we want to emphasize that effects proportional to  $\alpha$  can still change the probabilities at the atmospheric resonance by several percent. If we denote quantities associated with the mantle layers by an index 1, and those associated with the core by an index 2, the

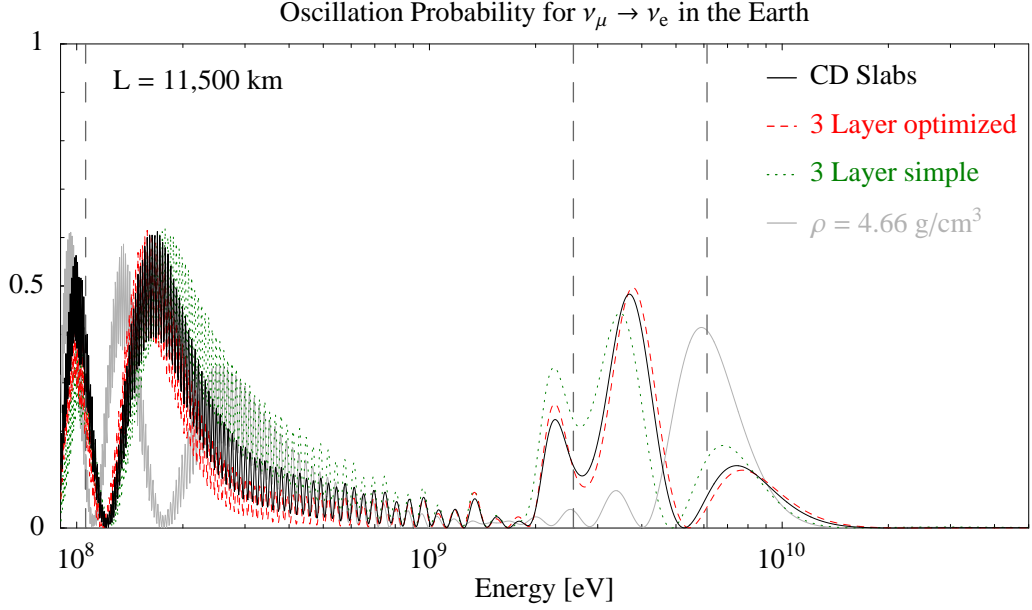


Figure 4.6: Neutrino oscillation probabilities for the  $\nu_\mu \rightarrow \nu_e$  channel in the Earth. We compare the accurate treatment using small slabs of constant density (black curve) with the optimized and simplified three-layer approximations (dashed red and dotted green curves), and with the oscillation probabilities for constant matter density  $\rho = 4.66 \text{ g cm}^{-3}$ . The vertical lines indicate the positions of the resonances in the core (left) and in the mantle (right). The values of the oscillation parameters are the same as in Fig. 4.1.

oscillation probability is given by (see appendix C)

$$\begin{aligned}
 P = & (1 - P_1)^2 P_2 + 2(1 - P_1)(1 - 2P_2)P_1 + P_1^2 P_2 \\
 & + 4(1 - 2P_1) \sin 2\theta_1 \sin 2\theta_2 \sin \Delta_1 \sin \Delta_2 (\cos \Delta_1 \cos \Delta_2 - \cos 2\theta_1 \cos 2\theta_2 \sin \Delta_1 \sin \Delta_2) \\
 & + P_1 \left[ \frac{1}{2}(1 + \cos^2 2\theta_1)(1 + \cos^2 2\theta_2) \cos 2\Delta_1 \cos 2\Delta_2 \right. \\
 & \quad + \frac{1}{2} \sin^2 2\theta_1 \sin^2 2\theta_2 - 2 \cos 2\theta_1 \cos 2\theta_2 \sin 2\Delta_1 \sin 2\Delta_2 \\
 & \quad \left. + \frac{1}{2} \sin^2 2\theta_1 (1 + \cos^2 2\theta_2) \cos 2\Delta_2 + \frac{1}{2} \sin^2 2\theta_2 (1 + \cos^2 2\theta_1) \cos 2\Delta_1 \right].
 \end{aligned} \tag{4.13}$$

Here,  $\theta_1$  and  $\theta_2$  are the effective mixing angles in matter, and  $\Delta_j = \Delta m_j^2 L_j / 4E$  is the oscillation phase acquired in layer  $j$ , which depends on  $\Delta m_j^2$ , the effective mass squared difference in matter of density  $\rho_j$ .  $P_j = \sin^2 2\theta_j \sin^2 \Delta_j$  denotes the oscillation

probability in each individual layer.

Equation (4.13) can be understood as follows: If we assume that coherence is lost at the mantle-core transitions, so that the neutrino is brought to a pure flavour eigenstate at these points, we would have from combinatorics

$$P_{\text{incoherent}} = (1 - P_1)^2 P_2 + 2(1 - P_1)(1 - P_2)P_1 + P_1^2 P_2, \quad (4.14)$$

i.e. either the flavour changes in the core, but not in the mantle, or it does not change in the core, but in exactly one of the two mantle layers (hence the factor of 2), or there is a flavour transition in all three layers. Since in reality coherence is not lost in the transitions, the interference terms proportional to  $1 - 2P_1$  and  $P_1$  appear, and the term  $2(1 - P_1)(1 - P_2)P_1$  acquires an extra factor of 2 in the second set of braces.

From Eq. (4.14) one expects that there should now be two atmospheric MSW resonances, one for the mantle density, and one for the core density. The positions of these resonances are indicated by the vertical dashed grey lines in Fig. 4.6. However, since the individual path lengths in the mantle and core are small,  $L_1 < 5340$  km and  $L_2 < 7000$  km, the oscillation probabilities at the resonances remain small as well:  $P_2 \lesssim 0.5$  and  $P_1 \lesssim 0.3$ . This implies that the triple products in Eq. (4.14), especially the ones containing  $P_1$  as a factor, will remain small. Indeed, without the interference terms the mantle resonance would reduce to a mere plateau on the high energy tail of the oscillation probability.

The fact that  $P_1$  remains relatively small ensures however that the interference term proportional to  $(1 - 2P_1)$  can get sizeable around the resonances, where  $\sin 2\theta_1$  and  $\sin 2\theta_2$  are large. But even the term proportional to  $P_1$  can contribute significantly since it contains only one factor of  $P_1$ . The interplay of these terms is quite complicated, but they generally cause the maximum transition probability to lie between the two resonances and produce strong oscillatory patterns around this maximum.

Below the resonances, the interference terms can modify the already small  $\theta_{13}$  oscillations. Although the interplay of the different terms in this region is again very complex, it is reasonable that a beat-like structure emerges, since  $\theta_1$  and  $\theta_2$  as well as  $\Delta_1$  and  $\Delta_2$  are numerically very similar there. Indeed, a beat is superimposed on the oscillations in Fig. 4.6 between 0.5 GeV and 2.0 GeV.

Note that in the limit of equal matter densities  $\rho_1 = \rho_2$ , i.e.  $\theta_1 = \theta_2$ , one can show that Eq. (4.13) reduces to the normal two-flavour probability in matter of constant density,  $\sin^2 2\theta_1 \sin^2(2\Delta_1 + \Delta_2)$ .

If we compare the predictions of the different models shown in Fig. 4.6, we note that the simple three-layer model reproduces the behaviour in the resonance region qualitatively, but the magnitude of the enhancement is off by several percent. The optimized model is also quantitatively quite accurate. In the sub-GeV region, the oscillation probability in the simple model is again too large, while in the optimized model it is too low. The behaviour in this region is very sensitive to slight changes in the baseline or in the oscillation parameters, so it cannot be generalized.

In Fig. 4.7, we compare the above models over a wider range of baselines and energies, and for different values of  $\sin^2 2\theta_{13}$ . The left column shows the oscillation probability  $P_{\nu_\mu \rightarrow \nu_e}$  in the accurate model of constant density slabs, while the other columns contain absolute differences of  $P_{\nu_\mu \rightarrow \nu_e}$  to the approximations in the optimized three-layer model, the simplified three-layer model, and in a constant density calculation. As expected, the optimized three-layer model, in which  $\rho_{\text{mantle}}$  and  $\rho_{\text{core}}$  are calculated individually for each baseline, gives the best approximation for all  $E$  and  $L$ , although even in this model the errors can reach 5 – 10% in the low energy regime slightly above the solar resonance, and at the atmospheric resonance for large  $\sin^2 2\theta_{13}$ . It is interesting to note that also for baselines for which no core transition occurs, the errors can be sizeable, which indicates that the variation of  $\rho$  inside the mantle can be important.

The behaviour of the simplified three-layer model with constant values for  $\rho_{\text{mantle}}$  and  $\rho_{\text{core}}$  is essentially the same except in the atmospheric resonance region at very long baselines. If  $L$  is so large that the neutrino trajectory traverses the core, and if  $\sin^2 2\theta_{13}$  is sizeable, the errors introduced by this model can be above 10%. At  $L \approx 8,500$  km, however, the simplified model is even better than the optimized one because there, the errors introduced by assuming the same  $\rho_{\text{mantle}}$  for all trajectories happen to compensate those stemming from the negligence of density variations within the mantle.

The approximation of constant density is equivalent to the simple three-layer approximation for baselines that do not pass through the core. For larger baselines, it is very inaccurate because it completely neglects core-transition effects.

## 4.3 The $\nu_\mu \rightarrow \nu_\tau$ channel

### 4.3.1 Three-flavour effects in vacuum

To discuss oscillations in the  $\nu_\mu \rightarrow \nu_\tau$  channel, let us again begin by considering the vacuum case. For simplicity we will assume  $\theta_{13} = 0$ . As there is no resonant enhancement in vacuum, this will also be a good approximation for non-vanishing, but small  $\theta_{13}$ . According to [9], the oscillation probability is then given by

$$P_{\mu\tau}^{\text{vac}} = s_{12}^2 \sin^2 2\theta_{23} \sin^2 \Delta + c_{12}^2 \sin^2 2\theta_{23} [\sin^2(1 - \alpha)\Delta - s_{12}^2 \sin^2 \alpha\Delta], \quad (4.15)$$

with the usual notation from Eq. (4.1). Equation (4.15) is plotted as the solid black curve in Fig. 4.8. The first term describes atmospheric oscillations driven by  $\Delta m_{31}^2$ , the last term describes solar oscillations driven by  $\Delta m_{21}^2$ . The middle term contains both frequencies and interferes with the two other terms. This leads to the small “bumps” at the lower edge of the enveloping curve and influences the overall amplitude of the solar oscillations, which is *not*  $\sin^2 2\theta_{12}$  here.

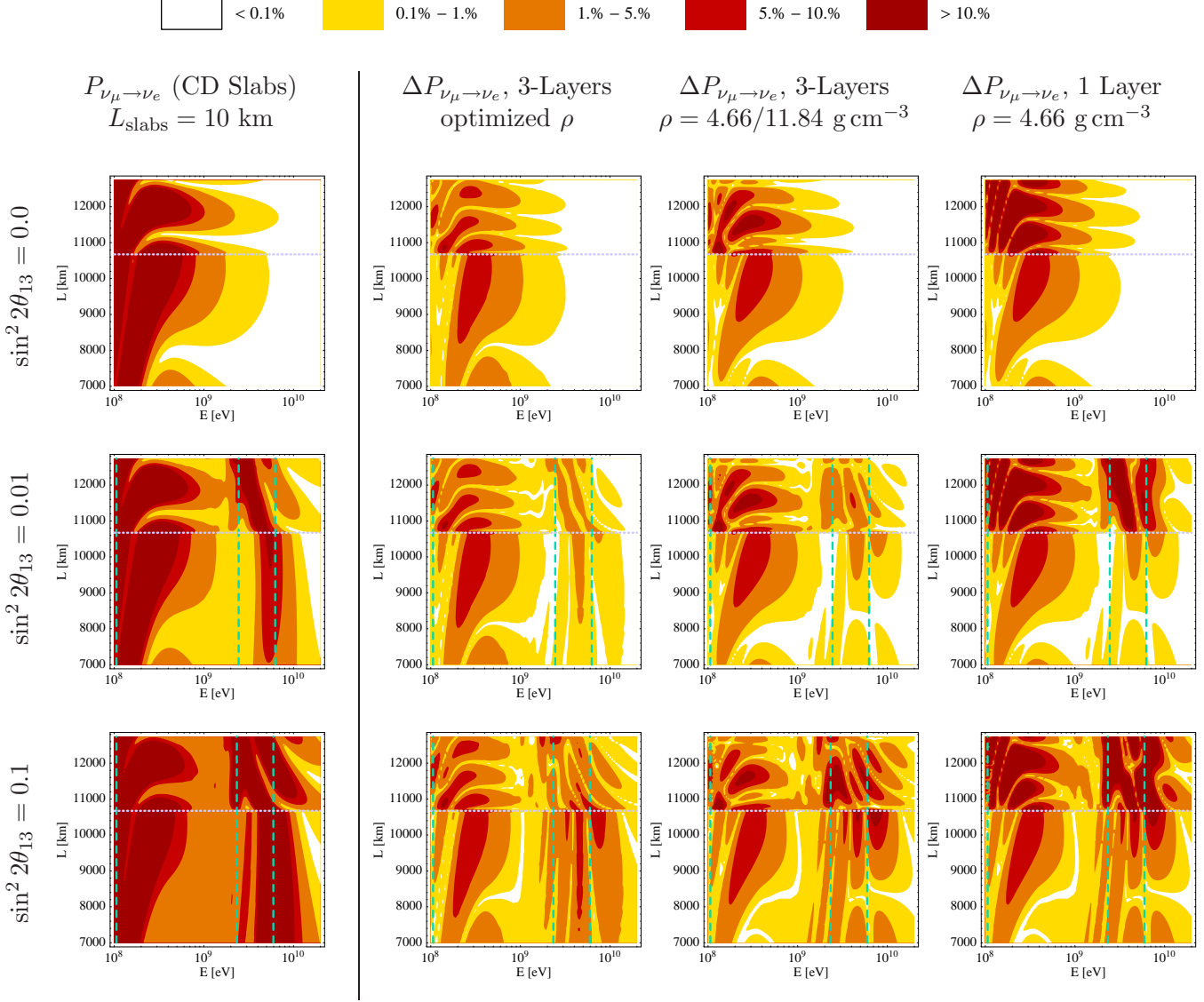


Figure 4.7: Accuracy of different approximations to the  $\nu_\mu \rightarrow \nu_e$  neutrino oscillation probabilities in the Earth. The leftmost column shows the exact probability  $P_{\nu_\mu \rightarrow \nu_e}$ , while the other columns show its differences  $\Delta P_{\nu_\mu \rightarrow \nu_e}$  to the probabilities calculated with the approximations discussed in the text. All probabilities have been folded with a 10% Gaussian energy smearing function. The vertical lines indicate the positions of the mantle and core resonances, the horizontal line shows the minimum baseline for which core transition occurs. The values of the oscillation parameters are the same as in Fig. 4.1.

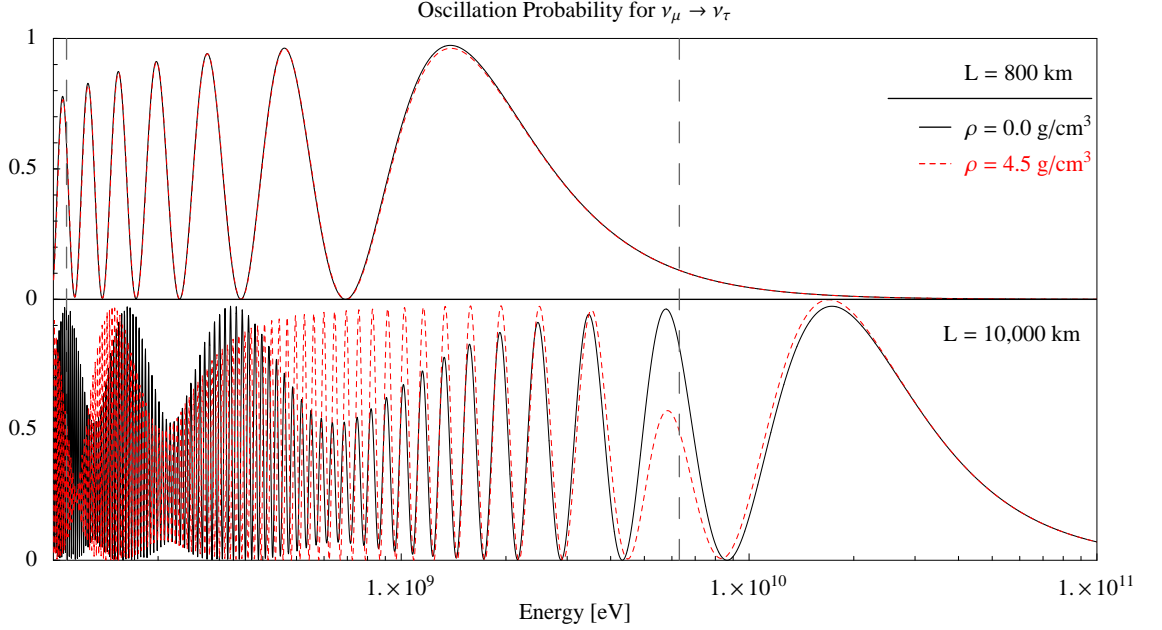


Figure 4.8: The three-flavour oscillation probability for the  $\nu_\mu \rightarrow \nu_\tau$  channel as a function of the energy. The vertical grey lines indicate the positions of the solar and atmospheric resonances. For the oscillation parameters, we have chosen the same values as in Fig. 4.1.

### 4.3.2 Three-flavour effects in matter of constant density

Matter effects in the  $\nu_\mu \rightarrow \nu_\tau$  channel are generic three-flavour effects, for according to the discussion in Sec. 2.2, the amplitude for coherent forward scattering is the same for  $\nu_\mu$  and  $\nu_\tau$ , i.e. in a two-flavour system matter could not affect the oscillation probabilities.

The red curve in Fig. 4.8 shows how  $\nu_\mu \rightarrow \nu_\tau$  oscillations in matter differ from those in vacuum. For energies well below the atmospheric resonance, it is again convenient to neglect  $\theta_{13}$ :

$$P_{\mu\tau}^{\text{mat}} \approx \sin^2 2\theta_{23} \sin^2(-\alpha C_{12} + A + \alpha - 2)\Delta + \cos^2 \theta_{12}^m \sin^2 2\theta_{23} \left[ \sin^2(\alpha C_{12} + A + \alpha - 2)\frac{\Delta}{2} - \sin^2 \theta_{12}^m \sin^2 \alpha C_{12} \Delta \right]. \quad (4.16)$$

Comparison of eqs. (4.16) and (4.15) shows that in matter, the frequency of the atmospheric term is slightly shifted by the potential  $A$  and by a contribution of the solar frequency. In the solar term, the frequency remains unchanged, but the amplitude is now given by the mixing angle in matter,  $\theta_{12}^m$ . This explains why solar oscillations are stronger than in the vacuum case for energies close to the solar resonance at

$E_{\text{sol}} = \cos 2\theta_{12}\Delta m_{21}^2/2V$ , but vanish completely for energies far above the resonance, where  $\theta_{12}^m \rightarrow 0$ . The interference term now has a slightly different frequency as well, and its amplitude contains  $\theta_{12}^m$  instead of  $\theta_{12}$ .

At the baseline shown in Fig. 4.8, the transition probability in matter is suppressed around the atmospheric resonance energy  $E_{\text{atm}} = \cos 2\theta_{13}\Delta m_{31}^2/2V$  [48–50], while for higher energies a slight enhancement occurs. Since solar oscillations are suppressed here, we can approximate  $P_{\mu\tau}$  by neglecting  $\alpha$  [9]:

$$P_{\mu\tau}^{\text{mat}} \approx \frac{1}{2} \sin^2 2\theta_{23} \left[ (1 - \cos 2\theta_{13}^m) \sin^2(1 + A - C_{13}) \frac{\Delta}{2} + (1 + \cos 2\theta_{13}^m) \sin^2(1 + A + C_{13}) \frac{\Delta}{2} - \frac{1}{2} \sin^2 2\theta_{13}^m \sin^2 C_{13}\Delta \right]. \quad (4.17)$$

If  $\theta_{13}$  were zero, the first and the last terms in Eq. (4.17) would vanish, so that two-flavour atmospheric oscillations would be recovered. For non-vanishing  $\theta_{13}$ , all three terms compete, and strong effects are to be expected around the resonance. To estimate the magnitude of these effects for a wider range of baselines, let us consider the quantity  $\Delta P_{\mu\tau} = P_{\mu\tau}^{\text{mat}} - P_{\mu\tau}^{\text{vac}}$ . Around the resonance, we have  $\sin 2\theta_{13}^m \approx 1$  and  $A \approx 1$ , so  $\Delta P_{\mu\tau}$  is given by

$$\Delta P_{\mu\tau}(E = E_{\text{atm}}) = \frac{1}{2} \sin^2 2\theta_{23} \left[ \sin^2(2 - C_{13}) \frac{\Delta}{2} + \sin^2(2 + C_{13}) \frac{\Delta}{2} - \frac{1}{2} \sin^2 C_{13}\Delta \right] - \sin^2 2\theta_{23} \sin^2 \Delta \quad (4.18)$$

$$= \sin^2 2\theta_{23} \left( \frac{1}{2} \left[ 1 - \frac{1}{2} \cos(2 - C_{13})\Delta - \frac{1}{2} \cos(2 + C_{13})\Delta - \frac{1}{2} \sin^2 C_{13}\Delta \right] - \frac{1}{2} + \frac{1}{2} \cos 2\Delta \right) \quad (4.19)$$

$$= \sin^2 2\theta_{23} \left( \frac{1}{2} \cos 2\Delta - \frac{1}{2} \cos 2\Delta \cos C_{13}\Delta - \frac{1}{4} \sin^2 C_{13}\Delta \right) \quad (4.20)$$

$$= \sin^2 2\theta_{23} \left( \cos 2\Delta \sin^2 \frac{C_{13}\Delta}{2} - \frac{1}{4} \sin^2 C_{13}\Delta \right) \quad (4.21)$$

This expression for  $\Delta P_{\mu\tau}$  is plotted in Fig. 4.9. It is a superposition of fast oscillations with length  $4\pi E/\Delta m_{31}^2$  (solid black curve), and slow oscillations with length  $8\pi E/C_{13}\Delta m_{31}^2$  (dotted blue curve). Positive values of  $\Delta P_{\mu\tau}$  correspond to an enhancement of the flavour transition probability, while negative values indicate a suppression.

It can be read off from Eq. (4.21) that matter effects can only be sizeable if  $C_{13}\Delta \approx (2n+1)\pi$  and  $2\Delta \approx \frac{2n+1}{2}\pi$ , where  $n$  is a non-negative integer. Since  $C_{13} \approx \sin 2\theta_{13} \ll 1$  at the resonance, this can only be fulfilled for baselines larger than the diameter of the Earth. For the value  $\sin^2 2\theta_{13} = 0.05$  which was chosen here, the maximum transition probability occurs at around 30,000 km. If  $\theta_{13}$  is close to the CHOOZ bound, a suppression of 70% can occur even inside the Earth. Since this suppression will occur only

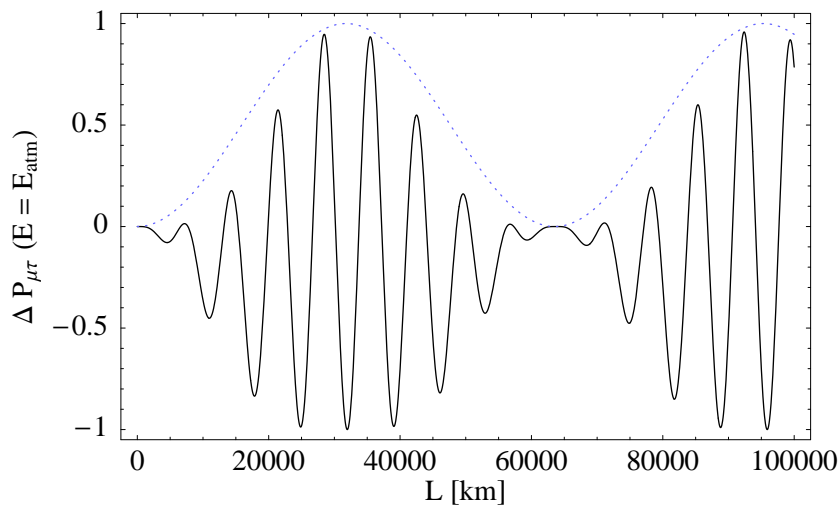


Figure 4.9: Magnitude of matter effects in the  $\nu_\mu \rightarrow \nu_\tau$  channel at the atmospheric resonance energy (black curve), and the enveloping oscillation term  $\sin^2 C_{13} \Delta/2$  (dotted blue curve). The values of the oscillation parameters are the same as in Fig .4.1

for neutrinos or only for antineutrinos, depending on  $\text{sign}(\Delta m_{31}^2)$ , it has been proposed to search for it in future atmospheric neutrino experiments [50] and thus determine the mass hierarchy. However we believe that this is quite ambitious because the effect is constrained to a small energy window, so large statistics and a very good energy resolution will be required. A megaton water Čerenkov detector could provide the necessary statistics, but its energy resolution is too limited to identify the effect in a statistically significant way. Furthermore, it is much easier to identify the mass hierarchy by looking for the resonance in the  $\nu_e$  appearance channel.

# Chapter 5

## Prospects of future neutrino oscillation experiments

### 5.1 Reactor neutrinos

Nuclear reactors are a great tool to study neutrinos because they provide a very high flux and are easily accessible. Consequently, it was at a nuclear reactor that the neutrino has first been discovered [51, 52]. The usefulness of reactor neutrinos for oscillation physics is limited by their low energy of only several MeV, which is below the threshold for CC  $\bar{\nu}_\mu$  and  $\bar{\nu}_\tau$  interactions, so that an observation of the  $\bar{\nu}_e \rightarrow \bar{\nu}_\mu$  or  $\bar{\nu}_e \rightarrow \bar{\nu}_\tau$  appearance channels is impossible, and one has to rely on a  $\bar{\nu}_e$  disappearance measurement.

Nevertheless, there are many plans for new reactor neutrino experiments aiming at the measurement of the small mixing angle  $\theta_{13}$ . They all have in common that the main detector is planned to be located at a distance of 1 to 2 km from the reactor core, which corresponds roughly to the first atmospheric oscillation maximum (cf. Fig. 4.1). The detector material is usually some liquid scintillator.

#### 5.1.1 Systematical errors

##### General discussion

Since the aim of a  $\theta_{13}$  reactor experiment is to measure a tiny deviation of the oscillation probability from unity, it is crucial that experimental errors are under control. Otherwise an observed deficit in the neutrino flux might be attributed either to oscillations or to experimental errors. Statistics is not a problem due to the high flux, but systematical errors can be large. In particular the information about the initial neutrino flux and spectrum, which can be obtained from thermal measurements at the power station, and from theoretical models, is only accurate up to a few percent, which is not sufficient to achieve the desired sensitivity to  $\sin^2 2\theta_{13}$  of better than  $\mathcal{O}(10^{-2})$ . Therefore, the next generation of experiments will employ a dedicated near detector, located close to the reactor core, to directly measure the unoscillated flux and spectrum.

The near and far detectors should be as similar as possible, so that most uncertainties associated with the detectors will cancel as well. The most important of these are

the interaction cross sections, the properties of the liquid scintillator, and the spill-in/spill-out effect. The latter occurs if the neutrino interaction takes place inside the fiducial volume, but the reaction products escape the fiducial volume, or vice-versa. The cancellation does not work for systematical errors that are uncorrelated between the two detectors, such as the relative normalization and energy calibration, and some backgrounds.

To study the impact of systematical errors quantitatively we have performed detailed simulations with the GLOBES software [37], which we have modified in order to allow an appropriate treatment of systematical uncertainties. To measure the potential of future experiments, we consider their sensitivity to  $\sin^2 2\theta_{13}$ , which is defined as in chapter 3 as the limit that an experiment can set to  $\sin^2 2\theta_{13}$ , assuming the true value is zero. To obtain it, we compare the event rates for  $\theta_{13} = 0$  with those for a non-zero test value in a detailed  $\chi^2$  analysis. For the numerical simulation, we assume the events to follow a Poisson distribution, but for illustrative purposes it is sufficient to work with the Gaussian approximation, which is very good due to the large event rates in typical reactor experiments. For a near/far setup,  $\chi^2$  has the form

$$\chi^2 = \sum_{A=N,F} \sum_{i=1}^{n_{\text{bins}}} \frac{1}{N_i^A} [T_i^A(\theta_{13}; a_{\text{norm}}, a_{\text{det}}^A, a_{\text{shape},i}, a_{\text{bkg}}, b) - N_i^A]^2 + \frac{a_{\text{norm}}^2}{\sigma_{\text{norm}}^2} + \frac{(a_{\text{det}}^N)^2}{\sigma_{\text{det}}^2} + \frac{(a_{\text{det}}^F)^2}{\sigma_{\text{det}}^2} + \frac{a_{\text{bkg}}^2}{\sigma_{\text{bkg}}^2} + \sum_{i=1}^{n_{\text{bins}}} \frac{a_{\text{shape},i}^2}{\sigma_{\text{shape}}^2} + \frac{b^2}{\sigma_b^2}. \quad (5.1)$$

Here,  $N_i^N$  and  $N_i^F$  denote the observed event numbers in the  $i$ -th energy bin at the near and far positions, respectively. These event rates are calculated with GLOBES assuming the values given in table 5.1 for the solar and atmospheric oscillation parameters, and  $\theta_{13} = 0$ . Correspondingly,  $T_i^A$  are the theoretically predicted event rates for non-zero  $\theta_{13}$  and certain systematical biases, which we denote by  $a_{\text{norm}}$ ,  $a_{\text{det}}^A$ ,  $a_{\text{shape},i}$ ,  $a_{\text{bkg}}$ , and  $b$ . In principle, also the solar and atmospheric oscillation parameters should be allowed to differ from their “true” values in the fit, but we have checked that minimizing  $\chi^2$  over them within the allowed ranges from other experiments does not change the results of our simulations. This is in accordance with ref. [53]. The second line of Eq. (5.1) contains pull terms which represent prior knowledge about the systematical biases by giving a large penalty to values that are much larger than the estimated systematical uncertainties. In detail, we introduce the flux normalization uncertainty  $\sigma_{\text{norm}}$ , which is correlated between the near and far detectors because it is associated with the reactor flux, the uncorrelated detector normalization errors  $\sigma_{\text{det}}$ , and a correlated background flux error  $\sigma_{\text{bkg}}$ . Furthermore, to account for uncertainties in the reactor neutrino spectrum, we introduce a shape error  $\sigma_{\text{shape}}$  which is independent for each energy bin, so  $a_{\text{shape}}$  gets an index  $i$ . Finally, we consider an energy calibration error  $\sigma_b$ . The dependence of  $T_i^A$

Parameter	Value
$\sin^2 2\theta_{23}$	1.000
$\sin^2 2\theta_{12}$	0.788
$\sin^2 2\theta_{13}$	0.000
$\delta_{CP}$	0.000
$\Delta m_{21}^2$	$8.1 \cdot 10^{-5} \text{ eV}^2$
$\Delta m_{31}^2$	$2.2 \cdot 10^{-3} \text{ eV}^2$

Table 5.1: Default values for the oscillation parameters used in our simulations.

on these parameters is given by

$$T_i^A = (1 + a_{\text{norm}} + a_{\text{det}}^A + a_{\text{shape},i}) \tilde{S}_i^A(\theta_{13}; b) + (1 + a_{\text{bkg}} + a_{\text{det}}^A) \tilde{B}_i^A(b), \quad (5.2)$$

where  $\tilde{S}_i^A(\theta_{13}; b)$  and  $\tilde{B}_i^A(b)$  are the signal and background rates for the wrong energy binning implied by non-zero  $b$ . They are obtained from the correctly binned rates  $S_i^A$  and  $B_i^A$  according to

$$\tilde{S}_i^A(\theta_{13}; b) = (1 + b) [(S_{[\delta]+1}(\theta_{13}) - S_{[\delta]}(\theta_{13}))(\delta - \lfloor \delta \rfloor) + S_{[\delta]}(\theta_{13})], \quad (5.3)$$

$$\delta = b \cdot (i + t_0 + \frac{1}{2}) + i, \quad (5.4)$$

and a similar expression for  $B_i^A$  (see also ref. [53]). The quantity  $t_0$  in Eq. (5.4) is the energy threshold of the detector, expressed in units of the bin width. We have used the Gauss bracket  $\lfloor \cdot \rfloor$  to denote the floor function. The expression in square brackets in Eq. (5.3) is essentially a linear interpolation between the events in bin  $\lfloor \delta \rfloor$  and those in bin  $\lfloor \delta \rfloor + 1$ . If  $b$  is not too large, the energy calibration never changes by more than the bin width, so that  $\lfloor \delta \rfloor = i$ . The factor  $(1 + b)$  in front accounts for the change of the bin width implied by  $b$ .

### Analytical derivation of the sensitivity to $\sin^2 2\theta_{13}$

Before discussing the results of our numerical simulations, let us first discuss the impact of systematical errors analytically and consider a simplified version of Eq. (5.1),

$$\begin{aligned} \chi^2 = & \sum_i \frac{1}{N_i^F} [N_i^F (1 + a_{\text{norm}} + a_{\text{det}}) (1 - \sin^2 2\theta_{13} \sin^2 \Delta_i) - N_i^F]^2 \\ & + \sum_i \frac{1}{N_i^N} [N_i^N (1 + a_{\text{norm}}) - N_i^N]^2 + \frac{a_{\text{norm}}^2}{\sigma_{\text{norm}}^2} + \frac{a_{\text{det}}^2}{\sigma_{\text{det}}^2}, \end{aligned} \quad (5.5)$$

where we have for simplicity neglected backgrounds, energy calibration and spectral errors. Furthermore, we have absorbed  $a_{\text{det}}^N$  into  $a_{\text{norm}}$  and kept only a relative detector

normalization bias  $a_{\text{det}}$  for the far detector. This is always possible without loss of generality if we adjust  $\sigma_{\text{norm}}$  and  $\sigma_{\text{det}}$  correspondingly. Finally, we have inserted the oscillation probability  $P_{ee}$  in the two-flavour approximation in terms of the oscillation phase  $\Delta_i = \Delta m_{31}^2 L/4E_i$ , which depends on the far detector baseline  $L$  and the neutrino energy  $E_i$ .

Since  $a_{\text{norm}}$ ,  $a_{\text{det}}$  and  $\sin^2 2\theta_{13}$  are small, Eq. (5.5) can be approximated by

$$\chi^2 = \sum_i N_i^F [a_{\text{norm}} + a_{\text{det}} - \sin^2 2\theta_{13} \sin^2 \Delta_i]^2 + \sum_i N_i^N a_{\text{norm}}^2 + \frac{a_{\text{norm}}^2}{\sigma_{\text{norm}}^2} + \frac{a_{\text{det}}^2}{\sigma_{\text{det}}^2}. \quad (5.6)$$

$a_{\text{norm}}$  and  $a_{\text{det}}$  are unknown, so we have to assume the worst case, i.e. minimal  $\chi^2$ . Therefore, we calculate

$$\frac{\partial \chi^2}{\partial a_{\text{norm}}} = 2 \sum_i N_i^F [a_{\text{norm}} + a_{\text{det}} - \sin^2 2\theta_{13} \sin^2 \Delta_i] + 2 \sum_i N_i^N a_{\text{norm}} + 2 \frac{a_{\text{norm}}}{\sigma_{\text{norm}}^2}, \quad (5.7)$$

$$\frac{\partial \chi^2}{\partial a_{\text{det}}} = 2 \sum_i N_i^F [a_{\text{norm}} + a_{\text{det}} - \sin^2 2\theta_{13} \sin^2 \Delta_i] + 2 \frac{a_{\text{det}}}{\sigma_{\text{det}}^2}, \quad (5.8)$$

and require these expressions to vanish. The near detector baseline is much shorter than that of the far detector, so the  $1/L^2$  dependence of the flux implies  $N_i^N \gg N_i^F$ . Therefore we can neglect the first and last terms in Eq. (5.7), and are left with

$$a_{\text{norm}} = 0, \quad (5.9)$$

i.e. the reactor flux normalization error drops out as expected. From Eq. (5.8), we then obtain for the fit value of  $a_{\text{det}}$ :

$$a_{\text{det}} = \sin^2 2\theta_{13} \frac{\sum_i N_i^F \sin^2 \Delta_i}{\sum_i N_i^F + 1/\sigma_{\text{det}}^2} \quad (5.10)$$

Inserting eqs. (5.9) and (5.10) into Eq. (5.6) yields

$$\chi^2 = \sin^4 2\theta_{13} \sum_i N_i^F \left[ \frac{\sum_j N_j^F \sin^2 \Delta_j}{\sum_j N_j^F + 1/\sigma_{\text{det}}^2} - \sin^2 \Delta_i \right]^2 + \frac{1}{\sigma_{\text{det}}^2} \left( \frac{\sum_j N_j^F \sin^2 \Delta_j}{\sum_j N_j^F + 1/\sigma_{\text{det}}^2} \right)^2. \quad (5.11)$$

The  $1\sigma$  range of  $\sin^2 2\theta_{13}$  is given by the requirement  $\chi^2 = 1$ , so we have

$$\sigma(\sin^2 2\theta_{13}) = \left[ \sum_i N_i^F \left[ \frac{\sum_j N_j^F \sin^2 \Delta_j}{\sum_j N_j^F + 1/\sigma_{\text{det}}^2} - \sin^2 \Delta_i \right]^2 + \frac{1}{\sigma_{\text{det}}^2} \left( \frac{\sum_j N_j^F \sin^2 \Delta_j}{\sum_j N_j^F + 1/\sigma_{\text{det}}^2} \right)^2 \right]^{-1/2}. \quad (5.12)$$

Different contributions dominate in this expression, depending on the magnitude of  $N_i^F$ :

- **Very low statistics.** As long as  $\sum_i N_i^F \ll 1/\sigma_{\text{det}}^2$ , Eq. (5.12) reduces to

$$\sigma(\sin^2 2\theta_{13}) \Big|_{\text{Low Stat.}} = \frac{1}{\sqrt{\sum_i N_i^F \sin^4 \Delta_i}} \quad (5.13)$$

because  $\sin^2 \Delta_i \approx 1$  at the far detector location, while all other terms are suppressed by the smallness of  $\sigma_{\text{det}}^2$ . Note that the same result is obtained for a systematics-free experiment with  $\sigma_{\text{det}} = 0$ . Therefore we call Eq. (5.13) the statistical limit.

- **Moderate statistics.** As soon as  $\sum_i N_i^F$  gets comparable to  $1/\sigma_{\text{det}}^2$ , all terms begin to contribute. Now, the first and second terms in the inner square brackets can partly cancel, thus reducing  $\chi^2$  and increasing  $\sigma(\sin^2 2\theta_{13})$ . This cannot be fully compensated by the last term, because this term cannot exceed  $1/\sigma_{\text{det}}^2$ .
- **Very high statistics.** If  $\sum_i N_i^F \gg 1/\sigma_{\text{det}}^2$ , all terms containing  $1/\sigma_{\text{det}}^2$  can be neglected, and Eq. (5.12) reduces to

$$\sigma(\sin^2 2\theta_{13}) \Big|_{\text{High Stat.}} = \left[ \sum_i N_i^F \left[ \frac{\sum_j N_j^F \sin^2 \Delta_j}{\sum_j N_j^F} - \sin^2 \Delta_i \right]^2 \right]^{-1/2}. \quad (5.14)$$

This means that for very high exposure, the sensitivity again follows  $1/\sqrt{N}$  and is independent of the exact value of  $\sigma_{\text{det}}$ , as long as the latter is so large that the condition  $\sum_i N_i^F \gg 1/\sigma_{\text{det}}^2$  is fulfilled. The physical explanation for this phenomenon is that the sensitivity is dominated by spectral information here. The first term in the inner square brackets is essentially  $\langle \sin^2 \Delta \rangle$ , averaged over energy. This average oscillation term is compared to the  $\sin^2 \Delta_i$  of each individual bin. The spectral distortion caused by neutrino oscillations will therefore increase  $\chi^2$  and lower  $\sigma(\sin^2 2\theta_{13})$ .

## Numerical simulation

In Fig. 5.1 we show the sensitivity to  $\sin^2 2\theta_{13}$  as a function of the neutrino luminosity in the far detector, obtained from a numerical simulation and using a full  $\chi^2$  expression similar to Eq. (5.1). The dashed curve shows the sensitivity that could be obtained if only the statistical uncertainties were present, i.e. if all the  $\sigma$ 's in Eq. (5.1) were very close to zero. The curve exhibits the  $1/\sqrt{N}$  scaling that is expected from Eq. (5.13). For the thick black curve, we include  $\sigma_{\text{norm}}$ ,  $\sigma_{\text{det}}^A$ , and  $\sigma_b$ , which leads to a deviation from the statistical limit. For luminosities above  $10^3$  GW t years, the thick curve scales again with  $1/\sqrt{N}$ , corresponding to the second statistically dominated regime described by Eq. (5.14). In the logarithmic plot, the distance between the purely statistical dashed

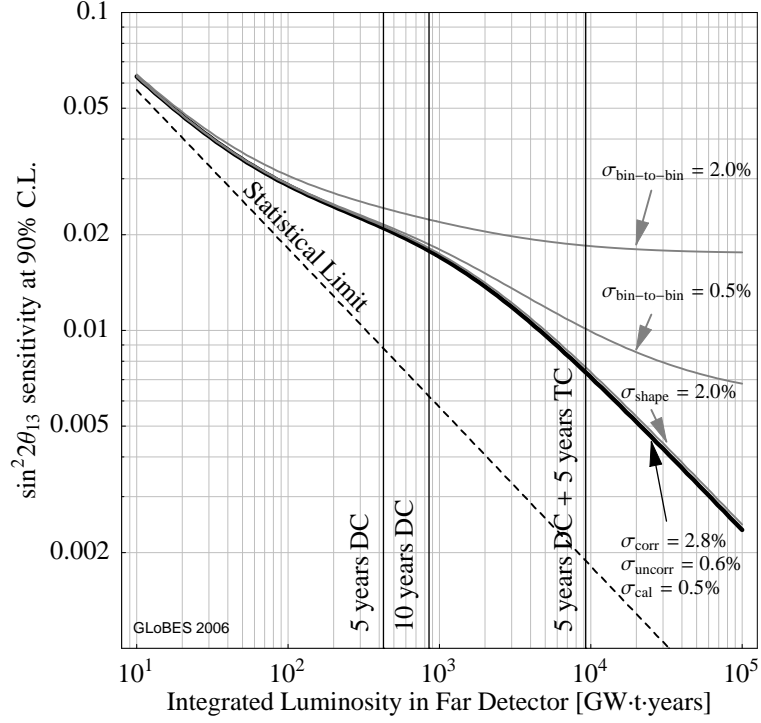


Figure 5.1: The impact of systematical errors on the  $\sin^2 2\theta_{13}$  sensitivity of a reactor experiment with identical near and far detectors. The sensitivity limit at the 90% confidence level is shown as a function of the total luminosity in the far detector. The vertical lines indicate the exposures that can be achieved in the Double Chooz experiment and its possible upgrade Triple Chooz. Here, we still neglect the delayed startup of the near detector in Double Chooz, and the different baselines of the two far detectors in Triple Chooz.

curve and the spectral regime of the thick black curve is constant because, on linear scales, the quotient  $\sigma(\sin^2 2\theta_{13})|_{\text{High Stat.}}/\sigma(\sin^2 2\theta_{13})|_{\text{Low Stat.}}$  is constant, as can be read off from eqs. (5.13) and (5.14).

The lower grey curve in Fig. 5.1 shows that  $\sigma_{\text{shape}}$  is irrelevant because it is correlated between the two detectors and therefore cancels in the near/far setup. The two upper grey curves show the effect of completely uncorrelated bin-to-bin errors  $\sigma_{\text{bin-to-bin}}$ , which can be used to account for backgrounds of unknown spectral shape. They are introduced in Eq. (5.1) just like  $\sigma_{\text{shape}}$ , but as they are independent for both detectors,  $a_{\text{bin-to-bin}}^A$  receives an index  $A$ . These errors are the ultimate limitation for reactor neutrino experiments, so they should be under control in order to achieve a good sensitivity.

		Correlated	Time-dependent	Value for DC
1	Reactor flux normalization	yes	yes	2.0%
2	Reactor spectrum	yes	yes	2.0% per bin
3	Cross Sections	yes	no	2.0%
4	Scintillator Properties	yes	no	
5	Spill-in/spill-out	yes	no	
6	Fiducial mass	no	no	0.6%
7	Detector normalization	no	yes	
8	Analysis cuts	no	no	
9	Energy calibration	no	yes	0.5%
10	Backgrounds	partly	partly	1.0%

Table 5.2: Systematical errors in Double Chooz (see text for details). The second column indicates which errors are correlated between near and far detector while the third column classifies which effects are time-dependent. The fourth column gives specific values we assume for Double Chooz. Table taken from ref. [36] and based on information from [35].

### 5.1.2 Double Chooz and Triple Chooz

We will now apply our results from the previous section to the Double Chooz experiment, which is currently the most advanced reactor neutrino project. Both detectors have a fiducial mass of 10.16 tons of liquid scintillator and are located at baselines of about 0.1 km and 1.05 km from the Chooz reactor complex, which has a thermal power of 8.4 GW. This leads to an expectation of 19,333 events per year in the far detector and  $1.071 \cdot 10^6$  events in the near detector. Table 5.2 gives typical values for the systematical errors. In Double Chooz, an additional complication arises from the fact that the near detector will start operation about 1.5 years after the far detector. Therefore only those systematical errors which are correlated between both detectors *and* which are not time-dependent can be fully eliminated. As can be read off from table 5.2, this is true for the errors in the cross sections, the properties of the scintillator, and the spill-in/spill-out effects. However, it does not apply to the uncertainties in the reactor flux and spectrum.

To incorporate this complication in the simulation, we divide our  $\chi^2$  function into separate parts for phase I, where only the far detector is running, and phase II, where both detectors are taking data. Therefore, the index  $A$  now runs over three values:  $F_I$ ,  $F_{II}$  and  $N$ , where the individual contributions are similar to those in Eq. (5.1). To account for the time dependence of the reactor normalization, we introduce in phase II (i.e. for  $A = F_{II}, N$ ) an additional parameter  $a_{\text{drift}}$  with an error of  $\sigma_{\text{drift}} = 1\%$  per year of delay. Furthermore, we neglect  $\sigma_{\text{shape}}$  in phase II, as Fig. 5.1 shows that it becomes irrelevant as soon as both detectors are taking data.

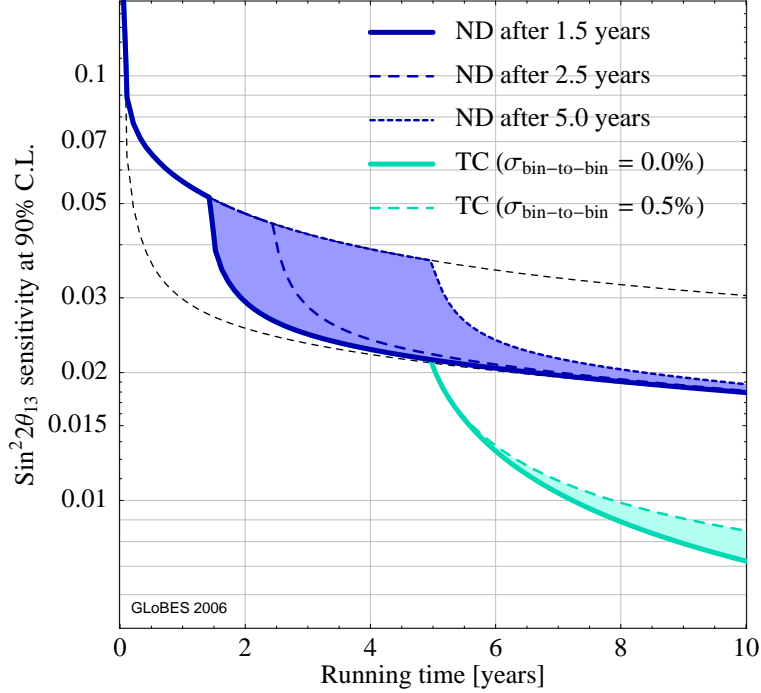


Figure 5.2: The  $\sin^2 2\theta_{13}$  sensitivity limit at the 90% C.L. for Double Chooz alone and for a Triple Chooz upgrade after 5 years. The blue curves correspond to different starting times of the near detector. The dashed cyan curve shows how Triple Chooz is affected by bin-to-bin errors. Figure taken from ref. [36].

The evolution of the  $\sin^2 2\theta_{13}$  sensitivity limit as a function of the running time is shown in Fig. 5.2. The plot illustrates how the sensitivity improves as soon as the near detector becomes available. However, even for very late starting times, the sensitivity will quickly reach the limit that would be obtained if the near detector were operational from the beginning (lower thin dashed black curve). This is due to the fact that Double Chooz has a luminosity in the systematics-dominated regime of Fig. 5.1 (between  $10^2$  GW t years and  $10^3$  GW t years), where the total number of events is not a problem, but spectral information is still statistically limited. This effect is even more pronounced in Fig. 5.2 due to the linear scale on the horizontal axes.

Figure 5.2 also shows the sensitivity that can be obtained by upgrading Double Chooz to Triple Chooz after 5 years by the construction of a second far detector with a fiducial mass of 200 t. This detector could be constructed in an existing cavern at a baseline of 1 km from the reactor cores. Although it will need to have a different design than the original Double Chooz detectors and will therefore introduce larger systematical errors

(we take  $\sigma_{\text{fid}} = 1\%$  and  $\sigma_{\text{cal}} = 1\%$ ), it can greatly improve the sensitivity. The reason is that it lifts the event rates to the second statistics dominated regime in Fig. 5.1, where spectral information gets dominant. Of course, for such a high exposure, bin-to-bin errors can be fatal. The thin dashed cyan curve in Fig. 5.2 shows however, that for the reasonable assumption of  $\sigma_{\text{bin-to-bin}} = 0.5\%$ , they are still tolerable, though not negligible.

## 5.2 Atmospheric neutrinos

### 5.2.1 General discussion

Atmospheric neutrinos cover a wide range of energies, and travel distances of up to  $2R_{\text{Earth}} \approx 12,742$  km before reaching the detector. Therefore, one might expect from Fig. 4.8 that solar as well as atmospheric oscillations should appear in the data.

That this is not the case is due to a triple conspiracy: Firstly, atmospheric neutrinos do not constitute a pure  $\nu_\mu$  beam, but contain an admixture of  $\nu_e$  which can oscillate into  $\nu_\mu$ , thereby washing out the  $\nu_\mu$  disappearance effect. For energies of several 100 MeV, where solar oscillations might be relevant, the flux ratio is  $\Phi(\nu_\mu)/\Phi(\nu_e) \approx 2$  because the dominant production process of atmospheric neutrinos, Eq. (3.1), yields two muon neutrinos and one electron neutrino for each primary proton. Therefore the  $\nu_\mu$  event rate in the detector can be expressed schematically as

$$N_\mu \propto 1 - P_{\text{solar}} - P_{\text{atm}} + \frac{1}{2}P_{\text{solar}}, \quad (5.15)$$

where the first three terms give  $P_{\mu\mu}$ , and the last one is essentially  $P_{e\mu} \cdot \Phi(\nu_e)/\Phi(\nu_\mu)$ .

Secondly, the energy and angular resolution of Super-Kamiokande does not permit to resolve the atmospheric oscillation maxima and minima in the relevant energy range around several 100 MeV, so the atmospheric oscillations average out,

$$N_\mu \propto \frac{1}{2} \sin^2 2\theta_{23}(1 - P_{\text{solar}}) + \frac{1}{2}P_{\text{solar}}. \quad (5.16)$$

Thirdly, as atmospheric mixing is close to maximal, this averaging will exactly compensate the  $\nu_e \rightarrow \nu_\mu$  oscillations, and we end up with the event rate

$$N_\mu \propto \frac{1}{2}. \quad (5.17)$$

This is however identical to what would be expected if solar oscillations were absent.

Let us now put this argument into a more mathematical form. Neglecting  $\theta_{13}$ , we

have

$$N_\mu \propto \Phi_e P_{e\mu} + \Phi_\mu (1 - P_{\mu e} - P_{\mu\tau}) \quad (5.18)$$

$$\begin{aligned} &\approx \Phi_\mu \left( \frac{1}{2} c_{23}^2 \sin^2 2\theta_{12}^m \sin^2 \alpha C_{12} \Delta + 1 - c_{23}^2 \sin^2 2\theta_{12}^m \sin^2 \alpha C_{12} \Delta \right. \\ &\quad \left. - \frac{1}{2} \sin^2 2\theta_{23} \left[ 1 - \frac{1}{2} \sin^2 2\theta_{12}^m \sin^2 \alpha C_{12} \Delta - \cos(\alpha C_{12} + A + \alpha - 2)\Delta \right. \right. \\ &\quad \left. \left. - (1 - \cos 2\theta_{12}^m) \sin \alpha C_{12} \Delta \sin(A + \alpha - 2)\Delta \right] \right) \quad (5.19) \end{aligned}$$

$$\begin{aligned} &= \Phi_\mu \left( \frac{1}{2} + \frac{1}{2} \cos(\alpha C_{12} + A + \alpha - 2)\Delta \right. \\ &\quad \left. + \frac{1}{2} (1 - \cos 2\theta_{12}^m) \sin \alpha C_{12} \Delta \sin(A + \alpha - 2)\Delta \right). \quad (5.20) \end{aligned}$$

In the second line, we have used  $\Phi(\nu_\mu)/\Phi(\nu_e) \approx 2$ , and in the third line we have inserted  $\theta_{23} \approx \pi/4$ . The last two terms in Eq. (5.20) oscillate with a frequency that is close the atmospheric one below 1 GeV, so, due to the limited experimental resolution, they will average out to zero, and the heuristic result from Eq. (5.17) is recovered.

A similar calculation for  $N_e$  yields

$$N_e \propto \Phi_e P_{ee} + \Phi_\mu P_{\mu e} \quad (5.21)$$

$$\approx \Phi_e \left( 1 - \sin^2 2\theta_{12}^m \sin^2 \alpha C_{12} \Delta + 2c_{23}^2 \sin^2 2\theta_{12}^m \sin^2 \alpha C_{12} \Delta \right) \quad (5.22)$$

$$= \Phi_e. \quad (5.23)$$

This triple conspiracy is lifted for  $E_\nu$  above several GeV because there, the initial flux ratio is different from 2. At such high energies, the muons produced in pion decay (Eq. (3.1)) can reach the ground before decaying. By interactions with the Earth, they lose energy, so that the electron neutrinos produced in their decays will have lower energy. Therefore one might hope to see the strong three-flavour effects around the atmospheric resonance.

A future megaton water Čerenkov detector such as Hyper-Kamiokande [54], MEMPHYS [55], or UNO [56] could achieve excellent statistics due to its large mass. However, if such a detector is built, it will be a multi-purpose detector which will also be used for accelerator neutrino experiments. Therefore, the question arises, whether the atmospheric background can be separated from the beam neutrinos. This is however possible due to directional and timing information: Beam neutrinos come from a known direction, and they arrive in short spills, with large intervals in between. Any high-energy neutrino coming from a different direction, or between two beam spills, must have an atmospheric origin. Therefore we believe that it is worthwhile to study the information that can be obtained from atmospheric neutrinos in future large detectors.

In this work, we will concentrate on the potential of atmospheric neutrinos alone, but we remark that a combined analysis of atmospheric and beam data can be very profitable [57]. We will consider two types of experiments:

- The existing Super-Kamiokande experiment, located in the Kamioka mine in the centre of Honshu Island, Japan. Super-Kamiokande is currently the world's largest water Čerenkov detector with a total mass of 50 kt of water.
- The ATLAS experiment at Cern in Geneva, Switzerland. ATLAS is one of the large multi-purpose detectors at the LHC accelerator, and will start operation in 2007. Of course, ATLAS is not built for neutrino physics and cannot detect the rare neutrino events as long as LHC is running, but during the winter, when the accelerator is shut down, it should be possible to modify the trigger systems in such a way that the experiment can look for atmospheric neutrino interactions. The total mass of ATLAS is 7 kt, so a reasonable number of neutrino interactions can be expected in the detector. We will focus on  $\nu_\mu$  interacting in the massive calorimeters, because for these, the energy of all interaction products is visible, and the secondary muon direction is precisely measured in the muon chambers, so that a good energy and angular resolution can be achieved. Furthermore, the magnetic field allows muon charge identification, i.e. one can distinguish  $\nu_\mu$  from  $\bar{\nu}_\mu$ . To obtain a reasonably pure neutrino sample it is crucial to efficiently reject the cosmic muon background, which is large due to the low overburden of only 55 m of rock. However, this should not be a problem since the excellent ATLAS muon system provides a very good veto.

Note that the other large LHC experiment, CMS, should be able to detect even more atmospheric neutrinos than ATLAS due to its larger mass of 12 kt. However, most neutrino interactions in CMS will take place in the iron return yokes of the magnetic field, so the interaction products will get scattered before hitting the active detector components and the resolution will be much worse than in ATLAS. The other two LHC experiments, LHCb and ALICE are too small to contribute to neutrino physics.

### 5.2.2 Simulation of atmospheric neutrino experiments

To study the potential of current and future atmospheric neutrino experiments, we have developed a simulation program called INSANE (INstrument for the Simulation of Atmospheric Neutrino Experiments), which allows to calculate expected event rates, binned over energy and zenith angle, and to perform a  $\chi^2$  analysis of the simulated data, taking into account systematical errors, parameter correlations, and degeneracies. Many of the techniques employed in INSANE are based on those used in GLOBES [37] for the simulation of accelerator and reactor experiments, but they have been rewritten and adapted to the peculiarities of atmospheric neutrinos such as the angular dependence of

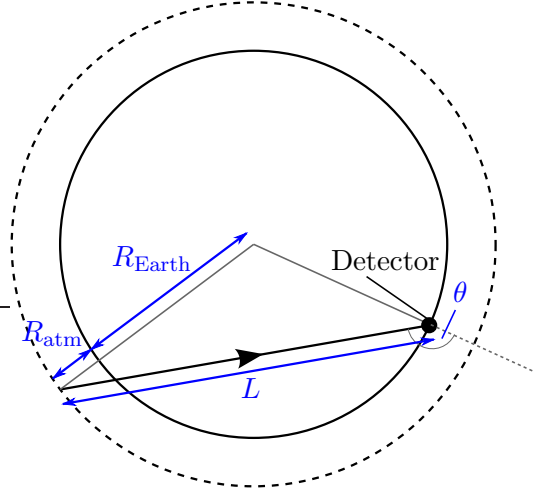


Figure 5.3: Illustration of the geometrical arguments leading to Eq. (5.25)

the fluxes and oscillation probabilities, and the possibility to analyse so-called upward going muon events (see below).

An oscillation analysis of atmospheric neutrinos is based on the energy and directional distribution of the events. We specify the direction by the “zenith angle”  $\theta$ , which is measured against the plumb line so that  $\theta_\nu = 0$  corresponds to vertically downward going neutrinos.  $\theta$  is related to the baseline  $L$  which the neutrino has travelled by the formula

$$(R_{\text{atm}} + R_{\text{Earth}})^2 = R_{\text{Earth}}^2 + L^2 + 2R_{\text{Earth}}L \cos \theta \quad (5.24)$$

$$\Leftrightarrow L = -R_{\text{Earth}} \cos \theta + \sqrt{R_{\text{Earth}}^2 \cos^2 \theta + R_{\text{atm}}^2 + 2R_{\text{atm}}R_{\text{Earth}}}, \quad (5.25)$$

where  $R_{\text{Earth}} = 6,371$  km is the Earth radius, and  $R_{\text{atm}}$  is the altitude at which the neutrinos are produced. Equation (5.25) follows from simple geometrical arguments based on the law of cosines (see Fig. 5.3).

We perform binning in  $E$  and  $\theta$ , and denote the number of events in the  $i^{\text{th}}$  energy bin and the  $j^{\text{th}}$  zenith angle bin by  $N_f^{ij}$ , where the index  $f$  indicates one of the six flavours  $e, \mu, \tau, \bar{e}, \bar{\mu}, \bar{\tau}$ . The starting point for the calculation of  $N_f^{ij}$  is the following formula:

$$N_f^{ij} = \mathcal{N} \int_{\text{bin } i,j} dE_r d\theta_r \int dE_l d\theta_l V_f(E_r, \theta_r, E_l, \theta_l) \cdot \int dE_\nu d\theta_\nu k_f(E_l, \theta_l, E_\nu, \theta_\nu) \sigma_f(E_\nu) \cdot$$

$$\sum_{f'=1}^3 P(f' \rightarrow f, E_\nu, L(\theta_\nu), \Theta) \Phi_{f'}(E_\nu, L(\theta_\nu)). \quad (5.26)$$

The last line of this expression describes neutrino production and oscillations, the second line the neutrino interaction, and the first line the detection process. Three different energy and zenith angle variables appear in Eq. (5.26):  $E_\nu$  and  $\theta_\nu$  are the parameters of the neutrino itself,  $E_l$  and  $\theta_l$  correspond to the secondary lepton which is produced in the neutrino interaction, and  $E_r$  and  $\theta_r$  are the reconstructed neutrino energy and direction, as obtained from the experiment. The initial flux is denoted by  $\Phi_{f'}(E_\nu, L(\theta_\nu))$ , the oscillation probability for the parameters  $\Theta = (\theta_{12}, \theta_{13}, \theta_{23}, \delta_{CP}, \Delta m_{21}^2, \Delta m_{31}^2)^T$  is given by  $P(f' \rightarrow f, E_\nu, L(\theta_\nu), \Theta)$ , and the interaction process is described by the cross section  $\sigma_f(E_\nu)$  and the distribution function of secondary leptons  $k_f(E_l, \theta_l, E_\nu, \theta_\nu)$ . The latter gives the probability that in the interaction of a neutrino with flavour  $f$ , energy  $E_\nu$ , and direction  $\theta_\nu$ , a lepton (of flavour  $f$ ) with energy  $E_l$  and direction  $\theta_l$  is produced. Analogously,  $V_f(E_r, \theta_r, E_l, \theta_l)$  gives the probability that a lepton with  $E_l, \theta_l$  gives a signal that is reconstructed as a neutrino with parameters  $E_r, \theta_r$ . The event rates are normalized by the factor  $\mathcal{N}$  which includes the detector mass and the exposure time.

Equation (5.26) is not suitable for an efficient numerical calculation because it contains a sixfold integration. We can avoid the integration over  $E_l$  and  $\theta_l$  by combining  $k_f$  and  $V_f$  to the detector response function

$$R(E_r, \theta_r, E_\nu, \theta_\nu) = \int dE_l d\theta_l V_f(E_r, \theta_r, E_l, \theta_l) \cdot k_f(E_l, \theta_l, E_\nu, \theta_\nu). \quad (5.27)$$

As our focus is on neutrino oscillations and not on the details of a specific detector, it is in general possible to use some rough approximation for  $R$  (see below). The integration over  $E_r$  and  $\theta_r$  has to be performed only once, yielding for each bin a function  $\tilde{R}^{ij}(E_\nu, \theta_\nu)$ , which gives the probability that the interaction of a neutrino with energy  $E_\nu$  and direction  $\theta_\nu$  will produce an event in bin  $(i, j)$ . The integration over  $E_\nu$  and  $\theta_\nu$  can finally be replaced by a sum, so that we have

$$N_f^{ij} = \sum_{k,l} \tilde{R}^{ij}(E_\nu^k, \theta_\nu^l) \cdot \sigma_f(E_\nu^k) \sum_{f'=1}^3 P(f' \rightarrow f, E_\nu^k, L(\theta_\nu^l), \Theta) \cdot \Phi_{f'}(E_\nu^k, L(\theta_\nu^l)). \quad (5.28)$$

One caveat of this approach is that we must make sure that the sampling of  $E_\nu$  and  $\theta_\nu$  does not produce aliasing effects.

Following the data analysis procedure of the Super-Kamiokande collaboration [58], we consider four different event samples, which are implemented by different detector response functions  $R$ . The fully contained (FC) sample contains events, for which the secondary lepton track lies completely inside the detector. For partially contained (PC) events, the primary vertex is located inside the fiducial volume, but the secondary lepton

leaves the detector. Also neutrinos interacting in the rock surrounding the detector can be seen, but a separation from the cosmic muon background is only possible if the secondary lepton is going upward. Such an event is therefore called upward stopping (US) or upward through-going (UT), depending on whether the lepton stops inside the detector or leaves it again. PC, US, and UT events can only originate from high energy muon neutrinos because the tracks of electrons and low energy muons are too short. A full energy reconstruction is not possible for these events, and we will only use their directional information in the analysis.

In the remainder of this section we will discuss in more detail the various parameters appearing in Eq. (5.28).

### Atmospheric neutrino fluxes

For the initial fluxes  $\Phi_{f'}(E_\nu, L(\theta_\nu))$ , we use the results of Honda et. al. [59]. Other calculations have been performed by Battistoni et. al. (“FLUKA fluxes”, [60]), and by Barr et. al. (“Bartol fluxes”, [61]). Their results are shown in figs. 5.4 and 5.5. The neutrino fluxes decrease rapidly with increasing energy due to the low flux of high energy cosmic rays. Note that the curves in the left panel of Fig. 5.4 have been multiplied with  $E_\nu^3$ ! The zenith angle distributions are peaked around  $\cos\theta = 0$  due to geometrical effects [62, 63].

The plots show that the predictions of different authors agree within about 10%. This remaining uncertainty originates mostly from the imperfect knowledge of the primary cosmic ray flux and of the hadronic interaction processes in the atmosphere. It will be taken into account in our discussion of systematical uncertainties in Sec. 5.2.3.

In the low energy region (up to a few GeV), the flux of primary cosmic rays is strongly affected by interactions with the solar wind and therefore varies with the eleven-year solar activity cycle [65]. At phases of maximum solar activity, the atmospheric neutrino flux is at a minimum, while for minimal solar activity, it reaches a maximum. Although this effect has to be taken into account when fitting actual experimental data, we will neglect it in our simulations and consistently use the fluxes for maximum solar activity and minimum neutrino flux.

Besides the dependence on the energy and the zenith angle  $\theta_\nu$ , the atmospheric neutrino fluxes also exhibit a dependence on the azimuthal angle  $\phi$  (the so-called east-west effect), which originates from the deflection of primary cosmic rays in the Earth magnetic field. For an oscillation analysis this  $\phi$ -dependence is irrelevant, because according to Eq. (5.25), the baseline  $L$ , which enters in the oscillation probability, depends only on  $\theta_\nu$ ,  $R_{\text{Earth}}$  and  $R_{\text{atm}}$ .

The production height of atmospheric neutrinos is taken to be 15 km above ground in INSANE, although in reality, it varies between 0 and 30 km. We neglect this variation because it is much smaller than the typical oscillation lengths, which are  $> 100$  km even for the lowest energy neutrinos ( $E_\nu \approx 100$  MeV) that can be seen in a detector like

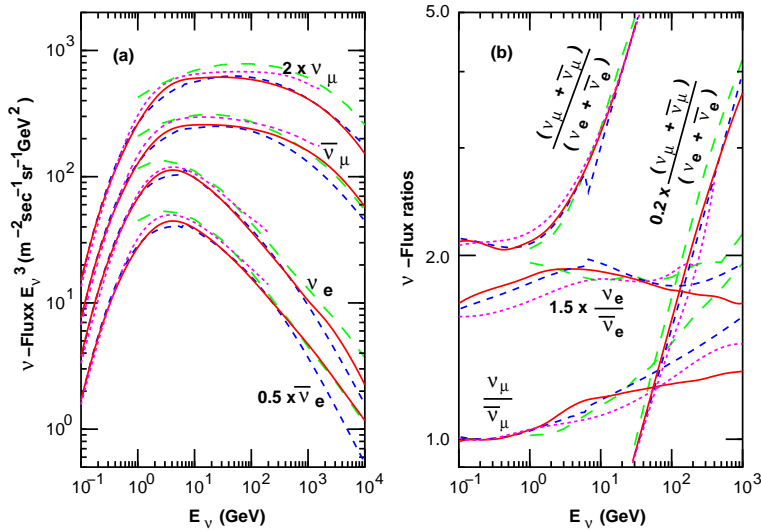


Figure 5.4: Theoretical predictions for the energy dependence of atmospheric neutrino fluxes (left panel) and of the flavour ratios (right panel). Solid red curves show the 2004 Honda fluxes [59], dotted magenta curves correspond to an older calculation by the same authors [64]; dashed blue lines are for FLUKA [60], and long dashed green lines for BARTOL [61]. Figure taken from ref. [59].

Super-Kamiokande.

### Cross sections

The cross sections for neutrino-nucleon interactions used in INSANE are based on works by Messier [66] and Paschos/Yu [67]. We use tabulated values which are also implemented in GLOBES and cover energies from 100 MeV to 1 TeV. For neutrinos with higher energies (up to 10 TeV), which can contribute only to the upward through-going muon sample, we extrapolate the cross sections by making the assumption that  $\sigma(E)/E$  is constant at such high energies. We only use charged current cross sections. The detailed calculation of these cross sections is highly non-trivial and well beyond the scope of this work, so we will only give a short qualitative overview. The main contributions are

- Quasi-elastic scattering (scattering off a whole nucleon):

$$\nu + N \rightarrow l + N', \quad (5.29)$$

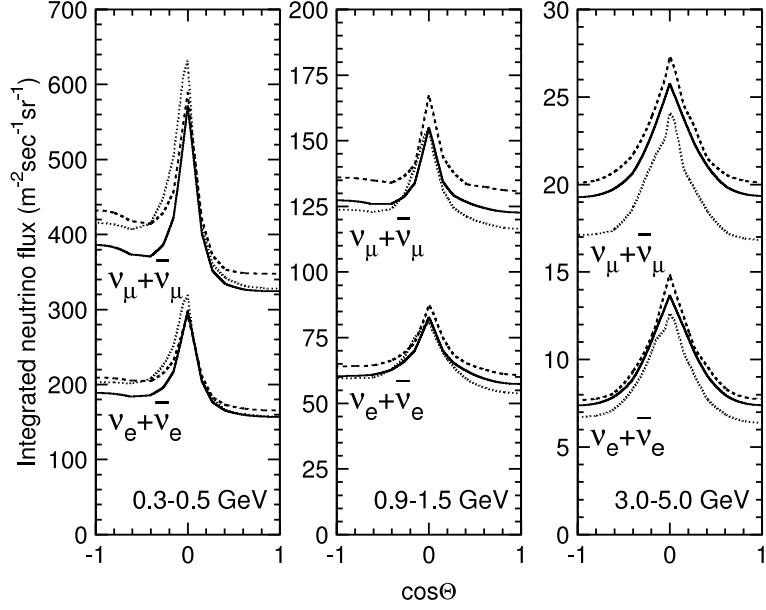


Figure 5.5: Theoretical predictions for the zenith angle dependence of atmospheric neutrino fluxes for three different energy windows. Solid lines are for Honda fluxes [59], dashed lines for FLUKA [60] and dotted lines for BARTOL [61]. Figure taken from ref. [58].

- Single-meson production:

$$\nu + N \rightarrow l + N' + \text{Meson}, \quad (5.30)$$

- Deep-inelastic scattering (scattering off a parton):

$$\nu + N \rightarrow l + N' + \text{Hadrons}, \quad (5.31)$$

where  $N$  and  $N'$  are the nucleons before and after the interaction, and  $l$  is a lepton of the same flavour as the initial neutrino.

The energy dependence of these contributions is illustrated in Fig. 5.6. Note that the cross sections for antineutrinos are much smaller than those for neutrinos. The data points shown in the plots are reasonably consistent with the theoretical predictions, but most of them have errors of at least several percent. Furthermore, experimental data is not available for all energies, especially for antineutrinos. Therefore we will have to make reasonable assumptions on the uncertainties in the cross sections when discussing systematical errors.

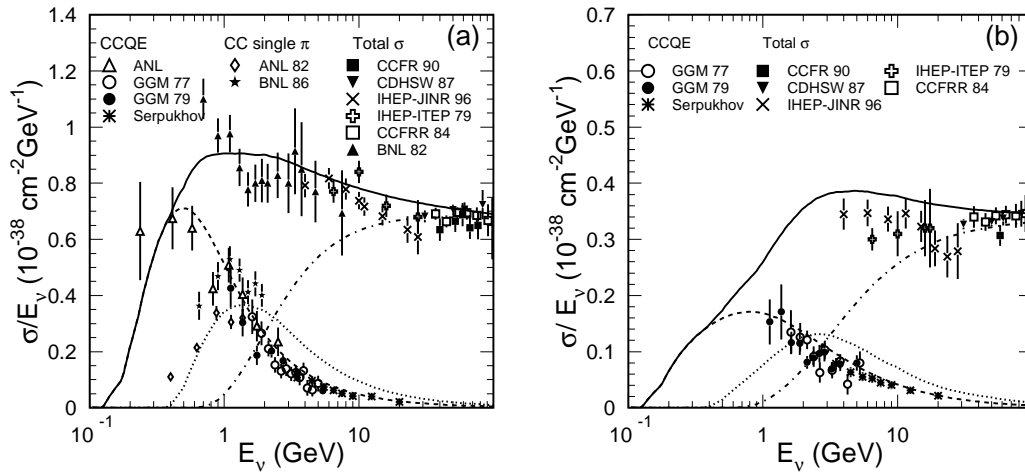


Figure 5.6: Charged current cross sections divided by  $E_\nu$  for (a) neutrinos and (b) antineutrinos interacting with nucleons. The solid lines are theoretical predictions for the total cross sections, which contain contributions from quasi-elastic scattering (dashed curves), single-meson production (dotted curves) and deep-inelastic scattering (dash-dotted curves). Figure taken from ref. [58]. See references therein for details on the experiments.

### Oscillation probabilities

Oscillation probabilities are calculated in a full three-flavour treatment, using a numerical algorithm that was specifically optimized for three-dimensional problems (see appendix A). To incorporate the earth matter density profile we use the optimized three-layer model that was discussed in Sec. 4.2.4. For the oscillation parameters, we use the standard values given in table 5.1. Unless stated otherwise we assume a normal mass hierarchy.

### The detector response function

The detector response function  $R(E_r, \theta_r, E_\nu, \theta_\nu)$  provides an abstract description of the properties of a neutrino detector, in particular the uncertainties it introduces in the energy and zenith angle reconstruction. Ideally,  $R$  is known to a reasonable accuracy from detector Monte Carlo (MC) simulations. However, as our purpose is to study the potential of future experiments, for which no MC simulations are yet existing, and of the already operational Super-Kamiokande experiment, for which the response function is not publicly available, we need to use some approximations for  $R$ . We parameterize

	Super-Kamiokande	ATLAS cons.	ATLAS real.	ATLAS opt.
$\sigma_E$ [%]	10.0	10.0	5.0	2.0
$\sigma_\alpha$ FC [°]	17.0 – 95.0	17.0 – 95.0	7.0	2.0
$\sigma_\alpha$ PC [°]	12.0	—	—	—
$\sigma_\alpha$ US [°]	9.0	—	—	—
$\sigma_\alpha$ UT [°]	3.0	9.0	9.0	9.0
$\epsilon^E/\epsilon^\theta$ FC	see Fig. 5.8/App. B	1.0 ( $\nu_\mu$ only)	1.0 ( $\nu_\mu$ only)	1.0 ( $\nu_\mu$ only)
$\epsilon^E/\epsilon^\theta$ PC	see Fig. 5.8/App. B	0.0	0.0	0.0
$\epsilon^E/\epsilon^\theta$ US	see App. B	0.0	0.0	0.0
$\epsilon^E/\epsilon^\theta$ UT	see App. B	see App. B	see App. B	see App. B

Table 5.3: Parameters of the detector response function for the different experiments discussed in the text.

$R$  as a double Gaussian, multiplied with detection efficiencies:

$$\begin{aligned}
 R(E_r, \theta_r, E_\nu, \theta_\nu) = & \epsilon^E(E_\nu) \epsilon^\theta(\theta_\nu) \cdot \frac{1}{Z_E} \exp\left(-\frac{(E_r - E_\nu)^2}{2\sigma_E^2(E_\nu)}\right) \\
 & \cdot \frac{1}{Z_\alpha} \int_0^{2\pi} d\phi_r \exp\left(-\frac{\alpha^2(\theta_r, \phi_r, \theta_\nu)}{2\sigma_\alpha^2(E_\nu)}\right). \quad (5.32)
 \end{aligned}$$

Here,  $\sigma_E(E_\nu)$  is the energy resolution,  $\sigma_\alpha(E_\nu)$  is the angular resolution, and

$$\alpha(\theta_r, \phi_r, \theta_\nu) = \arccos(\sin \theta_r \sin \theta_\nu \cos \phi_r + \cos \theta_r \cos \theta_\nu) \quad (5.33)$$

is the angle between directions  $(\theta_r, \phi_r)$  and  $(\theta_\nu, 0)$ . This is the only place where the azimuthal angle  $\phi$  is relevant in INSANE.  $Z_E$  and  $Z_\alpha$  are the normalization factors for the two exponential functions. The efficiencies are split into an energy dependent part  $\epsilon^E(E_\nu)$  and a zenith angle dependent part  $\epsilon^\theta(\theta_\nu)$ , the product of which describes the probability that a neutrino interaction within the detector is successfully reconstructed. For example, in Super-Kamiokande, the efficiency will be zero for very low energy neutrinos which cannot produce secondary leptons above the Čerenkov threshold.

Numerical values for the efficiencies and resolutions are given in tab. 5.3. For Super-Kamiokande we use angular resolutions based on ref. [58]. Fixed values are taken for PC, US, and UT events, while the angular resolution for FC events depends on the neutrino energy according to Fig. 5.7. As the plot shows that the resolutions for FC  $\nu_e$  events and FC  $\nu_\mu$  events are similar, we use the  $\nu_\mu$  resolutions for both flavours. The resolution is worse for low energy neutrinos because for these, the interaction kinematics are such that the angular correlation between the incident neutrino and the secondary lepton is very weak. For the energy resolution we assume a constant value of 10%.

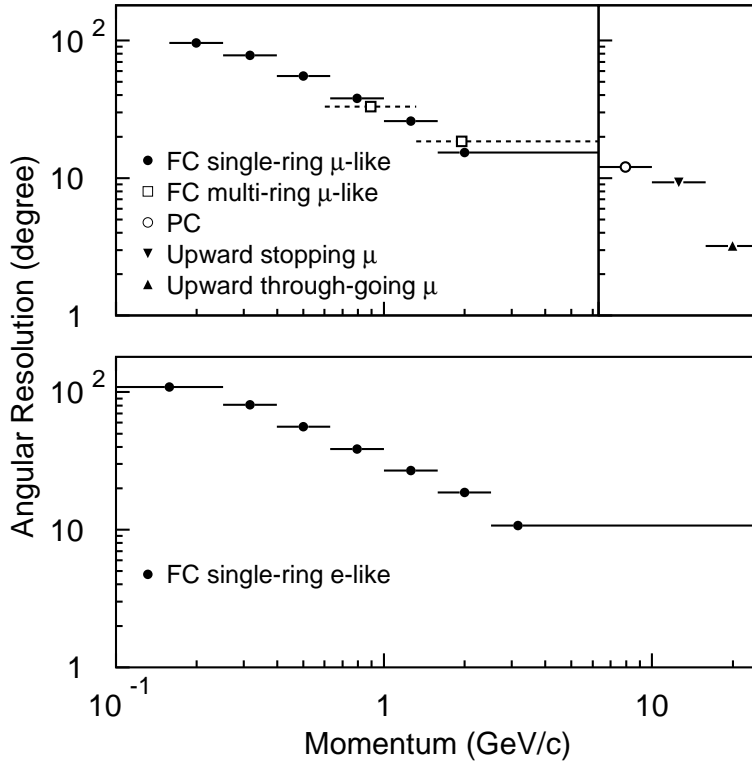


Figure 5.7: Angular resolution of Super-Kamiokande as a function of the secondary lepton energy (which we take equal to the neutrino energy for simplicity). The angular resolution is defined as the angular difference between the parent neutrino and the reconstructed direction for which 68% of the events are included. The resolutions for multi-ring events are not used in INSANE because we neglect this type of events. Figure taken from ref. [58].

The efficiencies are different for the different event samples — this is actually the way we separate the samples. The energy dependent factor  $\epsilon^E$  for FC and PC events in Super-Kamiokande is taken from detector Monte Carlo simulations [58, 68], while the angular dependent part  $\epsilon^\theta$  is calculated from geometrical arguments as described in appendix B. Unfortunately, Monte Carlo based efficiencies were only available for events containing a single Čerenkov ring, and since there is no easy way to estimate the efficiencies for multi-ring events, we do not include these in our analysis.

The efficiencies for US and UT events are calculated completely from the geometry. For these event samples, not only the reconstruction efficiency depends on  $E_\nu$  and  $\theta_\nu$ , but also the target mass, which is determined by the spatial volume from which neutrino-induced muons can reach the detector. Therefore, the upward muon efficiencies describe not only the separation of US and UT events, but also the relative normalization of US+UT to FC+PC events.

The efficiencies obtained for Super-Kamiokande are plotted in Fig. 5.8. For very low energies, all of them go to zero because a neutrino event can only be reconstructed if the secondary lepton is above the Čerenkov threshold. Since muons have a larger mass than electrons, this threshold is higher for muon neutrinos, so that the curve for FC  $\mu$ -like events starts out about 100 MeV above the one for  $e$ -like events. For intermediate energies, the FC efficiencies are quite high, but they decrease again as the energy goes above 1 GeV. This is because high energy neutrinos have a high probability of undergoing complicated interactions leading to multi-ring events which are not included in our analysis. For muon neutrinos, high energy means in addition that the secondary muon has a good chance of leaving the detector and thus being reconstructed as a PC event. This can be nicely seen from the blue curve in Fig. 5.8 that goes up as the cyan one goes down.

Upward going muons can only be produced by neutrinos with  $E \gtrsim 2$  GeV, because the Super-Kamiokande analysis procedure requires them to have a minimum track length of 7 m in the inner detector. For energies only slightly above this threshold, all upward going muons will stop inside the detector, while for higher energies most of them will leave it again. Therefore the US efficiency ultimately levels out while the UT efficiency increases continually, reflecting the large target volume for high energy neutrinos.

In Fig. 5.8, we also show the angular dependence of the efficiencies: Solid lines are for  $\cos \theta = 0$ , while dashed lines correspond to  $\cos \theta = -1$ . The efficiencies for  $\cos \theta = +1$  are identical to those for  $\cos \theta = -1$  due to the up-down symmetry of the Super-Kamiokande detector, which has the shape of an upright cylinder, slightly stretched along its axes. This geometry also implies that vertical tracks have a higher probability to stop inside the detector, so that the FC efficiencies at several GeV are higher at  $\cos \theta = -1$ , while the PC efficiencies are higher at  $\cos \theta = 0$ . For upward going muons, the target volume is larger in the horizontal direction, so the efficiency for UT events and for low energy US events is higher at  $\cos \theta = 0$ .

For ATLAS, it is difficult to estimate the resolutions and efficiencies because the per-

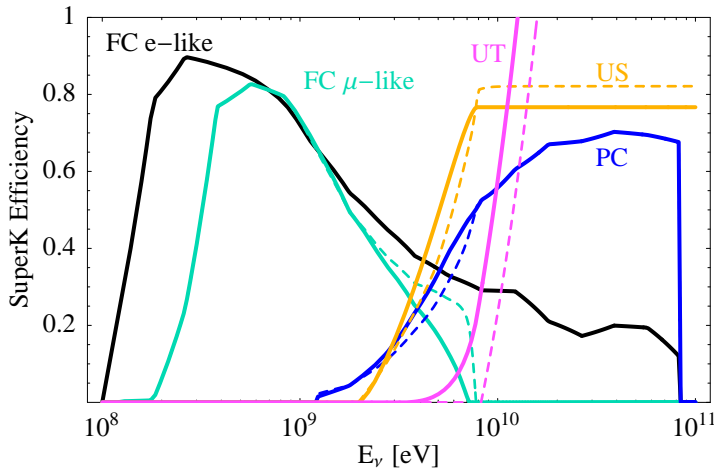


Figure 5.8: Efficiencies of the Super-Kamiokande detector as a function of the neutrino energy. Solid lines correspond to  $\cos\theta = 0$ , dashed lines are for  $\cos\theta = -1$ .

formance of the detector has never been studied under the point of view of neutrino physics before. Most neutrino interactions will take place in the inner parts of the detector, where most of the mass is concentrated. The interaction products will hit the calorimeters, so a reconstruction of the full neutrino energy should be possible. The angular resolution is limited by the fact that a direct track reconstruction is only possible for muons, but not for other particles. Therefore, no directional information will be available for electron neutrinos, and although it might be possible to extract some physical information from their total energy alone, we omit them completely in our analysis of ATLAS. For  $\mu$ -like events, the neutrino direction can be constrained kinematically by combining the information about the muon track and the total  $\nu_\mu$  energy. For quasi-elastic scattering processes (Eq. (5.29)), the kinematics can be reconstructed completely in this way because only two interaction products are involved, and the nucleon participating in the interaction is initially at rest. For single-meson production (Eq. (5.30)) and deep-inelastic scattering (Eq. (5.31)), which are more dominant in the Multi-GeV energy region, it is at least possible to derive constraints on the initial neutrino direction, which are stronger than in Super-Kamiokande, where only the muon is reconstructed.

Based on these considerations, we define three benchmark scenarios:

- In the **conservative scenario**, we assume the energy and angular resolutions to be identical to those of Super-Kamiokande. Furthermore, we assume that only neutrinos with  $E_\nu > 1.5$  GeV can be reconstructed.
- The **realistic scenario** also has a threshold of 1.5 GeV, but a better energy resolution of 5%, an energy-independent angular resolution of  $7^\circ$ , and twice the

exposure of the conservative scenario.

- In the **optimistic scenario**, the energy resolution is 2% and the angular resolution is  $2^\circ$ . In this scenario, we consider events with neutrino energies down to 300 MeV. The exposure is the same as for the realistic scenario. It will probably not be possible to achieve such a good resolution in *ATLAS*, but it is nevertheless interesting to study this scenario because it may be relevant for detectors at future colliders, for example at the ILC.

In all three scenarios, we assume a 100% reconstruction efficiency for FC  $\nu_\mu$  events. We do not distinguish between FC and PC events because the magnetic field allows an energy reconstruction also for muons that leave the detector. For the upward going muon sample, we calculate the efficiencies in analogy to those of *Super-Kamiokande*, but taking into account the different geometry of *ATLAS* (see appendix B). We do not distinguish between US and UT events because only a very small number of muons will stop inside the detector.

### Overall normalization

The overall normalization  $\mathcal{N}$  for *Super-Kamiokande* is chosen such that the total rate of partially contained CC  $\nu_\mu$  events is 1098.8, which corresponds to 1489 days of data taking. We chose the PC sample for the normalization because we have reliable Monte Carlo based efficiencies for this sample, and it is not as strongly affected by backgrounds as the FC sample. With this normalization we obtain 2750 unoscillated FC  $e$ -like events, 4666 FC  $\mu$ -like events, 696 upward stopping muons, and 2194 upward through-going muons. The ratios of the event numbers in the different samples do not exactly match the predictions of the *Super-Kamiokande* Monte Carlo simulations [58], but the discrepancies are well understood and do not have a dramatic effect on our results (see Sec. 5.2.4).

For *ATLAS*,  $\mathcal{N}$  is taken to be 5% of the *Super-Kamiokande* normalization factor in the realistic and optimistic scenarios, and 2.5% of it in the conservative scenario. This accounts for the low exposure and for possibly very stringent cuts that need to be imposed to reject the cosmic muon background. For the realistic scenario, we obtain without oscillations 204 FC  $\mu$ -like events and 229 upward going muons.

### 5.2.3 Analysis of simulated atmospheric neutrino data

To extract physical information from our atmospheric neutrino simulations, we use a  $\chi^2$  analysis similar to the one we used for the reactor experiments discussed in Sec. 5.1.1. Since for Sub-GeV neutrinos we must sample the oscillation probabilities with a smaller step size than for Multi-GeV neutrinos to avoid aliasing effects, we divide the events into a Sub-GeV sample with  $0.3 \text{ GeV} < E_\nu < 1.5 \text{ GeV}$ , and a Multi-GeV sample with  $1.5 \text{ GeV} < E_\nu < 35.0 \text{ GeV}$ . The number of bins we use for the different experiments

	Super-Kamiokande	ATLAS cons.	ATLAS real.	ATLAS opt.
Sub-GeV FC				
log $E$	10	—	—	30
cos $\theta$	10	—	—	40
Multi-GeV FC				
log $E$	20	20	30	60
cos $\theta$	10	10	10	40
PC (cos $\theta$ )	10	—	—	—
US (cos $\theta$ )	15	—	—	—
UT (cos $\theta$ )	30	27	27	27

Table 5.4: Binning for the analysis of the simulated data for different experiments.

are shown in table 5.4. The bin widths are roughly based on the resolutions given in table 5.3. As discussed above, we do not use  $e$ -like events in ATLAS, but as ATLAS can do charge identification, we use separate bins for  $\nu_\mu$  and  $\bar{\nu}_\mu$ . For the ATLAS UT sample, we only consider events with  $-1.0 < \cos \theta < -0.1$  to reject the possibly large backgrounds in the horizontal directions, while for Super-Kamiokande we use the whole range  $-1.0 < \cos \theta < 0$ . Although our choice of bins for ATLAS is not suitable for the analysis of real experimental data, because the bins are so small that most of them will contain one event at most, this binning gives a good estimate of the information that is contained in the data sample. To extract this information in reality, an optimized binning or a likelihood analysis would have to be used.

The  $\chi^2$  function for Super-Kamiokande is composed of contributions from the different event samples and of pull terms for external input on the oscillation parameters and on the systematical uncertainties:

$$\chi^2 = \chi_{FCe}^2 + \chi_{FC\mu}^2 + \chi_{PC}^2 + \chi_{US}^2 + \chi_{UT}^2 + \chi_{\text{pull,osc}}^2 + \chi_{\text{pull,sys}}^2. \quad (5.34)$$

For ATLAS, only FC  $\mu$ -like events and UT events contribute, but there are separate terms for neutrinos and antineutrinos. We assume the events to be distributed according to the Poisson Distribution, so the subexpression for event sample  $A$  is given by

$$\chi_A^2 = \sum_{i,j} 2[N_{ij,A}(\Theta_{\text{true}}) - T_{ij,A}(\Theta_{\text{test}}, \mathbf{a})] + 2T_{ij,A}(\Theta_{\text{test}}, \mathbf{a}) \log \left( \frac{T_{ij,A}(\Theta_{\text{test}}, \mathbf{a})}{N_{ij,A}(\Theta_{\text{true}})} \right), \quad (5.35)$$

where  $N_{ij,A}(\Theta_{\text{true}})$  is the “observed” event rate in bin  $(i, j)$  for the “true” oscillation parameters  $\Theta_{\text{true}} = (\theta_{12}, \theta_{13}, \theta_{23}, \delta_{CP}, \Delta m_{21}^2, \Delta m_{31}^2)^T$ , and  $T_{ij,A}(\Theta_{\text{test}}, \mathbf{a})$  is the event rate that would be expected for the hypothesized parameters  $\Theta_{\text{test}}$ , and for biases  $\mathbf{a}$  arising from systematical errors in the experiment. For PC, US, and UT events, the

summation over energy bins  $i$  is omitted, and only the sum over zenith angle bins  $j$  remains.

The pull term for the oscillation parameters has the form

$$\chi_{\text{pull,osc}}^2 = \sum_k \frac{(\Theta_{k,\text{test}} - \Theta_{k,\text{true}})^2}{\sigma_{\Theta_k}^2}, \quad (5.36)$$

where the summation runs only over those parameters for which external input is to be taken into account.  $\sigma_{\Theta_k}$  determines how strongly a fit value far from the externally given one is disfavoured. Pull terms are specified primarily for parameters to which the experiment under consideration has no sensitivity. This prevents the numerical fitting algorithm from evolving these parameters too far from the values obtained by other experiments in its attempt to get a better fit to the data, thus spoiling the sensitivity to the parameters that we are actually interested in.

Pull terms for systematical biases are similar to those for the oscillation parameters:

$$\chi_{\text{pull,sys}}^2 = \sum_k \frac{a_k^2}{\sigma_{a_k}^2}. \quad (5.37)$$

They give a penalty to fit values  $a_k$  which are further from zero than can be expected from the systematical uncertainties  $\sigma_{a_k}$ . We have defined  $\mathbf{a}$  such that the case of vanishing systematical errors corresponds to  $\mathbf{a} = 0$ .

To obtain the sensitivity of the experiment to some oscillation parameter  $\Theta_i$ , we keep this parameter fixed at some specific test value  $\Theta_{i,\text{test}}$ , and minimize  $\chi^2$  over the remaining oscillation parameters and over  $\mathbf{a}$ . By repeating this for different values of  $\Theta_{i,\text{test}}$ , we can find out which values of  $\Theta_i$  can be excluded at a given confidence level.

In the pull term  $\chi_{\text{pull,osc}}^2$  we assume  $\sigma_{\theta_{12}}$  and  $\sigma_{\theta_{23}}$  to be 10%, while we take 5% for  $\sigma_{\Delta m_{21}^2}$  and 30% for  $\sigma_{\Delta m_{31}^2}$ , in agreement with the current bounds from chapter 3. We assume the CHOOZ bound of  $10^\circ$  for  $\theta_{13}$ , and no external knowledge on  $\delta_{CP}$ . Of course, we only introduce pull terms for those parameters which we are not currently fitting.

The types and magnitudes of the systematical errors for the different experiments are listed in tab. 5.5. Normalization errors are implemented in the same way as for reactor experiments (cf. Eq. (5.1)). They are taken to be very large to account for the uncertainties in the initial fluxes and in the cross sections. The ‘‘tilt’’ errors are a simple way to introduce energy or angle dependent biases. For example, an energy tilt  $a_{E\text{-tilt}}$  enhances the event rates by a term growing with the energy according to

$$T_{ij}(a_{E\text{-tilt}}, \dots) = \left(1 + a_{E\text{-tilt}} \frac{i}{i_{\text{max}}}\right) T_{ij}(a_{E\text{-tilt}} = 0, \dots). \quad (5.38)$$

As the energy binning in INSANE is logarithmically, this growth is logarithmically as well. Of course, the expression in Eq. (5.38) is only meaningful in combination with a

sufficiently large normalization error because otherwise it could only describe an excess or deficit in the high energy region but not for low energies. The zenith angle tilts are implemented in a similar way:

$$T_{ij}(a_{\theta\text{-tilt}}, \dots) = \left(1 + a_{\theta\text{-tilt}} \frac{j}{j_{\text{max}}}\right) T_{ij}(a_{\theta\text{-tilt}} = 0, \dots). \quad (5.39)$$

In Super-Kamiokande, several background sources add to the total event rate [58]. The FC Sub-GeV samples and the Multi-GeV FC  $e$ -like sample contain between 5% and 10% of neutral current background events. We neglect this background because we assume that it can in principle be subtracted with a reasonable accuracy. The number of NC events depends only on the initial neutrino flux, i.e. if the initial flux is known to within 20%, the background subtraction error is at most 2%. Besides the NC background, there is a probability of several percent for muon neutrinos to be misidentified as  $\nu_e$ . We assume the misidentification probability to be 5% for all energies.

In ATLAS, it should also be possible to subtract NC backgrounds, but cosmic muons might be a problem in the downward and horizontal directions because of the lower overburden. To account for this, we allow a larger zenith angle tilt for FC events in ATLAS, and for upward going muons, we consider only events with  $-1.0 < \cos \theta < -0.1$ , as discussed above.

#### 5.2.4 Event distributions in Super-Kamiokande and ATLAS

Before making predictions about the physics potential of Super-Kamiokande and ATLAS, we will first consider the low level event rate distributions. In Fig. 5.9, we show the zenith angle distributions for Super-Kamiokande as predicted by INSANE, both with and without inclusion of neutrino oscillations, and compare them with the published Super-Kamiokande data and Monte Carlo results [58]. For this plot we have used separate Monte Carlo based efficiencies  $\epsilon^E$  for Sub-GeV and Multi-GeV FC events instead of the combined curves plotted in Fig. 5.8. This ensures that we get the separation of Sub-GeV and Multi-GeV events right.

Nevertheless, our predictions for the fully contained event rates are significantly too low, although the zenith angle spectra agree well with those from Super-Kamiokande. The reason for the deficit is that we have assumed maximal solar activity and thus minimal neutrino flux, while Super-Kamiokande data was taken mostly at solar minimum, corresponding to maximal neutrino flux. Since only low energy cosmic rays are affected by the solar wind, the mismatch is larger for the Sub-GeV samples. For  $e$ -like events, it is furthermore enhanced by a 10% admixture of neutral current background events, which we neglected for the reasons discussed above.

For PC events, the agreement between our simulations and the Super-Kamiokande results is excellent because we have normalized INSANE to the total rate of unoscillated CC  $\nu_\mu$  PC events in Super-Kamiokande. Amazingly, the agreement is also very good for

## Super-Kamiokande

	<b>Error Type</b>	<b>Magnitude</b>
1	Overall normalization for FC events	20%
2	Relative normalization for FC $\nu_e$ events	5%
3	Relative normalization for antineutrinos	5%
4	Relative normalization for Multi-GeV events	10%
5	Normalization for PC events	20%
6	Normalization for US events	20%
7	Normalization for UT events	20%
8	Tilt of the energy spectrum for FC Sub-GeV events	5%
9	Tilt of the energy spectrum for FC Multi-GeV events	5%
10	Tilt of the zenith angle spectrum for FC Sub-GeV events	2%
11	Tilt of the zenith angle spectrum for FC Multi-GeV events	2%
12	Tilt of the zenith angle spectrum for PC events	2%
13	Tilt of the zenith angle spectrum for US events	2%
14	Tilt of the zenith angle spectrum for UT events	2%

## ATLAS

	<b>Error Type</b>	<b>Magnitude</b>
1	Overall normalization for contained events	20%
2	Relative normalization for antineutrinos	5%
3	Normalization for upward going muon events	20%
4	Tilt of the energy spectrum	5%
5	Tilt of the zenith angle spectrum for contained events	10%
6	Tilt of the zenith angle spectrum for upward going muon events	2%

Table 5.5: Systematical errors in Super-Kamiokande and ATLAS.

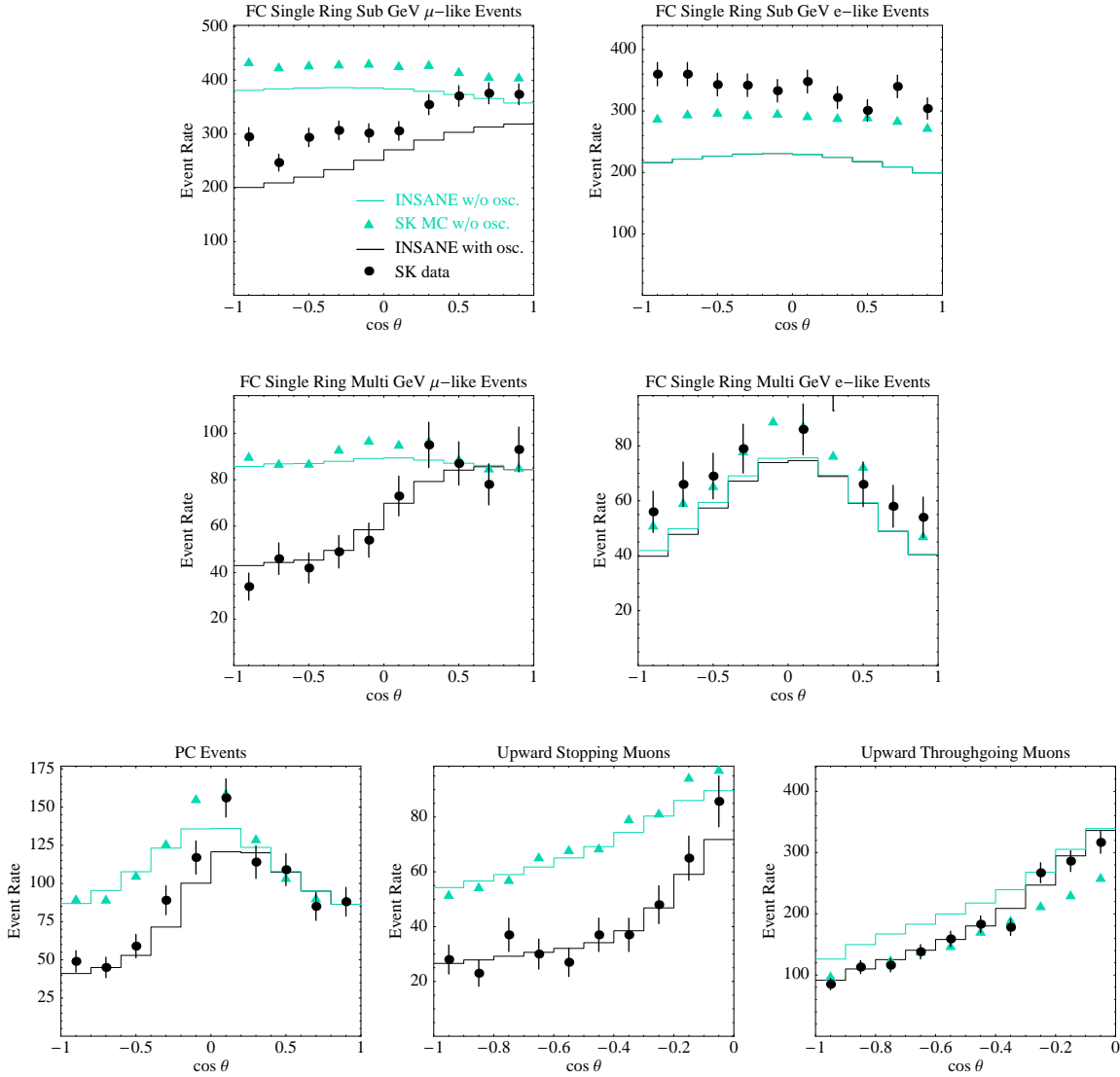


Figure 5.9: Comparison of the event rates predicted by INSANE to the Super-Kamiokande data and Monte Carlo results [58]. We have normalized our simulation to the total rate of CC partially contained  $\nu_\mu$  events without oscillations from the MC simulation. The normalization of the other event samples is determined by INSANE. The resulting discrepancies are explained in the text.

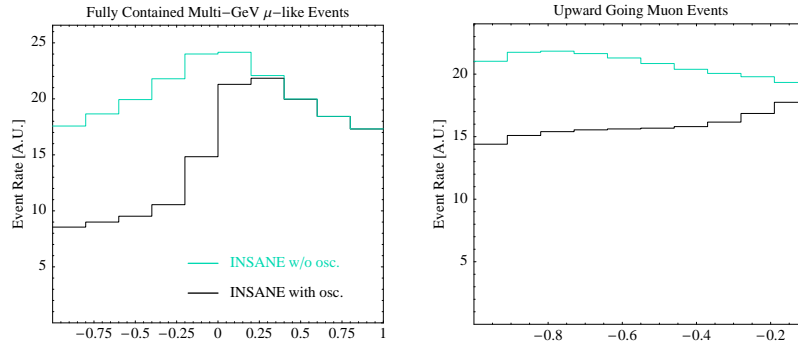


Figure 5.10: Zenith angle distribution of the expected event rates in ATLAS.

upward stopping muons although we have calculated the efficiencies for these without any input from detector Monte Carlo simulations. For upward through-going muons, the agreement with the data is also excellent, but for the prediction without oscillations, we obtain more events than Super-Kamiokande. This might be attributed to our possibly imperfect estimates of the upward going muon efficiencies, but we would like to remark that also the Monte Carlo simulation seems to have some problems here, because it predicts fewer events without oscillations than have actually been seen in the experiment with oscillations.

Besides the comparison of the zenith angle distributions, we have also checked that the energy distributions predicted by INSANE agree with those from the Super-Kamiokande Monte Carlo simulation. A comparison with experimental results was not possible, because for FC events, the energy binning of Super-Kamiokande is too rough, and for PC, US, and UT events, the neutrino energy cannot be reconstructed.

We have also checked that the event rates for FC  $\mu$ -like and upward through-going muon events in ATLAS have the expected shapes (Fig. 5.10). Since ATLAS does not distinguish between fully contained and partially contained events, the FC  $\mu$ -like rate in the left panel of Fig. 5.10 has to be compared to the sum of the FC  $\nu_\mu$  and PC events in Super-Kamiokande, and we find excellent agreement for the simulation without oscillations. With oscillations, the decrease in the event rate at  $\cos\theta = 0$  is sharper in ATLAS than in Super-Kamiokande because there is less washout due to the better angular resolution.

The zenith angle distribution of upward going muon events in ATLAS is relatively flat compared to that of Super-Kamiokande because the geometry of ATLAS is such that the target area for vertical muon tracks is larger than for horizontal tracks, so that the lower initial flux in the vertical direction is compensated.

### 5.2.5 Physics potential of atmospheric neutrino experiments

In this section we will present our main results on the physics potential of atmospheric neutrino oscillation experiments, focusing in particular on ATLAS.

#### Measurement of $\theta_{23}$ and $\Delta m_{31}^2$

First, we compare the predicted confidence regions in the  $\theta_{23}$ - $\Delta m_{31}^2$  plane with fits by the Super-Kamiokande collaboration to check the assumptions and simplifications we made in the INSANE analysis. This comparison is shown in Fig. 5.11. The right panel contains two different Super-Kamiokande fits: For the zenith angle fit, the events were binned over  $\cos\theta$  as in Fig. 5.9, while for the  $L/E$  analysis, they were sorted according to the baseline-to-energy ratio  $L/E$ . Both fits are based on a two-flavour model, so the degeneracies  $\Delta m_{31}^2$  vs.  $-\Delta m_{31}^2$  and  $\theta_{23}$  vs.  $\pi/2 - \theta_{23}$  have no impact on it. The three-flavour treatment of INSANE can distinguish these degeneracies, but to make the results comparable, we show in the left plot only the minimum of the four resulting  $\chi^2$  values.

The comparison of the plots reveals that the confidence regions obtained with INSANE are very similar to those obtained by Super-Kamiokande. The  $\theta_{23}$  sensitivity is approximately the same as in the  $L/E$  analysis, but not as good as in the zenith angle analysis, because we could not include the information from multi-ring events and thus have lower overall statistics. This is also one of the reasons why the  $\Delta m_{31}^2$  sensitivity predicted by INSANE is in agreement only with the more conservative zenith angle analysis, although our two-dimensional binning should in principle also contain the  $L/E$  information. Other reasons are that in the  $L/E$  analysis, Super-Kamiokande uses a larger fiducial volume and exploits outer detector information for PC events.

To discuss the prospects of ATLAS to detect neutrino oscillations, we compare in Fig. 5.12 the  $\theta_{23}$ - $\Delta m_{31}^2$  confidence regions of the “realistic” ATLAS scenario, of Super-Kamiokande, and of the superbeam experiment T2K. Note that the confidence levels are now  $1\sigma$ ,  $2\sigma$  and  $3\sigma$  instead of 68%, 90%, and 99% as in Fig. 5.11 to make the results more comparable with the literature on future accelerator experiments.

The plot shows that the  $\theta_{23}$  sensitivity of ATLAS is relatively poor due to the low statistics, so that the  $3\sigma$  confidence interval reaches from  $20^\circ$  to  $70^\circ$ . Nevertheless, the experiment can rule out the no oscillation hypothesis and thus provide an independent confirmation of neutrino oscillations with a detector technology which is completely new in this field of particle physics. The  $\Delta m_{31}^2$  sensitivity of ATLAS is slightly better than that of Super-Kamiokande at the  $1\sigma$  level, but at higher confidence levels, very large values of  $\Delta m_{31}^2$  cannot be ruled out. Neither of the atmospheric experiments can compete with T2K, which achieves the best sensitivity to both parameters.

Note that we have used the CHOOZ bound  $\theta_{13} < 10^\circ$  as external input according to Sec. 5.2.3. Without this constraint, the contours would extend to larger  $\Delta m_{31}^2$  in

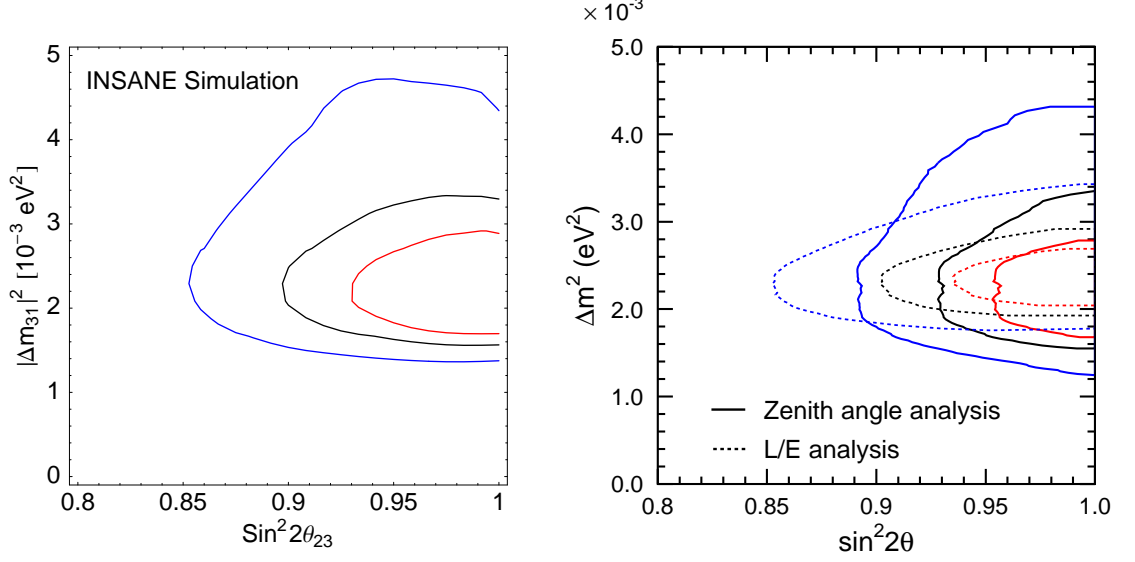


Figure 5.11: Left panel: Confidence regions in the  $\theta_{23}$ - $\Delta m_{31}^2$ -plane for Super-Kamiokande, obtained with INSANE. Right panel: Results of two-flavour fits published by the Super-Kamiokande collaboration [14, 58]. The contours correspond to confidence levels of 68%, 90%, and 99%.

the region where  $\theta_{23} < \pi/4$ , because the appearance of oscillations at relatively short baselines and high energies, which would normally rule out too large values of  $\Delta m_{31}^2$ , can for large  $\theta_{13}$  be partly compensated by matter effects in the  $\nu_\mu \rightarrow \nu_\tau$  channel, which can shift the first maximum back to lower energies and longer baselines. This is only possible for  $\theta_{23} < \pi/4$ , because otherwise,  $\nu_\mu \rightarrow \nu_e$  oscillations driven by  $\theta_{13}$ , which are proportional to  $\sin^2 \theta_{23}$  (cf. Eq. (4.9)) would spoil the fit.

The confidence regions in Fig. 5.12 for the assumption of an inverted mass hierarchy look very similar to those for the normal hierarchy, i.e. neither of the experiments can resolve the  $\Delta m_{31}^2$  degeneracy. This is still the case if we assume a non-zero true value for  $\theta_{13}$ . Furthermore, since we have assumed the true  $\theta_{23}$  to be exactly  $\pi/4$ , the plot is symmetric about this value, i.e. the so-called octant degeneracy  $\theta_{23}$  vs.  $\pi/2 - \theta_{23}$  is not relevant.

In Fig. 5.13 we compare the  $\theta_{23}$ - $\Delta m_{31}^2$  confidence regions for the three different ATLAS scenarios. The shaded regions for the realistic scenario are the same as in Fig. 5.12, but as we now show a larger range of  $\Delta m_{31}^2$  values, two degenerate solutions become visible at  $\Delta m_{31}^2 \approx \pm 6.6 \cdot 10^{-3} \text{ eV}^2$ . For these test values, the oscillation length is just a factor

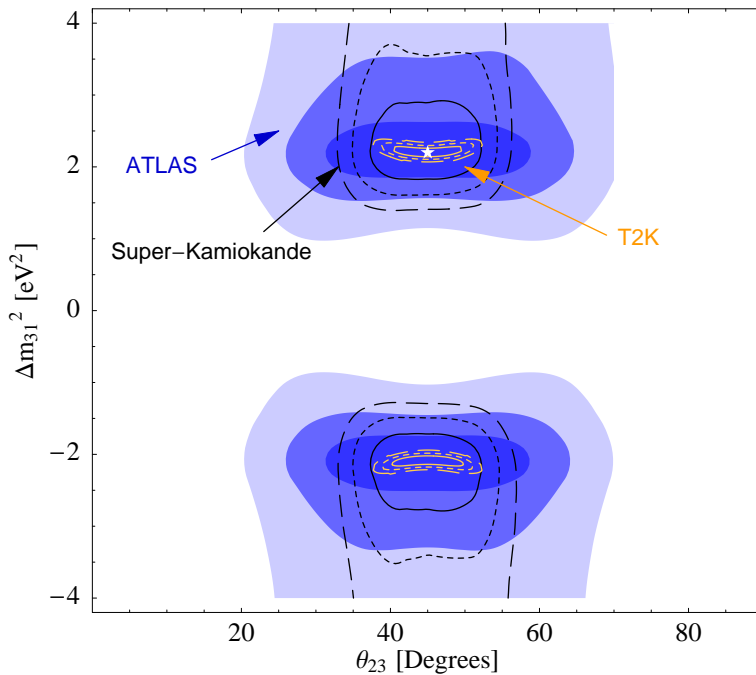


Figure 5.12: Confidence regions in the  $\theta_{23}$ - $\Delta m_{31}^2$ -plane for Super-Kamiokande (black contours), ATLAS (shaded regions) T2K (orange contours). The solid, dotted and dashed lines correspond to the  $1\sigma$ ,  $2\sigma$ , and  $3\sigma$  confidence levels for two degrees of freedom, the white star indicates the assumed true values of the parameters. The T2K contours are taken from [69,70].

of three smaller than for the “true” value  $\Delta m_{31}^2 = 2.2 \cdot 10^{-3} \text{ eV}^2$ , so that the second oscillation maximum takes the place of the first one. Since this degeneracy is already ruled out by existing data, it does not pose a problem.

The sensitivity to  $\Delta m_{31}^2$  of the optimistic scenario is much better than that of the realistic scenario because of the higher resolution. The  $\theta_{23}$  measurement is however still limited by low statistics. The conservative scenario finally has only very poor sensitivity, and is not even able to rule out the hypothesis of no oscillations at the  $3\sigma$  level. This shows that the results of ATLAS will depend crucially on the resolutions and event rates that can finally be reached.

### Sensitivity to $\sin^2 2\theta_{13}$

We will now consider the potential of future atmospheric neutrino experiments to detect three-flavour effects. In Fig. 5.14 we show the sensitivity (defined as in secs. 5.1.1 and 3.3) of a Super-Kamiokande-like detector to the small mixing angle  $\theta_{13}$ . The lower

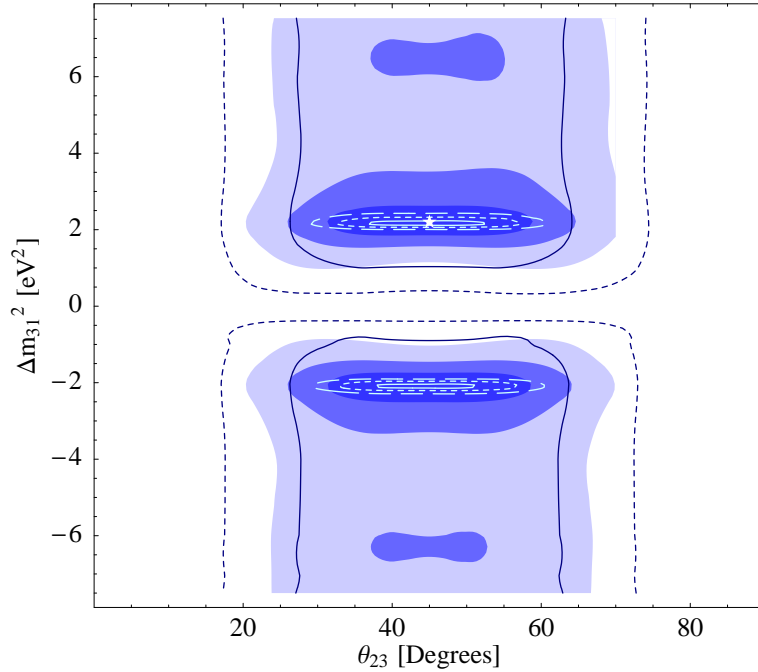


Figure 5.13: Confidence regions in the  $\theta_{23}$ - $\Delta m_{31}^2$ -plane for the three ATLAS scenarios. Dark blue contours are for the conservative, shaded regions for the realistic, and light blue contours for the optimistic scenario. The confidence levels  $1\sigma$ ,  $2\sigma$ , and  $3\sigma$  are shown, and the white star indicates the assumed true values of the parameters. Note that for the conservative scenario, the  $3\sigma$  contour is absent because it cannot rule out the no-oscillation hypothesis at this confidence level.

edge of the filled region corresponds to the purely statistical limit, while the blue, green, and yellow bands show the impact of systematical uncertainties, parameter correlations, and the  $\text{sign}(\Delta m_{31}^2)$  degeneracy. The vertical grey lines indicate the exposure that has been achieved in Super-Kamiokande, and the exposure that can be expected in Hyper-Kamiokande, a megaton water Čerenkov detector similar to Super-Kamiokande, which we simulate by simply multiplying the normalization factor  $\mathcal{N}$  of Super-Kamiokande by 20.

The plot shows that with only statistical limitations, even Super-Kamiokande could provide a slight improvement of the current CHOOZ bound on  $\sin^2 2\theta_{13}$ . The impact of systematical uncertainties is relatively small, but parameter correlations are a severe limitation. They can only be overcome when more accurate information on the other oscillation parameters, in particular on  $\theta_{23}$ ,  $\Delta m_{31}^2$ , and  $\delta_{CP}$ , will become available. However, this information can only come from new accelerator experiments, which have

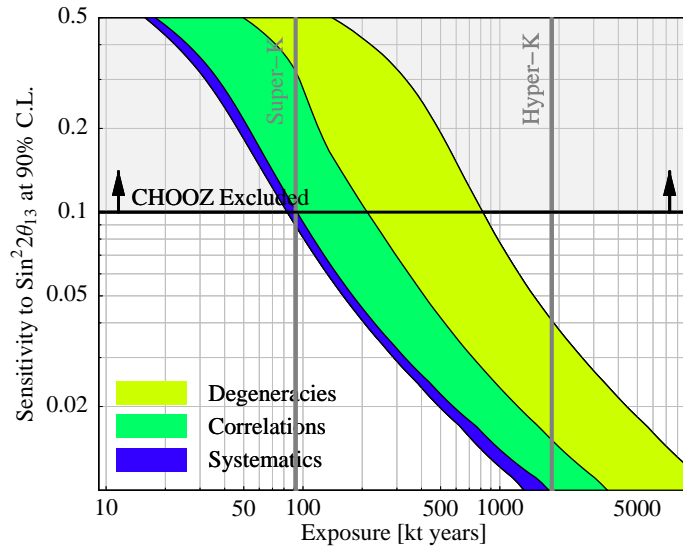


Figure 5.14:  $\sin^2 2\theta_{13}$  sensitivity of Super-Kamiokande at the 90% C.L. as a function of the exposure. The shaded regions indicate the limitations due to systematical errors, parameter correlations, and degeneracies.

themselves an excellent sensitivity to  $\theta_{13}$ , and would therefore render a measurement with atmospheric neutrinos unnecessary. Even more dramatic than the limitations due to parameter correlations is the impact of the  $\text{sign}(\Delta m_{31}^2)$  degeneracy. This is easy to understand because the main source of  $\theta_{13}$  sensitivity in Super-Kamiokande is the atmospheric matter resonance at very long baselines. For the “true” value  $\theta_{13} = 0$ , this resonance is absent, but for non-vanishing test values, the event rates at several GeV will get modified. These modifications are much weaker if an inverted mass hierarchy is assumed, because then the resonance is shifted to the antineutrino sector, where the cross sections are lower. Therefore, only very large  $\theta_{13}$  can be ruled out in this case. The  $\text{sign}(\Delta m_{31}^2)$  degeneracy might be resolved if a nearby supernova occurs, and Earth matter effects are detected in its neutrino signal (see chapter 3). Figure 5.14 is in accordance with the results of a recent three-flavour fit by the Super-Kamiokande collaboration [71], which confirms their limited sensitivity to  $\theta_{13}$ .

To see how the different event samples contribute to the overall sensitivity, we show in Fig. 5.15 the  $\chi^2$  function for Hyper-Kamiokande over the test value for  $\theta_{13}$ . The true value was assumed to be zero, therefore the curves start out at zero at the left edge of the plot. Obviously, the best sensitivity comes from fully contained  $e$ -like events, because in this channel, the atmospheric resonance is most easily detectable as a strong electron appearance signal at several GeV and long baselines. The other samples do not contribute significantly. For very large  $\theta_{13}$ , the curve for the FC  $e$ -like sample has

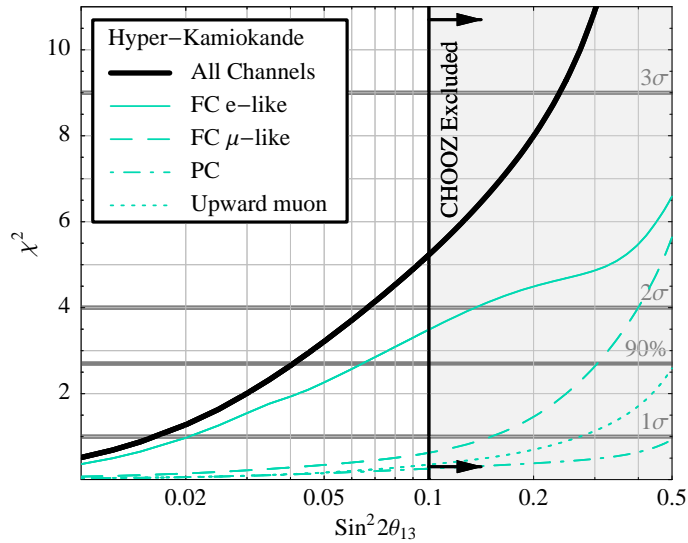


Figure 5.15:  $\chi^2$  function for the Hyper-Kamiokande experiment. The colored curves show the contributions from the individual data samples.

an interesting plateau, the origin of which is again found in the atmospheric resonance: For small test values of  $\theta_{13}$ , the first oscillation maximum at the resonance energy is at a baseline larger than the diameter of the Earth. As  $\theta_{13}$  increases, the maximum approaches  $2R_{\text{Earth}}$ , and the resonant enhancement becomes stronger, so that the predicted event rates no longer provide a good fit to the “true” rates with  $\theta_{13} = 0$ . For very large test values, the first oscillation maximum is inside the Earth, and as the next minimum approaches, the overall enhancement will *decrease* from some point on, so the fit becomes again better. The availability of spectral information, in combination with the complicated oscillation patterns in the PREM profile, partly resolves the problem, so that  $\chi^2$  only flattens out instead of actually decreasing. We have checked that with the assumption of constant matter density throughout the Earth, a real local minimum appears at precisely the point where the Earth diameter is equal to one full oscillation length at the resonance energy.

In Fig. 5.16, we compare the sensitivity to  $\theta_{13}$  of atmospheric neutrino experiments to that of the reactor experiments Double Chooz and Triple Chooz, and of the accelerator setups MINOS, NO $\nu$ A, and T2K. The colour coding is the same as in Fig. 5.14, and the bars for Super-Kamiokande and Hyper-Kamiokande are actually a simple vertical cut through this plot. As we have seen before, atmospheric neutrino experiments can only rule out very large  $\theta_{13}$  because they are limited by correlations and degeneracies. Even with the good statistics in Hyper-Kamiokande, a sensitivity beyond  $\sin^2 2\theta_{13} = 0.04$  cannot be expected. ATLAS is limited by statistics and degeneracies, and is therefore

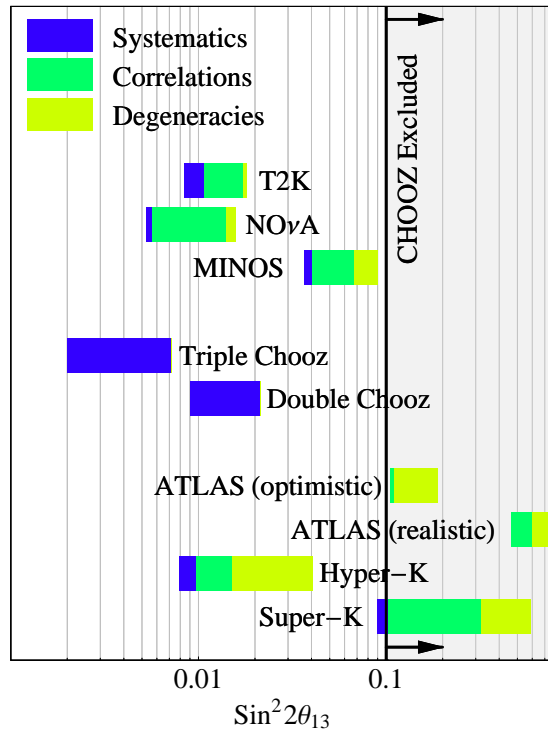


Figure 5.16: Limitations of the sensitivity to  $\theta_{13}$  due to statistics, systematics, correlations, and degeneracies for the atmospheric neutrino experiments **Super-Kamiokande**, **Hyper-Kamiokande**, and **ATLAS**, for the accelerator experiments **MINOS**, **NO $\nu$ A**, and **T2K** [69, 70], and for the reactor setups **Double Chooz** and **Triple Chooz**.

unable to search for  $\theta_{13}$ .

The beam experiments suffer mainly from correlations, especially between  $\theta_{13}$  and  $\delta_{CP}$ . **MINOS**, which is currently running, has a sensitivity only slightly below the **CHOOZ** bound, but the future projects **NO $\nu$ A** and **T2K** can improve this down to  $\sin^2 2\theta_{13} \lesssim 0.02$ , well beyond the sensitivity of atmospheric neutrinos. **Double Chooz** is only slightly worse than **T2K** and **NO $\nu$ A**, and provides a very clean measurement, which is only affected by systematical uncertainties. **Triple Chooz** finally has by far the best sensitivity of all experiments shown here, and could only be rivaled by an upgraded superbeam like **T2HK**, a beta beam or a neutrino factory (see refs. [39, 72]).



# Chapter 6

## Summary and conclusions

In this work, we have discussed three-flavour neutrino oscillations from a phenomenological point of view. We have introduced the quantum mechanical formalism of neutrino oscillations in chapter 2, and derived the two-flavour oscillation probability in two different ways. We have discussed the caveats of the usual textbook derivation, in particular the equal momentum approximation, and we have shown why this derivation nevertheless gives the correct result. We have then extended the formalism to the realistic three-neutrino system, incorporated matter effects, and stated several interesting properties of the oscillation probabilities.

We have given an overview of the current status of neutrino oscillation physics in chapter 3, and discussed the most important open questions, in particular the search for generic three-flavour effects such as non-vanishing  $\theta_{13}$ , leptonic CP violation, and the neutrino mass hierarchy.

In the analytical discussion of three flavour effects in chapter 4, we have considered the  $\nu_e \rightarrow \nu_e$  channel, the  $\nu_\mu \rightarrow \nu_e$  channel, and the  $\nu_\mu \rightarrow \nu_\tau$  channel. The  $\nu_e \rightarrow \nu_e$  channel is important for reactor neutrino experiments searching for the weak  $\theta_{13}$ -oscillations that are superimposed on the dominant solar term.

The  $\nu_\mu \rightarrow \nu_e$  channel is interesting especially for future accelerator experiments. For low energies, the solar oscillations dominate, with only weak perturbations proportional to  $\sin 2\theta_{13}$ . Above the solar MSW resonance at around 100 MeV, the solar terms get suppressed, but if  $\theta_{13}$  is not too small, the transition probability can again be enhanced at the atmospheric resonance, which is located at several GeV. For large  $\theta_{13}$ , it will also be possible to discover leptonic CP violation around the first atmospheric maximum. It is however difficult to disentangle the correlations between the oscillation parameters there. If the matter density is not constant, but instead follows the PREM profile of the Earth, the oscillatory behaviour is significantly modified, in particular at the atmospheric resonance for very large baselines. To calculate these modifications, which may be relevant to atmospheric neutrinos and to accelerator projects in the distant future, the PREM profile can be approximated by a three-layer model.

Oscillations in the  $\nu_\mu \rightarrow \nu_\tau$  channel are dominated by the close-to-maximal  $\theta_{23}$  term, but for low energies, also solar oscillations are very strong. The atmospheric resonance affects the  $\nu_\mu \rightarrow \nu_\tau$  channel, but it will be very challenging to detect this effect experi-

mentally.

In the first part of chapter 5, we have considered the potential of future reactor experiments to measure  $\theta_{13}$ . The main limitation for such a measurement are systematical errors, which have to be carefully incorporated into the  $\chi^2$  analysis. For exposures which are large enough to keep the statistical uncertainty on the total number of events small, the systematical normalization errors are crucial, and need to be reduced e.g. by the construction of a dedicated near detector. If the event rates are so large that spectral information can be used, only uncorrelated bin-to-bin errors can spoil the performance. Two particularly interesting reactor projects are **Double Chooz**, which can push the limit on  $\sin^2 2\theta_{13}$  down to 0.02, and its possible upgrade **Triple Chooz** with a sensitivity below 0.01.

Another interesting neutrino source are cosmic rays interacting with the atmosphere of the Earth. It is unfortunately very difficult to see three-flavour effects in these atmospheric neutrinos because of the numerical coincidence of the flux ratio and the mixing angle,  $\Phi(\nu_e)/\Phi(\nu_\mu) \approx \sin^2 \theta_{23} \approx 0.5$ , in combination with the limited experimental resolution. We have developed **INSANE**, a sophisticated software program for the simulation of present and future atmospheric neutrino experiments. We have incorporated realistic fluxes and cross sections, a full three-flavour treatment of the oscillation probabilities, and an abstract description of the detector properties. To analyze the simulated event rates, we have used a  $\chi^2$  analysis, taking into account statistical and systematical uncertainties as well as parameter correlations and degeneracies. We have verified the realism of **INSANE** by comparison with the results of **Super-Kamiokande**.

We have proposed to study atmospheric neutrinos with the **ATLAS** detector at CERN. We have made assumptions on the detector resolutions and efficiencies, and based on these assumptions, we have predicted that **ATLAS** could confirm neutrino oscillations at better than  $3\sigma$ , and furthermore measure  $\Delta m_{31}^2$  and  $\theta_{23}$  with an accuracy that is however worse than the existing bounds from **Super-Kamiokande**. We have emphasised that the potential of **ATLAS** depends crucially on the energy and angular resolutions that can be reached. We have also studied the potential of atmospheric neutrino experiments to detect three-flavour effects, but have found that such a measurement could never compete with dedicated accelerator experiments.

# Appendix A

## Numerical calculation of oscillation probabilities

When fitting neutrino oscillation parameters to a simulated or real data set, it is necessary to calculate the oscillation probabilities at many different points in the parameter space. This is only possible if one can rely on fast and stable numerical algorithms.

### A.1 Constant matter density

As long as the matter density is constant, the most efficient ansatz is to diagonalize the Hamiltonian of Eq. (2.46) to obtain the effective mixing parameters in matter, and then to insert these into Eq. (2.16).

The easiest way to perform the diagonalization is by using a “black box” eigensystem routine, as it is for example provided by the GNU Scientific Library [73] or the Linear Algebra Package LAPACK [74]. The disadvantage of these packages is that they are optimized for very large matrices with at least several thousand rows and columns, and produce a substantial computational overhead when applied to the  $3 \times 3$  neutrino Hamiltonian.

Therefore we have developed a specialized algorithm for calculating the eigensystem of  $3 \times 3$  complex Hermitian matrices. The basic idea behind it is that in 3-dimensional space, the vector cross product is available, which is a very powerful tool for problems involving orthogonal vectors.

Let  $\mathbf{A}$  be any complex Hermitian  $3 \times 3$  matrix with (real) eigenvalues  $\lambda_i$  and corresponding eigenvectors  $\mathbf{v}_i$ , where  $i = 1, 2, 3$ . We assume for the moment that  $\lambda_1$  is known. Then,  $\mathbf{v}_1$  fulfills the equation

$$(\mathbf{A} - \lambda_1 \mathbf{I})\mathbf{v}_1 = 0, \tag{A.1}$$

where  $\mathbf{I}$  is the  $3 \times 3$  identity matrix. We take the Hermitian conjugate of this equation and multiply it with an arbitrary vector  $\mathbf{x} \in \mathbb{R}^3$  to obtain

$$\mathbf{v}_1^\dagger (\mathbf{A} - \lambda_1 \mathbf{I})\mathbf{x} = 0, \tag{A.2}$$

i.e.  $\mathbf{v}_1$  is orthogonal to the image of  $\mathbf{A} - \lambda_1 \mathbf{I}$  and can be calculated as the cross product of two linearly independent elements of this image (provided of course, that  $\mathbf{A} - \lambda_1 \mathbf{I}$  is not of rank 1). As soon as  $\lambda_1$  and  $\mathbf{v}_1$  are known, the 1-dimensional subspace generated by  $\mathbf{v}_1$  can be split off and the remaining 2-dimensional problem can be solved exactly. We perform the splitting off by means of a complex Householder transformation

$$\mathbf{P} = \mathbf{I} - \omega \mathbf{u} \mathbf{u}^\dagger \quad (\text{A.3})$$

with

$$\mathbf{u} = \mathbf{v}_1 \mp |\mathbf{v}_1| \mathbf{e}_1 \quad (\text{A.4})$$

and

$$\omega = \frac{1}{|\mathbf{u}|^2} \left( 1 + \frac{\mathbf{v}_1^\dagger \mathbf{u}}{\mathbf{u}^\dagger \mathbf{v}_1} \right). \quad (\text{A.5})$$

In Eq. (A.4),  $\mathbf{e}_1$  denotes the first unit vector  $(1, 0, 0)^T$ . From a purely mathematical point of view, the choice of sign in this equation is arbitrary, but in the actual implementation we choose it to be equal to the sign of the real part of  $v_{11}$  to avoid roundoff errors in this step. It is straightforward to show that  $\mathbf{P}$  is unitary:

$$\mathbf{P}^\dagger \mathbf{P} = (\mathbf{I} - \omega \mathbf{u} \mathbf{u}^\dagger) (\mathbf{I} - \omega^* \mathbf{u} \mathbf{u}^\dagger) \quad (\text{A.6})$$

$$= \mathbf{I} - \frac{\mathbf{u} \mathbf{u}^\dagger}{|\mathbf{u}|^2} \left( 2 + \frac{\mathbf{v}_1^\dagger \mathbf{u}}{\mathbf{u}^\dagger \mathbf{v}_1} + \frac{\mathbf{u}^\dagger \mathbf{v}_1}{\mathbf{v}_1^\dagger \mathbf{u}} \right) + \frac{\mathbf{u} \mathbf{u}^\dagger \mathbf{u} \mathbf{u}^\dagger}{|\mathbf{u}|^2} \left( 2 + \frac{\mathbf{v}_1^\dagger \mathbf{u}}{\mathbf{u}^\dagger \mathbf{v}_1} + \frac{\mathbf{u}^\dagger \mathbf{v}_1}{\mathbf{v}_1^\dagger \mathbf{u}} \right) \quad (\text{A.7})$$

$$= \mathbf{I}. \quad (\text{A.8})$$

Furthermore,  $\mathbf{P} \mathbf{v}_1 \sim \mathbf{e}_1$  because

$$(\mathbf{I} - \omega \mathbf{u} \mathbf{u}^\dagger) \mathbf{v} = \mathbf{v}_1 - \frac{\left( 1 + \frac{\mathbf{v}_1^\dagger \mathbf{u}}{\mathbf{u}^\dagger \mathbf{v}_1} \right) \mathbf{u} \mathbf{u}^\dagger \mathbf{v}_1}{2|\mathbf{v}_1|^2 \mp |\mathbf{v}_1| (v_{i1} + v_{i1}^*)} \quad (\text{A.9})$$

$$= \mathbf{v}_1 - \frac{(\mathbf{u}^\dagger \mathbf{v}_1 + \mathbf{v}_1^\dagger \mathbf{u})(\mathbf{v}_1 \mp |\mathbf{v}_1| \mathbf{e}_1)}{2|\mathbf{v}_1|^2 \mp |\mathbf{v}_1| (v_{i1} + v_{i1}^*)} \quad (\text{A.10})$$

$$= \mathbf{v}_1 - \frac{(|\mathbf{v}_1|^2 \mp |\mathbf{v}_1| v_{i1} + |\mathbf{v}_1|^2 \mp |\mathbf{v}_1| v_{i1}^*)(\mathbf{v}_1 \mp |\mathbf{v}_1| \mathbf{e}_1)}{2|\mathbf{v}_1|^2 \mp |\mathbf{v}_1| (v_{i1} + v_{i1}^*)} \quad (\text{A.11})$$

$$= \pm |\mathbf{v}_1| \mathbf{e}_1. \quad (\text{A.12})$$

This implies, that  $\mathbf{A}' = \mathbf{P} \mathbf{A} \mathbf{P}^\dagger$  is a block diagonal matrix of the desired form

$$\mathbf{A}' = \begin{pmatrix} \lambda_1 & & & \\ & * & * & \\ & & * & * \\ & & & * \end{pmatrix}. \quad (\text{A.13})$$

To evaluate the matrix product  $\mathbf{PAP}^\dagger$  in the most efficient way, we first calculate the quantities

$$\mathbf{p} = \omega^* \mathbf{A} \mathbf{u}, \tag{A.14}$$

$$K = \frac{\omega}{2} \mathbf{u}^\dagger \mathbf{p}, \tag{A.15}$$

$$\mathbf{q} = \mathbf{p} - K \mathbf{u}. \tag{A.16}$$

With these definitions, we have

$$\mathbf{A}' = \mathbf{P}(\mathbf{A} - \mathbf{p} \mathbf{u}^\dagger) \tag{A.17}$$

$$= \mathbf{A} - \mathbf{p} \mathbf{u}^\dagger - \mathbf{u} \mathbf{p}^\dagger + 2K \mathbf{u} \mathbf{u}^\dagger \tag{A.18}$$

$$= \mathbf{A} - \mathbf{q} \mathbf{u}^\dagger - \mathbf{u} \mathbf{q}^\dagger, \tag{A.19}$$

which is the final expression that is implemented in the program. Note that in the last step we have made use of the fact that  $K$  is real, as can be seen from eqs. (A.15) and (A.14), and from the hermiticity of  $\mathbf{A}$ .

Once we have brought  $\mathbf{A}$  to the form (A.13), it is straightforward to calculate the two remaining eigenvalues by directly solving the characteristic equation. The corresponding eigenvectors  $\mathbf{v}_{1,2}$  are orthogonal to the columns of  $\mathbf{A}' - \lambda_{1,2} \mathbf{I}$  (and to  $\mathbf{v}_1$ ). They are therefore obtained by simply rotating the columns of these matrices by 90 degrees. To transform them back to the original basis, we multiply them with  $\mathbf{P}^\dagger$ .

The only remaining problem is to find the first eigenvalue  $\lambda_1$  which is required to start the algorithm. We calculate it by searching for a root of the characteristic polynomial with the Steffenson algorithm [73]. This algorithm is based on Newton's method which simply follows the gradient of the function, combined with Aitken's  $\Delta^2$  method to accelerate the convergence [75]. Although there are specialized algorithms for finding the roots of polynomials (e.g. the algorithms by Muller and Laguerre [76]), we have not experimented with them. These algorithms require the use of complex arithmetic, including square roots of complex numbers, therefore we do not expect them to give a great improvement compared to the Steffenson algorithm even if they may need fewer iteration to converge.

The Steffenson method requires a starting value  $\lambda_0$ , the choice of which turned out to be non-trivial because we must make sure that it does not accidentally coincide with an extremal point of the function. At these points the derivative vanishes, and so Newton's method cannot be used. This problem occurred very frequently when we tested our algorithm with integer matrices. Since extremal points of the characteristic polynomial can only lie between its roots, we choose for  $\lambda_0$  a value which is guaranteed to be larger than the largest root. We can find such a value by using Gerschgorin's theorem [77], which states that all eigenvalues of an  $n \times n$  matrix  $\mathbf{A}$  are contained in the union of

circular discs

$$\bigcup_j \left\{ x \in \mathbb{C} : |x - a_{jj}| \leq \sum_{\substack{k=1 \\ k \neq j}}^n |a_{jk}| \right\}. \quad (\text{A.20})$$

This implies, that all eigenvalues  $\lambda_i$  satisfy

$$\lambda_i \leq \max_j \sum_{k=1}^n |a_{jk}|, \quad (\text{A.21})$$

so the right hand side of this inequality would provide a suitable starting value for the Steffenson algorithm. To avoid taking square roots, we weaken the bound slightly and take

$$\lambda_0 = \max_j \sum_{k=1}^n (|\operatorname{Re} a_{jk}| + |\operatorname{Im} b_{jk}|). \quad (\text{A.22})$$

Note that this gives our algorithm the property that  $\lambda_1$  is always the largest eigenvalue of  $\mathbf{A}$ .

To make the algorithm robust, we need to give some thought to its numerical accuracy. The Steffenson root finder and the Householder transformation are widely used and are known to be stable and accurate. The cross product, however, may introduce large errors if it is applied to vectors which are almost linearly dependent because in such a case it contains differences of almost equal numbers. Therefore, if our algorithm detects that the first and second columns  $\mathbf{A}_1$  and  $\mathbf{A}_2$  of the matrix in Eq. (A.1) are almost linearly dependent, it does not use the cross product, but takes them to be *exactly* linearly dependent, i.e.  $\mathbf{A}_1 = \mu \mathbf{A}_2$ , so that  $\mathbf{v}_1$  can immediately be obtained as

$$\mathbf{v}_1 = \frac{1}{\sqrt{1 + |\mu|^2}} \begin{pmatrix} 1 \\ -\mu^* \\ 0 \end{pmatrix}. \quad (\text{A.23})$$

This approach is justified because it is known that Hermitian eigenvector problems are always well conditioned [77] in the sense that small changes in the matrix entries will only cause small changes in the eigenvalues and eigenvectors.

Finally, the performance can be optimized by exploiting the hermiticity of  $\mathbf{A}$  and performing all operations only on the upper triangular parts of the matrix.

## A.2 Varying matter density

To calculate the neutrino oscillation probabilities in matter of varying density, there are two different approaches:

- Dividing the neutrino trajectory into **slabs of constant density**, calculating the S-Matrix for each slab according to the methods described in the previous section, and multiplying all contributions. For complex simulations, this approach is only feasible if the number of slabs is very small. Fortunately, we have seen in Sec. 4 that for the PREM profile of the Earth it is usually sufficient to work with only three layers, two for the mantle and one for the core. The S-Matrices for the two mantle layers are identical.
- **Solving the time-dependent Schrödinger equation**

$$i\frac{\partial\psi}{\partial t} = (H_0 + V(t))\psi \quad (\text{A.24})$$

directly with a standard ODE solver such as the Runge-Kutta or Bulirsch-Stoer algorithms [76, 77]. In Eq. (A.24),  $H_0$  is the vacuum Hamiltonian, and  $V$  is the (non-constant) matter potential

The second option requires some discussion. Naïve application of an ODE solver to the neutrino evolution equation is very inefficient because it requires a large number of iterations to correctly follow the oscillatory behavior of the S-Matrix elements. The basic idea for solving an initial value problem  $dx/dt = f(x, t)$  with  $x(t_0) = x_0$  is to evolve  $x(t)$  and  $dx(t)/dt$  over a small distance  $h$  in each iteration by using polynomial extrapolation. Adaptive step size control is used to dynamically vary  $h$  in order to achieve the optimal balance between performance and accuracy. For oscillatory functions, however, this is not very efficient because polynomial extrapolation is only accurate over some fraction of the oscillation period, i.e. the step size controller will adjust  $h$  to a value which is smaller than the smallest oscillation length in the problem. As an example, for 100 MeV neutrinos, the atmospheric oscillation length is 113 km, so for a baseline of 10,000 km, the algorithm would need at least 100 iterations. In reality, several thousand iterations are required to achieve an accuracy on the per cent level.

This problem can be alleviated by noting that in most regions of the  $L$ - $E$ -plane, the oscillations are mainly determined by the vacuum Hamiltonian  $H_0$ , with only minor modifications from the matter potential  $V(t)$ . We can mask out the vacuum part by going from the Schrödinger picture to the interaction picture. We therefore define

$$\psi_I = e^{iH_0 t}\psi, \quad (\text{A.25})$$

$$V_I = e^{iH_0 t}V(t)e^{-iH_0 t}. \quad (\text{A.26})$$

In these transformed variables, Eq. (A.24) becomes

$$\frac{\partial\psi_I}{\partial t} = V_I(t)\psi_I. \quad (\text{A.27})$$

It can be seen from Fig. A.1 that  $\psi_I$  is usually much smoother than  $\psi$ , so the ODE solver can choose a larger step size and therefore needs fewer iterations to solve Eq. (A.27). To

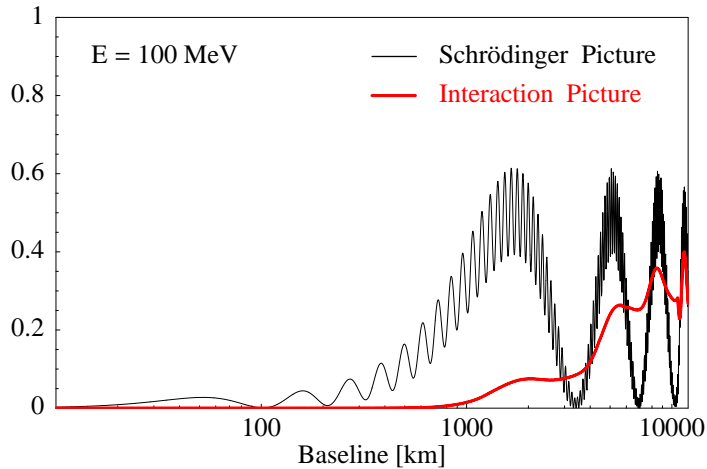


Figure A.1: Squared moduli of the  $e\mu$  S-Matrix element in the PREM profile for the Schrödinger picture and for the interaction picture. In the interaction picture, the (trivial) vacuum oscillations are transformed away, making the numerical solution of the problem much more efficient.

obtain the actual oscillation probabilities  $|\psi_\alpha|^2$ , the resulting vector  $\psi_I(t)$  can be easily transformed back to the Schrödinger picture using Eq. (A.25).

### A.3 Comparison of the algorithms

The computational efficiency of the different algorithms discussed so far is shown in Fig. A.2. As expected, the performance of the constant density algorithms is almost independent of the neutrino energy (and of the baseline). However, the algorithms differ by almost a factor of 10 in performance. This proves that indeed the GSL and LAPACK routines are not optimized for small matrices. We are aware that our  $3 \times 3$  algorithm can be optimized even further on the implementational level, but this would make the code unreadable and thus unmaintainable, therefore we have refrained from doing so.

The ODE solvers in the PREM profile are most efficient at high energies (or, equivalently, short baselines), where only few oscillation lengths need to be retraced. When going to energies around 1 MeV, the performance drops by up to three orders of magnitude if the calculation is performed in the Schrödinger picture, but by only one order of magnitude if the interaction picture is used. We have compared the performance of two different ODE solvers from the GNU Scientific Library: A standard Runge-Kutta-Fehlberg method, and a more sophisticated implicit Bulirsch-Stoer algorithm. However, the dotted curves in Fig. A.2 show, that the more sophisticated algorithm is less efficient for our problem.

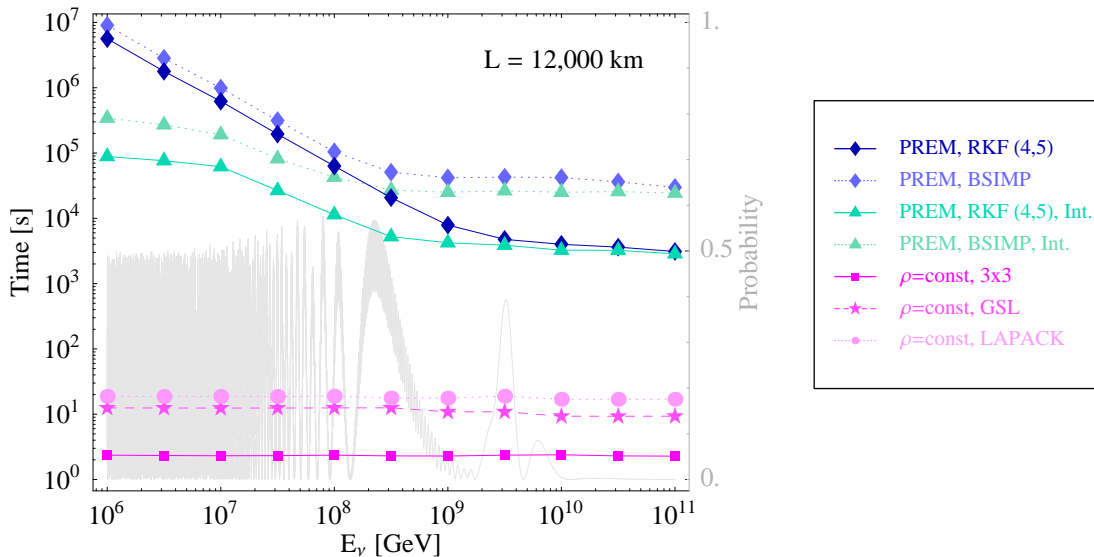


Figure A.2: Computational efficiency of various algorithms for the calculation of neutrino oscillation probabilities. We measured the time required to calculate the probabilities for all 9 oscillation channels 1 Million times on a AMD Athlon XP 2000+ processor with a clock frequency of 1.67 GHz . For oscillations in the PREM profile, we compare a Runge-Kutta-Fehlberg (4,5) (RKF (4,5)) and an Implicit Bulirsch-Stoer (BSIMP) integrator, both in the Schrödinger Picture (Eq. (A.24)) and in the Interaction Picture (Eq. (A.27)). For constant matter density, we compare the optimized algorithm for  $3 \times 3$  matrices with the eigensystem evaluators of the GNU Scientific Library and of LAPACK. For reference, we also show the  $\nu_\mu \rightarrow \nu_e$  oscillation probability (gray curve).

The performance of the ODE solvers is several orders of magnitude worse than that of the constant density methods, therefore we conclude that for all practical purposes it is advisable to divide the matter profile into layers of constant density.



## Appendix B

### Geometry of atmospheric neutrino detectors

As discussed in chapter 5, the efficiencies for  $\mu$ -like neutrinos in the Super-Kamiokande detector exhibit a complicated dependence on the energy and on the zenith angle. While the energy dependence for FC and PC events is available from Monte Carlo simulations, we must rely on our own geometrical arguments for the angular dependence. For upward going muons, also the target volume has to be determined geometrically.

#### B.1 Calculation of the muon range in matter

The most important ingredient in our arguments is the distance  $L_\mu$  that a secondary muon can travel in the detector. For a given energy  $E_\mu$ , this distance depends only on the material the muon passes through. For FC and PC events this is water, while for upward going muons it is partly water and partly rock. For simplicity, we will however assume upward going muons to travel in water as well. Of course, we will thus overestimate  $L_\mu$  for these events by a factor of about  $\rho_{\text{rock}}/\rho_{\text{H}_2\text{O}}$ , the ratio of the water and rock densities, so the target volume will be too large. This is however compensated by the cross sections, which are smaller in water by  $(\rho_{\text{rock}}/\rho_{\text{H}_2\text{O}})^{-1}$ , so that the overall result is approximately correct.

$L_\mu$  can be calculated quantitatively from the initial muon energy  $E_\mu$  (which we take to be equal to  $E_\nu$ , neglecting nuclear recoil) and several material dependent parameters by integrating the inverse of the Bethe-Bloch formula [43, 78]

$$-\frac{dE}{dx} = K\rho z^2 \frac{Z}{A} \frac{1}{\beta^2} \left[ \frac{1}{2} \ln \frac{2m_e \beta^2 \gamma^2 T_{\text{max}}}{I^2} - \beta^2 - \frac{\delta}{2} \right] + E_\mu b(E_\mu), \quad (\text{B.1})$$

where

$$T_{\text{max}} = \frac{2m_e \beta^2 \gamma^2}{1 + 2\gamma \frac{m_e}{m_\mu} + \left(\frac{m_e}{m_\mu}\right)^2} \quad (\text{B.2})$$

and

$$\delta = \begin{cases} 0 & \text{for } \log_{10} \beta\gamma < X_0 \\ 2 \ln 10 \cdot \log_{10} \beta\gamma + a(X_1 - \log_{10} \beta\gamma)^m + C & \text{for } X_0 < \log_{10} \beta\gamma < X_1 \\ 2 \ln 10 \cdot \log_{10} \beta\gamma + C & \text{for } X_1 < \log_{10} \beta\gamma \end{cases} \quad (\text{B.3})$$

Symbol	Description	Value for H <sub>2</sub> O
$E_\mu$	Muon energy	
$\beta$	Muon velocity in units of $ct$	
$\gamma$	$\sqrt{1 - \beta^2}$	
$K$	Kinematical pre-factor for ionization processes	0.307075 MeV cm <sup>2</sup> /g
$\rho$	Density of target material	1 g/cm <sup>3</sup>
$z$	Charge of incident particle	-1
$Z/A$	Proton-Nucleon ratio of absorber	1/2
$m_e$	Electron mass	0.5110 MeV
$m_\mu$	Muon mass	105.7 MeV
$T_{\max}$	Max. kinetic energy of electron after ionization	
$I$	Mean excitation energy of target material	75.0 eV
$b(E_\mu)$	Effect of radiative processes	$3 \cdot 10^{-6}$ cm <sup>2</sup> g <sup>-1</sup>
$\delta$	Density effect correction	
$C$		-3.5017
$X_0$		0.2400
$X_1$		2.8004
$a$		0.09116
$m$		3.4773

Table B.1: Parameters of the Bethe-Bloch formula. Most numerical values are taken from ref. [78]. Note that some of them (in particular  $b(E_\mu)$ ) are only rough approximations.

The first term in Eq. (B.1) describes energy loss by ionization, while the last term is a phenomenological parameterization of radiative effects. The quantities appearing in the Bethe-Bloch formula are listed in table B.1, along with their numerical values for H<sub>2</sub>O.

## B.2 Angular efficiencies for contained events

The geometry of FC and PC events in Super-Kamiokande is illustrated in Fig. B.1. The detector is a cylindrical vessel filled with water, and is subdivided into the inner detector (ID) with a radius of  $R_{\text{ID}} = 16.9$  m and a height of  $Y_{\text{ID}} = 36.2$  m, and the surrounding outer detector (OD) forming a shell with a thickness of about  $D_{\text{OD}} = 2.1$  m. The OD and the ID are separated by the photomultiplier mounting structure, which constitutes an inactive region of  $D_{\text{PMT}} = 0.55$  m.

The criteria for an event to be called fully contained are

1. The primary vertex is located inside the “fiducial volume” (FV) which is defined by the requirement that the distance from the vertex to the inner detector walls is

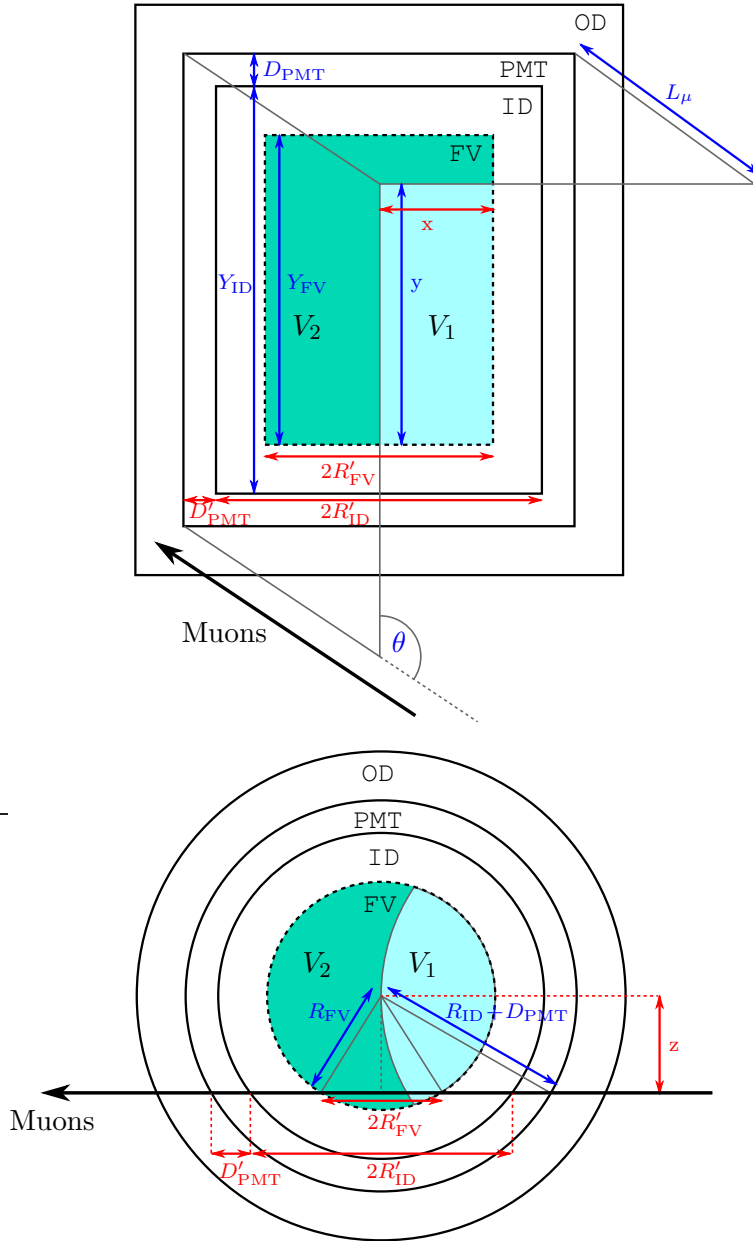


Figure B.1: Geometry of FC and PC events. The drawings show a vertical (top) and a horizontal (bottom) cut through the cylindrical Super-Kamiokande detector. Quantities labeled in red (grey) depend on  $z$ . A muon neutrino that has interacted in the shaded region  $V_1$  ( $V_2$ ) will be reconstructed as FC (PC).

at least  $R_{\text{ID}} - R_{\text{FV}} = 2$  m. The FV is depicted by the dotted line in Fig. B.1.

2. The secondary muon is not seen in the OD. This means that the distance  $L_\mu$  it can travel in water is smaller than the distance from the primary vertex to the inner OD walls in direction  $\theta$ .

The volume in which these criteria are fulfilled is shown as the light shaded region  $V_1$  in Fig. B.1. The angular efficiencies  $\epsilon_{\text{FC}}^\theta$  are proportional to  $V_1$ . They are normalized such that they leave the total number of (unoscillated) events unchanged because the Monte Carlo based energy efficiency factors  $\epsilon_{\text{FC}}^E$  are already properly normalized.

$V_1$  is given by

$$V_1(E, \theta) = 2 \int_0^{R_{\text{FV}}} dz x(z) \cdot y, \quad (\text{B.4})$$

where

$$x(z) = \max\left(0, \min\left(2R'_{\text{FV}}(z), 2R'_{\text{ID}}(z) + D'_{\text{PMT}} - L_\mu(E) \sin \theta\right)\right), \quad (\text{B.5})$$

$$y = \max\left(0, \min\left(Y_{\text{FV}}, Y_{\text{ID}} + D_{\text{PMT}} - L_\mu(E) |\cos \theta|\right)\right), \quad (\text{B.6})$$

as can be read of from the upper part of Fig. B.1.  $Y_{\text{FV}}$ ,  $Y_{\text{ID}}$  and  $D_{\text{PMT}}$  have already been given above. The calculation of the remaining quantities is illustrated in the bottom panel of Fig. B.1:

$$R'_{\text{FV}}(z) = \sqrt{R_{\text{FV}}^2 - z^2}, \quad (\text{B.7})$$

$$R'_{\text{ID}}(z) = \sqrt{R_{\text{ID}}^2 - z^2}, \quad (\text{B.8})$$

$$D'_{\text{PMT}}(z) = \sqrt{(R_{\text{ID}} + D_{\text{PMT}})^2 - z^2} - R'_{\text{ID}}(z). \quad (\text{B.9})$$

The criteria for PC events are

1. The primary vertex is located in the fiducial volume.
2. The secondary lepton gives a signal in the OD.

They are fulfilled in the dark shaded region  $V_2$  in Fig. B.1, the volume of which is  $V_2 = \pi R_{\text{FV}}^2 Y_{\text{FV}} - V_1$ .  $\epsilon_{\text{PC}}^\theta$  is proportional to  $V_2$ , and normalized in the same way as  $\epsilon_{\text{FC}}^\theta$ .

### B.3 Efficiencies for upward going muon events in Super-Kamiokande

The efficiencies for upward through-going and upward stopping muon events in Super-Kamiokande are calculated similarly to those for FC and PC events. An event is tagged as an upward going muon if a muon with  $\cos \theta < 0$  is seen in the OD, and its track length in the ID is at least  $L_{\mu, \min} = 7$  m. To fulfill these requirements a muon must have been created in the shaded region  $V_1$  of Fig. B.2. In principle, neutrino interactions in the OD also contribute about 6.6% of the US and 1.8% of the UT events. However, such interactions are only reconstructed as upward going muon events if the vertex is close enough to the outer detector walls so that a sufficient amount of Čerenkov light reaches the OD photodetectors. Since it is difficult to estimate under which conditions this is the case, we neglect interactions in the OD completely.

If an upward going muon is energetic enough to pass through  $V_2$ , it will give an exit signal in the OD and therefore be recorded as through-going. If no exit signal is seen, the event is an upward stopping muon. These considerations lead to the following expressions for the efficiencies:

$$\epsilon_{\text{UT}}^E \cdot \epsilon_{\text{UT}}^\theta = \max(0, V_1 - V_2)/V_{\text{ID}}, \quad (\text{B.10})$$

$$\epsilon_{\text{US}}^E \cdot \epsilon_{\text{US}}^\theta = \max(V_1, V_2)/V_{\text{ID}}, \quad (\text{B.11})$$

where the normalization by the ID volume  $V_{\text{ID}} = \pi R_{\text{ID}}^2 Y_{\text{ID}}$  is necessary to fix the ratio (US + UT)/(FC + PC) to. Using the standard formula for the area of a polygon, we now calculate

$$V_1 = 2 \int_0^{R_{\text{ID}}} dz \sum_{i=0}^5 (P_{i,x} P_{i+1,y} - P_{i,y} P_{i+1,x}), \quad (\text{B.12})$$

$$V_2 = 2 \int_0^{R_{\text{ID}}} dz \sum_{i=0}^5 (Q_{i,x} Q_{i+1,y} - Q_{i,y} Q_{i+1,x}). \quad (\text{B.13})$$

The edges of the polygons are

$$P_0 = \left( (b + D_{\text{PMT}} + D_{\text{OD}}) |\tan \theta|; -(b + D_{\text{PMT}} + D_{\text{OD}}) \right), \quad (\text{B.14})$$

$$P_1 = \left( L_\mu \sin \theta; -L_\mu |\cos \theta| \right), \quad (\text{B.15})$$

$$P_2 = \left( L_\mu \sin \theta + X; -L_\mu |\cos \theta| \right), \quad (\text{B.16})$$

$$P_3 = \left( L_\mu \sin \theta + X; -L_\mu |\cos \theta| + Y \right), \quad (\text{B.17})$$

$$P_4 = \left( X + a + D'_{\text{PMT}} + D'_{\text{OD}}; Y - (a + D'_{\text{PMT}} + D'_{\text{OD}}) |\cot \theta| \right), \quad (\text{B.18})$$

$$P_5 = \left( X + a + D'_{\text{PMT}} + D'_{\text{OD}}; -(b + D_{\text{PMT}} + D_{\text{OD}}) \right), \quad (\text{B.19})$$

and

$$Q_0 = (0; 0), \quad (\text{B.20})$$

$$Q_1 = (X; 0), \quad (\text{B.21})$$

$$Q_2 = (X; Y), \quad (\text{B.22})$$

$$Q_3 = (X - D_{\text{PMT}}|\tan \theta|; Y + D_{\text{PMT}}), \quad (\text{B.23})$$

$$Q_4 = (-D'_{\text{PMT}}; Y + D_{\text{PMT}}), \quad (\text{B.24})$$

$$Q_5 = (-D'_{\text{PMT}}; D'_{\text{PMT}}|\cot \theta|). \quad (\text{B.25})$$

The remaining quantities are given by

$$X = 2R'_{\text{ID}}(z) - L_{\mu,\text{min}} \sin \theta, \quad (\text{B.26})$$

$$Y = Y_I D - L_{\mu,\text{min}}|\cos \theta|, \quad (\text{B.27})$$

$$a = L_{\mu,\text{min}} \sin \theta, \quad (\text{B.28})$$

$$b = L_{\mu,\text{min}}|\cos \theta|, \quad (\text{B.29})$$

$$R'_{\text{ID}}(z) = \sqrt{R_{\text{ID}}^2 - z^2}, \quad (\text{B.30})$$

$$D'_{\text{PMT}}(z) = \sqrt{(R_{\text{ID}} + D_{\text{PMT}})^2 - z^2} - R'_{\text{ID}}(z), \quad (\text{B.31})$$

$$D'_{\text{OD}}(z) = \sqrt{(R_{\text{ID}} + D_{\text{PMT}} + D_{\text{OD}})^2 - z^2} - R'_{\text{ID}}(z) - D'_{\text{PMT}}(z). \quad (\text{B.32})$$

For nearly horizontal muons, a special treatment is necessary because for these,  $Q_3$  may lie on the vertical boundary of the PMT structure, above  $Q_5$ . If this is the case,  $Q_3$  is given by  $(-D'_{\text{PMT}}; Y + (X + D'_{\text{PMT}})|\cot \theta|)$ , and  $Q_4$  is omitted. A similar situation can arise for nearly vertical muons, where correspondingly  $Q_5$  has to be modified and  $Q_4$  is again omitted. Furthermore, we have to make sure that  $V_1$  is set to zero if  $L_{\mu}$  is so small that the muons cannot pass the OD and the PMT layer, and still reach the minimum ID track length  $L_{\mu,\text{min}}$ .

## B.4 Efficiencies for upward going muon events in ATLAS

To calculate the upward going muon efficiencies for ATLAS, we use the same algorithms as for Super-Kamiokande, but since ATLAS has the shape of a horizontally oriented cylinder,  $|\cos \theta|$  and  $\sin \theta$  as well as  $|\tan \theta|$  and  $|\cot \theta|$  are interchanged in the calculation. Furthermore, ATLAS has no outer detector, and we assume that no fiducial volume or minimum track length cuts are necessary. The radius of ATLAS is taken to be 11 m, and its length is 42 m.





## Appendix C

### Neutrino oscillations in the three-layer model of the earth

In this appendix, we are going to derive the two-flavour neutrino oscillation probabilities in three layers of alternating matter densities  $\rho_1$ ,  $\rho_2$ , and  $\rho_3 = \rho_1$ , and thicknesses  $L_1$ ,  $L_2$ , and  $L_3 = L_1$ , respectively. This corresponds to the three-layer model of the Earth from chapter 4, if we set  $\rho_1 = \rho_{\text{mantle}}$  and  $\rho_2 = \rho_{\text{core}}$ . We denote the mixing angles in matter by  $\theta_1$  and  $\theta_2$  and the effective mass squared differences by  $\Delta m_1^2$  and  $\Delta m_2^2$ . Our starting point is the two-flavour S-matrix in matter of constant density,

$$\begin{aligned} S_j &= \begin{pmatrix} c_j & s_j \\ -s_j & c_j \end{pmatrix} \begin{pmatrix} e^{i\Delta_j} & 0 \\ 0 & e^{-i\Delta_j} \end{pmatrix} \begin{pmatrix} c_j & -s_j \\ s_j & c_j \end{pmatrix} \\ &= \begin{pmatrix} c_j^2 e^{i\Delta_j} + s_j^2 e^{-i\Delta_j} & -s_j c_j (e^{i\Delta_j} - e^{-i\Delta_j}) \\ -s_j c_j (e^{i\Delta_j} - e^{-i\Delta_j}) & s_j^2 e^{i\Delta_j} + c_j^2 e^{-i\Delta_j} \end{pmatrix}, \end{aligned} \quad (\text{C.1})$$

where we have used the notation  $c_j = \cos \theta_j$ ,  $s_j = \sin \theta_j$  and  $\Delta_j = \Delta m_j^2 L_j / 4E$ . Let us for the moment abbreviate  $S_j$  by

$$S_j = \begin{pmatrix} A_j & B_j \\ B_j & A_j^* \end{pmatrix}, \quad (\text{C.2})$$

with

$$A_j = c_j^2 e^{i\Delta_j} + s_j^2 e^{-i\Delta_j} \quad (\text{C.3})$$

$$B_j = -s_j c_j (e^{i\Delta_j} - e^{-i\Delta_j}). \quad (\text{C.4})$$

The evolution matrix for the full trajectory, crossing all three layers, then has the form

$$\begin{aligned} S &= S_1 S_2 S_1 \\ &= \begin{pmatrix} A_1^2 A_2 + 2A_1 B_1 B_2 + A_2^* B_1^2 & A_1 A_2 B_1 + |A_1|^2 B_2 + B_1^2 B_2 + A_1^* A_2^* B_1 \\ A_1 A_2 B_1 + |A_1|^2 B_2 + B_1^2 B_2 + A_1^* A_2^* B_1 & A_2 B_1^2 + 2A_1^* B_1 B_2 + A_1^{*2} A_2^* \end{pmatrix}, \end{aligned} \quad (\text{C.5})$$

Using the relations  $P_j = |B_j|^2 = -B_j^2$  and  $1 - P_j = |A_j|^2$  for the oscillation and survival probabilities in each individual layer, we obtain for the full two-flavour survival probability

$$1 - P = |A_1^2 A_2 + 2A_1 B_1 B_2 + A_2^* B_1^2|^2 \quad (\text{C.6})$$

$$\begin{aligned} &= (1 - P_1)^2 P_2 + 4(1 - P_1)P_1 P_2 + (1 - P_2)P_1^2 \\ &\quad + 2(1 - P_1)(A_1 A_2 B_1^* B_2^* + A_1^* A_2^* B_1 B_2) - P_1(A_1^2 A_2^2 + A_1^{*2} A_2^{*2}) \\ &\quad + 2P_1(A_1 A_2 B_1^* B_2 + A_1^* A_2^* B_1 B_2^*) \\ &= (1 - P_1)^2 P_2 + 4(1 - P_1)P_1 P_2 + (1 - P_2)P_1^2 \\ &\quad + 2(1 - 2P_1)(A_1 A_2 B_1^* B_2^* + A_1^* A_2^* B_1 B_2) - P_1(A_1^2 A_2^2 + A_1^{*2} A_2^{*2}), \end{aligned} \quad (\text{C.7})$$

where in the last step we have used  $B_j^* = -B_j$ . We can now substitute back eqs. (C.3) and (C.4) to obtain

$$\begin{aligned} 1 - P &= (1 - P_1)^2(1 - P_2) + 4(1 - P_1)P_1 P_2 + (1 - P_2)P_1^2 \\ &\quad + 2(1 - 2P_1) \left[ (c_1^2 e^{i\Delta_1} + s_1^2 e^{-i\Delta_1})(c_2^2 e^{i\Delta_2} + s_2^2 e^{-i\Delta_2}) \right. \\ &\quad \quad \left. \cdot s_1 c_1 (e^{i\Delta_1} - e^{-i\Delta_1}) \cdot s_2 c_2 (e^{i\Delta_2} - e^{-i\Delta_2}) + c.c. \right] \\ &\quad - P_1 \left[ (c_1^4 e^{2i\Delta_1} + 2s_1^2 c_1^2 + s_1^4 e^{-2i\Delta_1})(c_2^4 e^{2i\Delta_2} + 2s_2^2 c_2^2 + s_2^4 e^{-2i\Delta_2}) + c.c. \right] \end{aligned} \quad (\text{C.8})$$

$$\begin{aligned} &= (1 - P_1)^2(1 - P_2) + 4(1 - P_1)P_1 P_2 + (1 - P_2)P_1^2 \\ &\quad + 2(1 - 2P_1) \left[ -\sin 2\theta_1 \sin 2\theta_2 \sin \Delta_1 \sin \Delta_2 \right. \\ &\quad \quad \left( (e^{i(\Delta_1 + \Delta_2)} + e^{-i(\Delta_1 + \Delta_2)})(c_1^2 c_2^2 + s_1^2 s_2^2) \right. \\ &\quad \quad \left. \left. + (e^{i(\Delta_1 - \Delta_2)} + e^{-i(\Delta_1 - \Delta_2)})(c_1^2 s_2^2 + s_1^2 c_2^2) \right) \right] \\ &\quad - P_1 \left[ (e^{2i(\Delta_1 + \Delta_2)} + e^{-2i(\Delta_1 + \Delta_2)})(c_1^4 c_2^4 + s_1^4 s_2^4) \right. \\ &\quad \quad + (e^{2i(\Delta_1 + \Delta_2)} + e^{-2i(\Delta_1 + \Delta_2)})(c_1^4 s_2^4 + c_2^4 s_1^4) \\ &\quad \quad + (e^{2i\Delta_1} + e^{-2i\Delta_1}) \cdot 2s_2^2 c_2^2 (c_1^4 + s_1^4) + (e^{2i\Delta_2} + e^{-2i\Delta_2}) \cdot 2s_1^2 c_1^2 (c_2^4 + s_2^4) \\ &\quad \quad \left. + 8s_1^2 c_1^2 s_2^2 c_2^2 \right]. \end{aligned} \quad (\text{C.9})$$

To proceed, we need the following formulas for higher powers of trigonometric functions:

$$c_1^2 c_2^2 + s_1^2 s_2^2 = \frac{1}{2} + \frac{1}{2} \cos 2\theta_1 \cos 2\theta_2 \quad (\text{C.10})$$

$$c_1^2 s_2^2 + s_1^2 c_2^2 = \frac{1}{2} - \frac{1}{2} \cos 2\theta_1 \cos 2\theta_2 \quad (\text{C.11})$$

$$c_1^4 c_2^4 + s_1^4 s_2^4 = \frac{1}{2} \cos 2\theta_1 \cos 2\theta_2 + \frac{1}{8} (1 + \cos^2 2\theta_1)(1 + \cos^2 2\theta_2) \quad (\text{C.12})$$

---


$$c_1^4 s_2^4 + s_1^4 c_2^4 = -\frac{1}{2} \cos 2\theta_1 \cos 2\theta_2 + \frac{1}{8} (1 + \cos^2 2\theta_1)(1 + \cos^2 2\theta_2) \quad (\text{C.13})$$

$$c_1^4 + s_1^4 = \frac{1}{2} + \frac{1}{2} \cos^2 2\theta_1. \quad (\text{C.14})$$

Inserting these expressions into Eq. (C.9) yields

$$\begin{aligned} 1 - P &= (1 - P_1)^2 (1 - P_2) + 4(1 - P_1)P_1P_2 + (1 - P_2)P_1^2 \\ &\quad - 2(1 - 2P_1) \sin 2\theta_1 \sin 2\theta_2 \sin \Delta_1 \sin \Delta_2 \\ &\quad \left( \cos(\Delta_1 + \Delta_2)(1 + \cos 2\theta_1 \cos 2\theta_2) + \cos(\Delta_1 - \Delta_2)(1 - \cos 2\theta_1 \cos 2\theta_2) \right) \\ &\quad - P_1 \left[ \cos(2\Delta_1 + 2\Delta_2) \left[ \cos 2\theta_1 \cos 2\theta_2 + \frac{1}{4}(1 + \cos^2 2\theta_1)(1 + \cos^2 2\theta_2) \right] \right. \\ &\quad \left. + \cos(2\Delta_1 - 2\Delta_2) \left[ -\cos 2\theta_1 \cos 2\theta_2 + \frac{1}{4}(1 + \cos^2 2\theta_1)(1 + \cos^2 2\theta_2) \right] \right. \\ &\quad \left. + \frac{1}{2} \cos 2\Delta_1 \cdot \sin^2 2\theta_2 (1 + \cos^2 2\theta_1) + \frac{1}{2} \cos 2\Delta_2 \cdot \sin^2 2\theta_1 (1 + \cos^2 2\theta_2) \right. \\ &\quad \left. + \frac{1}{2} \sin^2 2\theta_1 \sin^2 2\theta_2 \right] \quad (\text{C.15}) \\ &= (1 - P_1)^2 (1 - P_2) + 4(1 - P_1)P_1P_2 + (1 - P_2)P_1^2 \\ &\quad - 4(1 - 2P_1) \sin 2\theta_1 \sin 2\theta_2 \sin \Delta_1 \sin \Delta_2 (\cos \Delta_1 \cos \Delta_2 - \cos 2\theta_1 \cos 2\theta_2 \sin \Delta_1 \sin \Delta_2) \\ &\quad - P_1 \left[ \frac{1}{2} (1 + \cos^2 2\theta_1)(1 + \cos^2 2\theta_2) \cos 2\Delta_1 \cos 2\Delta_2 \right. \\ &\quad \left. + \frac{1}{2} \sin^2 2\theta_1 \sin^2 2\theta_2 - 2 \cos 2\theta_1 \cos 2\theta_2 \sin 2\Delta_1 \sin 2\Delta_2 \right. \\ &\quad \left. + \frac{1}{2} \sin^2 2\theta_1 (1 + \cos^2 2\theta_2) \cos 2\Delta_2 + \frac{1}{2} \sin^2 2\theta_2 (1 + \cos^2 2\theta_1) \cos 2\Delta_1 \right]. \quad (\text{C.16}) \end{aligned}$$

The expression for the transition probability is correspondingly

$$\begin{aligned} P &= (1 - P_1)^2 P_2 + 2(1 - P_1)(1 - 2P_2)P_1 + P_1^2 P_2 \\ &\quad + 4(1 - 2P_1) \sin 2\theta_1 \sin 2\theta_2 \sin \Delta_1 \sin \Delta_2 (\cos \Delta_1 \cos \Delta_2 - \cos 2\theta_1 \cos 2\theta_2 \sin \Delta_1 \sin \Delta_2) \\ &\quad + P_1 \left[ \frac{1}{2} (1 + \cos^2 2\theta_1)(1 + \cos^2 2\theta_2) \cos 2\Delta_1 \cos 2\Delta_2 \right. \\ &\quad \left. + \frac{1}{2} \sin^2 2\theta_1 \sin^2 2\theta_2 - 2 \cos 2\theta_1 \cos 2\theta_2 \sin 2\Delta_1 \sin 2\Delta_2 \right. \\ &\quad \left. + \frac{1}{2} \sin^2 2\theta_1 (1 + \cos^2 2\theta_2) \cos 2\Delta_2 + \frac{1}{2} \sin^2 2\theta_2 (1 + \cos^2 2\theta_1) \cos 2\Delta_1 \right]. \quad (\text{C.17}) \end{aligned}$$

This is just Eq. (4.13).



## Acknowledgments

I wish to express my gratitude to my supervisor Manfred Lindner, who affiliated me to his group, who gave me this interesting and challenging subject for my diploma thesis, and who assisted my work with many helpful comments and discussions, but nevertheless left me the freedom to pursue own ideas as well. Furthermore, he allowed me to participate in several interesting and enjoyable scientific meetings, in particular the Young Scientists' Workshop at Ringberg Castle, and the Double Chooz collaboration meeting in Heidelberg.

I am also much obliged to Evgeny Akhmedov for patience with my many questions and for his excellent explanations of many of the more subtle aspects of neutrino physics. Srubabati Goswami deserves gratefulness for many helpful discussions on the simulation of atmospheric neutrinos. I wish to thank Patrick Huber, Mark Rolinec, and Walter Winter for sharing with me their extensive knowledge on future neutrino oscillation experiments, and on techniques for simulating them on a computer. I would furthermore like to thank Kathrin Hochmuth, Lothar Oberauer, Teresa Marrodán Undagoitia, and Michael Wurm, who were always willing to help when I needed an experimentalist's advice.

I am especially grateful to Kathrin Hochmuth, Alexander Merle, and Mark Rolinec for proof-reading this work and making many invaluable comments and suggestions.

Working in the TUM neutrino group has been a very enjoyable experience. Therefore, I would like to thank my colleagues for all the pleasurable scientific and non-scientific discussions: Florian Bauer, Alexander Blum, Marc-Thomas Eisele, Mathias Garny, Claudia Hagedorn, Andreas Hohenegger, Alexander Merle, Markus Michael Müller, Toshihiko Ota, Florian Plentinger, Werner Rodejohann, Michael Schmidt, our secretary Karin Ramm, and our visitors Evgeny Akhmedov, Naoyuki Haba, Toshifumi Jittoh, Rabi Mohapatra, Joe Sato, Yoshio Sato, and Alexei Yu. Smirnov. They all have contributed to the excellent atmosphere during many joyful coffee breaks, at the "T30 Formula Phi" kart races, and on innumerable other occasions.

This work would not have been possible without the continuous support from my parents, Karin and Herbert Kopp, who sparked my interest in the natural sciences, who made it possible for me to study in Munich, and who encouraged me on innumerable occasions.

Finally, I would like to thank the Studienstiftung des Deutschen Volkes, in particular Hella Kohrs-Kaumanns and Rudolf Höll, for supporting me during my studies.



# Index

- accelerator experiments
  - measurement of atmospheric parameters, 24, 27, 75
  - measurement of  $\theta_{13}$ , 27, 80–81
  - oscillation probability, *see* oscillation channels,  $\nu_\mu \rightarrow \nu_e$
- adaptive step size control, 89
- adiabatic flavour conversion, *see* MSW effect
- aliasing, 59
- ALICE, 57
- angular resolution
  - ATLAS, 66–68
  - Super-Kamiokande, 63–64
- antineutrinos, 18, 21
- appearance channels, *see* oscillation channels
- approximate oscillation probabilities, *see* Oscillation probabilities
- ATLAS
  - angular resolution, 66–68
  - backgrounds, 57
  - benchmark scenarios, 67
  - $\chi^2$  analysis, 68–71
  - efficiencies, 66–68, 98
  - energy resolution, 66–68
  - geometry, 98
  - overburden, 57
  - systematical errors, 72
  - target mass, 57
  - track reconstruction, 66–68
  - zenith angle distribution of events, 74
- atmospheric neutrinos
  - cross sections, 61
  - fluxes, 60
  - production height, 60
  - production reaction, 23
  - systematical uncertainties, 70
  - three-flavour effects in, 46, 55, 77
- atmospheric resonance, 19, 35, 41–42, 45, 56
- azimuthal angle, 60, 64
- backgrounds
  - cosmic muons in ATLAS, 57
  - flux error, 48
  - misidentified muons, 71
  - neutral current, 71
  - unknown sources, 52
- Bethe-Bloch formula, 93
- biases, *see* systematical errors
- bin-to-bin errors, *see* systematical errors
- binning
  - of atmospheric events, 69
- Bulirsch-Stoer algorithm, 90
- cancellation
  - of systematical errors, 47
- Čerenkov threshold, 64
- charge identification, 57, 69
- $\chi^2$  analysis
  - for atmospheric neutrinos, 68–71
  - for Double Chooz, 53
  - for reactor experiments, 48–51
- CMS, 57

- coherent forward scattering, 15
- conspiracy, 55
- core resonance, 41–42
- correlations, 38, 78
- cosmic muon background, 57
- cosmic rays, 23, 60
- CP violation
  - absence for  $\alpha = 0$  or  $\theta_{13} = 0$ , 38
  - in superbeam experiments, 27
  - in the  $\nu_\mu \rightarrow \nu_e$  channel, 35–38
- cross sections
  - for atmospheric neutrinos, 61–62
- deep-inelastic scattering, 62
- deficit of solar neutrinos, *see* solar neutrino problem
- degeneracies, 75, 79
- $\delta_{CP}$ , *see* CP violation
- $\Delta m_{21}^2$ , 25, 27
- $\Delta m_{31}^2$ , 24, 27, 75–77
- detector response function, 63
- diagonalization
  - of the Hamiltonian, 85–88
- directional information, *see* zenith angle
- disappearance channels, *see* oscillation channels
- Double Chooz
  - baseline, 53
  - $\chi^2$  analysis, 53
  - delayed near detector startup, 53
  - sensitivity to  $\theta_{13}$ , 27, 53
  - systematical errors, 53
  - target mass, 53
- Double Chooz, 80–81
- Earth density profile, *see* PREM
- Earth matter effects, **38, 88**
- Earth radius, 58
- east-west effect, 60
- efficiencies, **63**
  - ATLAS, 66–68, 98
  - Super-Kamiokande, 63–66, 94–98
- efficiency
  - of numerical algorithms, 90
- eigenstates
  - flavour, *see* flavour eigenstates
  - mass, *see* mass eigenstates
- eigensystem
  - of  $3 \times 3$  matrices, 85–88
- energy distribution
  - of events in Super-Kamiokande, 74
- energy resolution
  - ATLAS, 66–68
  - Super-Kamiokande, 63–64
- equal momentum approximation, 14
- experiments
  - accelerator, *see* accelerator experiments
  - reactor, *see* reactor experiments
- far detector, 47, 53
- fiducial volume (in Super-Kamiokande), 94
- flavour eigenstates, 11
- fluxes of atmospheric neutrinos, *see* atmospheric neutrinos
- fully contained events
  - in ATLAS, 74
  - in Super-Kamiokande, **59**, 71, 94–96
- GALLEX, 25
- Gaussian, *see* energy resolution, angular resolution
- geometry
  - of ATLAS, 98
  - of Super-Kamiokande, 94–98
- Gerschgorin’s theorem, 87
- global fits, **27**
- GLOBES, 48, 57
- GNO, 25
- GNU Scientific Library, 85, 90
- Hamiltonian

- in matter, 17, 19
  - in vacuum, 13
  - numerical diagonalization, 85–88
- Homestake, 25
- Householder transformation, 86
- Hyper-Kamiokande, 56, 80–81
- incoherent scattering, 15
- inner detector (of Super-Kamiokande), 94
- INSANE, **57**
- interaction picture, 89, 90
- interdependencies
  - of oscillation probabilities, 21
- inverted hierarchy, 27
- K2K, 24
- KamLAND, 25
- kinematics
  - of neutrino interactions, 64, 67
- Lagrangian, 11, 16
- LAPACK, 85, 90
- $L/E$  analysis, 75
- leptonic CP violation, *see* CP violation
- LHC, 57
- LHCb, 57
- likelihood analysis, 69
- LMA-MSW solution, 25
- LSND, 29
- mantle resonance, 41–42
- mantle-core transition, 39–42
- mass eigenstates, 11
- mass hierarchy, 27
- matter effects, **15**, *see also* MSW-effect
  - in the Earth, **38, 88**
  - in the  $\nu_\mu \rightarrow \nu_e$  channel, 34
  - in the  $\nu_\mu \rightarrow \nu_\tau$  channel, 44
- megaton water Čerenkov detectors, 56
- MEMPHYS, 56
- Mikheyev-Smirnov-Wolfenstein effect, *see* MSW effect
- MINOS, 27, 80–81
- misidentified muons, 71
- MSW effect, 18
- multi-ring events, 66
- muon misidentification, *see* misidentified muons
- muon range, 93–94
- near detector, 47, 53
- neutral current background, 71
- neutrino mass hierarchy, *see* mass hierarchy
- neutrino oscillation probabilities, *see* oscillation probabilities
- neutrino oscillations
  - in matter, **15**, 34, 38, 44, 88
  - in the Earth, 38, 88
  - in vacuum, **11**, 32, 33, 42
- no-oscillation hypothesis, 75
- non-standard neutrino oscillations, 29
- normal hierarchy, 27
- normalization
  - of atmospheric event rates, 68
  - uncertainty, *see* systematical errors
- $\text{NO}\nu\text{A}$ , 27, 80–81
- numerical algorithms, 85
- octant degeneracy, *see* degeneracies
- oscillation channels
  - $\nu_e \rightarrow \nu_e$ , 32
  - $\nu_\mu \rightarrow \nu_e$ , 33
  - $\nu_\mu \rightarrow \nu_\tau$ , 42
- oscillation parameters
  - atmospheric, *see* atmospheric parameters
  - global fit values, 27
  - solar, *see* solar parameters
  - values in our simulations, 49
- oscillation probabilities
  - approximations
    - $\nu_\mu \rightarrow \nu_e$  channel, 35–37, 39–42, 46

- $\nu_\mu \rightarrow \nu_\tau$  channel, 42
- for antineutrinos, 21
- interdependencies, 21
- numerical calculation, 85
- outer detector (of Super-Kamiokande), 94
- overburden
  - of ATLAS, 57
- parameters, *see* oscillation parameters
- partially contained events
  - in Super-Kamiokande, **60**, 71, 96
- performance
  - of numerical algorithms, 90
- photomultipliers (in Super-Kamiokande), 94
- pion decay, 12, 23
- PMNS matrix, 11, **15**
- Poisson distribution, 48, 69
- Pontecorvo-Maki-Nakagawa-Sakata matrix, *see* PMNS matrix
- potential
  - matter, *see* matter effects
- Preliminary Reference Earth Model, *see* PREM
- PREM (Preliminary Reference Earth Model), **38**, 88
- pull terms, *see*  $\chi^2$  analysis
- quasi-elastic scattering, 61
- reactor experiments, 80–81
  - measurement of solar parameters, 25
  - measurement of  $\theta_{13}$ , 27
  - oscillation probability, *see* oscillation channels,  $\nu_e \rightarrow \nu_e$
  - prospects of future, **47**
  - systematical errors, 47
- resolution
  - angular, *see* angular resolution
  - energy, *see* energy resolution
- resonance
  - atmospheric, *see* atmospheric resonance
  - solar, *see* solar resonance
- Runge-Kutta Fehlberg algorithm, 90
- SAGE, 25
- Schrödinger equation, 13
- Schrödinger picture
  - vs. interaction picture, 89, 90
- $\text{sign}(\Delta m_{31}^2)$  degeneracy, *see* Degeneracies
- shape error, *see* systematical errors, reactor spectrum
- simulation, *see also* GLOBES, INSANE
  - atmospheric neutrino experiments, **57**, 93
  - reactor neutrino experiments, **51**
- single meson production, 62
- single-ring events, 66
- smearing, *see* energy resolution, angular resolution
- SNO, 25
- software, *see also* GLOBES, INSANE
- solar activity, 60
- solar neutrino problem, 25
- solar neutrinos, 25
- solar resonance, 19, 26, 35, 44
- spectral uncertainty, *see* systematical errors
- spectrum
  - of atmospheric neutrinos, 60
- spill-in/spill-out effect, 48
- statistical data analysis, *see*  $\chi^2$  analysis
- Steffenson algorithm, 87
- sterile neutrino, 30
- Super-Kamiokande
  - angular resolution, 63–64
  - $\chi^2$  analysis, 68–71
  - efficiencies, 63–66, 94–98
  - energy distribution of events, 74
  - energy resolution, 63–64
  - event samples, 59

- 
- geometry, 94–98
  - observation of solar neutrinos, 25
  - systematical errors, 72
  - target mass, 57
  - track reconstruction, 63–66
  - zenith angle distribution of events, 71–74
  - superbeams, *see* accelerator experiments
  - supernova neutrinos, 29
  - survival probability, *see* oscillation probabilities
  - systematical errors
    - background flux, 48
    - bin-to-bin, 52
    - cancellation, 47
    - correlated vs. uncorrelated, 47
    - detector normalization, 48
    - energy calibration, 48
    - in atmospheric experiments, 70, 72
    - in reactor experiments, 47
    - reactor flux, 48
    - reactor spectrum, 48
    - tilt of the spectrum, 72
  - T2K, 27, 75, 80–81
  - textbook derivation of neutrino oscillation probabilities, 13
  - $\theta_{12}$ , 25, 27
  - $\theta_{13}$ 
    - in accelerator experiments, 27
    - in atmospheric neutrino experiments, 77
    - in reactor experiments, 47
    - Sensitivity vs. discovery reach, 27
  - $\theta_{23}$ , 24, 27, 75–77
  - three-layer approximation, 39, 101
  - tilt errors, *see* systematical errors
  - track
    - minimum length for upward going muons, 66, 97
    - reconstruction in ATLAS, 66–68
    - reconstruction in Super-Kamiokande, 63–66
  - Double Chooz
    - sensitivity to  $\theta_{13}$ , 27
  - Triple Chooz
    - baseline, 54
    - sensitivity to  $\theta_{13}$ , 54
    - target mass, 54
  - triple conspiracy (in atmospheric neutrinos), 55
  - Triple Chooz, 80–81
  - UNO, 56
  - upward stopping muons
    - in Super-Kamiokande, 60, 71, 97–98
  - upward through-going muons
    - in ATLAS, 74, 98
    - in Super-Kamiokande, 60, 74, 97–98
  - water Čerenkov detectors, *see* Super-Kamiokande
  - zenith angle, 58
  - zenith angle distribution
    - of events in ATLAS, 74
    - of events in Super-Kamiokande, 71–74
  - zenith angle resolution, *see* angular resolution



## Bibliography

- [1] T.-P. Cheng and L.-F. Li, *Gauge theory of elementary particle physics*, Clarendon Press, 1984.
- [2] S. Nussinov, *Solar neutrinos and neutrino mixing*, Phys. Lett. **B63** (1976), 201–203.
- [3] B. Kayser, *On the quantum mechanics of neutrino oscillation*, Phys. Rev. **D24** (1981), 110.
- [4] H. Nunokawa, V. B. Semikoz, A. Y. Smirnov, and J. W. F. Valle, *Neutrino conversions in a polarized medium*, Nucl. Phys. **B501** (1997), 17–40, [hep-ph/9701420](#).
- [5] E. K. Akhmedov, *Neutrino physics*, (1999), [hep-ph/0001264](#).
- [6] H. W. Zaglauer and K. H. Schwarzer, *The mixing angles in matter for three generations of neutrinos and the MSW mechanism*, Z. Phys. **C40** (1988), 273.
- [7] M. Maltoni, T. Schwetz, M. A. Tortola, and J. W. F. Valle, *Status of global fits to neutrino oscillations*, New J. Phys. **6** (2004), 122, [hep-ph/0405172](#).
- [8] A. de Gouvea, *The oscillation probability of GeV solar neutrinos of all active species*, Phys. Rev. **D63** (2001), 093003, [hep-ph/0006157](#).
- [9] E. K. Akhmedov, R. Johansson, M. Lindner, T. Ohlsson, and T. Schwetz, *Series expansions for three-flavor neutrino oscillation probabilities in matter*, JHEP **04** (2004), 078, [hep-ph/0402175](#).
- [10] E. K. Akhmedov, P. Huber, M. Lindner, and T. Ohlsson, *T violation in neutrino oscillations in matter*, Nucl. Phys. **B608** (2001), 394–422, [hep-ph/0105029](#).
- [11] Super-Kamiokande, Y. Fukuda et al., *Evidence for oscillation of atmospheric neutrinos*, Phys. Rev. Lett. **81** (1998), 1562–1567, [hep-ex/9807003](#).
- [12] SNO, Q. R. Ahmad et al., *Direct evidence for neutrino flavor transformation from neutral-current interactions in the Sudbury Neutrino Observatory*, Phys. Rev. Lett. **89** (2002), 011301, [nucl-ex/0204008](#).
- [13] C. K. Jung, C. McGrew, T. Kajita, and T. Mann, *Oscillations of atmospheric neutrinos*, Ann. Rev. Nucl. Part. Sci. **51** (2001), 451–488.

- [14] Super-Kamiokande, Y. Ashie et al., *Evidence for an oscillatory signature in atmospheric neutrino oscillation*, Phys. Rev. Lett. **93** (2004), 101801, hep-ex/0404034.
- [15] K2K, E. Aliu et al., *Evidence for muon neutrino oscillation in an accelerator-based experiment*, Phys. Rev. Lett. **94** (2005), 081802, hep-ex/0411038.
- [16] Y. Oyama, *Results from k2k and status of t2k*, (2005), hep-ex/0512041.
- [17] MINOS, D. A. Petit, *First MINOS Results from the NuMI Beam*, 2006.
- [18] B. T. Cleveland et al., *Measurement of the solar electron neutrino flux with the Homestake chlorine detector*, Astrophys. J. **496** (1998), 505–526.
- [19] SAGE, J. N. Abdurashitov et al., *Measurement of the solar neutrino capture rate with gallium metal*, Phys. Rev. **C60** (1999), 055801, astro-ph/9907113.
- [20] GALLEX, W. Hampel et al., *GALLEX solar neutrino observations: Results for GALLEX IV*, Phys. Lett. **B447** (1999), 127–133.
- [21] GNO, M. Altmann et al., *GNO solar neutrino observations: Results for GNO I*, Phys. Lett. **B490** (2000), 16–26, hep-ex/0006034.
- [22] GNO, C. M. Cattadori, *Update of solar neutrino interaction rate measurements from GNO at LNGS*, Nucl. Phys. Proc. Suppl. **110** (2002), 311–314.
- [23] R. Davis, *A review of the Homestake solar neutrino experiment*, Prog. Part. Nucl. Phys. **32** (1994), 13–32.
- [24] SAGE, J. N. Abdurashitov et al., *Measurement of the solar neutrino capture rate by the Russian-American gallium solar neutrino experiment during one half of the 22-year cycle of solar activity*, J. Exp. Theor. Phys. **95** (2002), 181–193, astro-ph/0204245.
- [25] Super-Kamiokande, S. Fukuda et al., *Determination of solar neutrino oscillation parameters using 1496 days of Super-Kamiokande-I data*, Phys. Lett. **B539** (2002), 179–187, hep-ex/0205075.
- [26] SNO, Q. R. Ahmad et al., *Measurement of day and night neutrino energy spectra at SNO and constraints on neutrino mixing parameters*, Phys. Rev. Lett. **89** (2002), 011302, nucl-ex/0204009.
- [27] SNO, S. N. Ahmed et al., *Measurement of the total active B-8 solar neutrino flux at the Sudbury Neutrino Observatory with enhanced neutral current sensitivity*, Phys. Rev. Lett. **92** (2004), 181301, nucl-ex/0309004.

- 
- [28] KamLAND, K. Eguchi et al., *First results from KamLAND: Evidence for reactor anti- neutrino disappearance*, Phys. Rev. Lett. **90** (2003), 021802, hep-ex/0212021.
- [29] KamLAND, T. Araki et al., *Measurement of neutrino oscillation with KamLAND: Evidence of spectral distortion*, Phys. Rev. Lett. **94** (2005), 081801, hep-ex/0406035.
- [30] R. N. Mohapatra and A. Y. Smirnov, *Neutrino mass and new physics*, (2006), hep-ph/0603118.
- [31] H. Minakata, H. Nunokawa, W. J. C. Teves, and R. Zukanovich Funchal, *Reactor measurement of  $\theta_{12}$ : Principles, accuracies and physics potentials*, Phys. Rev. **D71** (2005), 013005, hep-ph/0407326.
- [32] MINOS, E. Ables et al., *P-875: A Long baseline neutrino oscillation experiment at Fermilab*, FERMILAB-PROPOSAL-P-875.
- [33] Y. Itow et al., *The JHF-Kamioka neutrino project*, (2001), hep-ex/0106019.
- [34] NO $\nu$ A, D. S. Ayres et al., *NO $\nu$ A proposal to build a 30-kiloton off-axis detector to study neutrino oscillations in the Fermilab NuMI beamline*, (2004), hep-ex/0503053.
- [35] F. Ardellier et al., *Letter of intent for Double-CHOOZ: A search for the mixing angle  $\theta_{13}$* , (2004), hep-ex/0405032.
- [36] P. Huber, J. Kopp, M. Lindner, M. Rolinec, and W. Winter, *From Double Chooz to Triple Chooz - Neutrino Physics at the Chooz Reactor Complex*, (2006), hep-ph/0601266.
- [37] P. Huber, M. Lindner, and W. Winter, *Simulation of long-baseline neutrino oscillation experiments with GLoBES*, Comput. Phys. Commun. **167** (2005), 195, hep-ph/0407333, <http://www.ph.tum.de/~globes>.
- [38] P. Huber, M. Lindner, M. Rolinec, T. Schwetz, and W. Winter, *Prospects of accelerator and reactor neutrino oscillation experiments for the coming ten years*, Phys. Rev. **D70** (2004), 073014, hep-ph/0403068.
- [39] P. Huber, M. Lindner, M. Rolinec, and W. Winter, *Physics and optimization of beta-beams: From low to very high gamma*, (2005), hep-ph/0506237.
- [40] A. S. Dighe and A. Y. Smirnov, *Identifying the neutrino mass spectrum from the neutrino burst from a supernova*, Phys. Rev. **D62** (2000), 033007, hep-ph/9907423.
- [41] C. Lunardini and A. Y. Smirnov, *Supernova neutrinos: Earth matter effects and neutrino mass spectrum*, Nucl. Phys. **B616** (2001), 307–348, hep-ph/0106149.

- [42] LSND, A. Aguilar et al., *Evidence for neutrino oscillations from the observation of  $\bar{\nu}_e$  appearance in a  $\bar{\nu}_\mu$  beam*, Phys. Rev. **D64** (2001), 112007, [hep-ex/0104049](#).
- [43] Particle Data Group, S. Eidelman et al., *Review of particle physics*, Phys. Lett. **B592** (2004), 1.
- [44] BooNE, E. D. Zimmerman, *BooNE has begun*, eConf **C0209101** (2002), TH05, [hep-ex/0211039](#).
- [45] M. Blennow, T. Ohlsson, and W. Winter, *Non-standard Hamiltonian effects on neutrino oscillations*, (2005), [hep-ph/0508175](#).
- [46] P. Huber, T. Schwetz, and J. W. F. Valle, *Confusing non-standard neutrino interactions with oscillations at a neutrino factory*, Phys. Rev. **D66** (2002), 013006, [hep-ph/0202048](#).
- [47] A. M. Dziewonski and D. L. Anderson, *Preliminary reference earth model*, Phys. Earth Planet. Interiors **25** (1981), 297–356.
- [48] R. Gandhi, P. Ghoshal, S. Goswami, P. Mehta, and S. Uma Sankar, *Earth matter effects at very long baselines and the neutrino mass hierarchy*, (2004), [hep-ph/0411252](#).
- [49] R. Gandhi, P. Ghoshal, S. Goswami, P. Mehta, and S. Uma Sankar, *Large matter effects in  $\nu_\mu \rightarrow \nu_\tau$  oscillations*, Phys. Rev. Lett. **94** (2005), 051801, [hep-ph/0408361](#).
- [50] R. Gandhi, P. Ghoshal, S. Goswami, P. Mehta, and S. Uma Sankar, *Probing the  $\nu$  mass hierarchy via atmospheric  $\nu_\mu + \bar{\nu}_\mu$  survival rates in Megaton water Cherenkov detectors*, (2005), [hep-ph/0506145](#).
- [51] C. L. Cowan Jr., F. Reines, F. B. Harrison, H. W. Kruse, and A. D. McGuire, *Detection of the free neutrino: A confirmation*, Science **124** (1956), no. 3212, 103–104.
- [52] C. L. Cowan and F. Reines, *The Neutrino*, Nature **178** (1956), no. 446.
- [53] P. Huber, M. Lindner, T. Schwetz, and W. Winter, *Reactor neutrino experiments compared to superbeams*, Nucl. Phys. **B665** (2003), 487–519, [hep-ph/0303232](#).
- [54] K. Nakamura, *Hyper-Kamiokande: A next generation water Cherenkov detector*, Int. J. Mod. Phys. **A18** (2003), 4053–4063.
- [55] A. de Bellefon et al., *MEMPHYS: A large scale water Čerenkov detector at Fréjus*, Contribution to the CERN strategic committee, [http://apc-p7.org/APC\\_CS/Experiences/MEMPHYS/](http://apc-p7.org/APC_CS/Experiences/MEMPHYS/).

- 
- [56] C. K. Jung, *Feasibility of a next generation underground water Cherenkov detector: UNO*, (1999), hep-ex/0005046.
- [57] P. Huber, M. Maltoni, and T. Schwetz, *Resolving parameter degeneracies in long-baseline experiments by atmospheric neutrino data*, Phys. Rev. **D71** (2005), 053006, hep-ph/0501037.
- [58] Super-Kamiokande, Y. Ashie et al., *A measurement of atmospheric neutrino oscillation parameters by Super-Kamiokande I*, Phys. Rev. **D71** (2005), 112005, hep-ex/0501064.
- [59] M. Honda, T. Kajita, K. Kasahara, and S. Midorikawa, *A new calculation of the atmospheric neutrino flux in a 3- dimensional scheme*, Phys. Rev. **D70** (2004), 043008, astro-ph/0404457.
- [60] G. Battistoni, A. Ferrari, T. Montaruli, and P. R. Sala, *The FLUKA atmospheric neutrino flux calculation*, Astropart. Phys. **19** (2003), 269–290, hep-ph/0207035.
- [61] G. D. Barr, T. K. Gaisser, P. Lipari, S. Robbins, and T. Stanev, *A three-dimensional calculation of atmospheric neutrinos*, Phys. Rev. **D70** (2004), 023006, astro-ph/0403630.
- [62] P. Lipari, *The geometry of atmospheric neutrino production*, Astropart. Phys. **14** (2000), 153–170, hep-ph/0002282.
- [63] T. K. Gaisser and M. Honda, *Flux of atmospheric neutrinos*, Ann. Rev. Nucl. Part. Sci. **52** (2002), 153–199, hep-ph/0203272.
- [64] M. Honda, T. Kajita, K. Kasahara, and S. Midorikawa, *Calculation of the flux of atmospheric neutrinos*, Phys. Rev. **D52** (1995), 4985–5005, hep-ph/9503439.
- [65] T. K. Gaisser, T. Stanev, and G. Barr, *Cosmic ray neutrinos in the atmosphere*, Phys. Rev. **D38** (1988), 85.
- [66] M. D. Messier, *Evidence for neutrino mass from observations of atmospheric neutrinos with Super-Kamiokande*, UMI-99-23965.
- [67] E. A. Paschos and J. Y. Yu, *Neutrino interactions in oscillation experiments*, Phys. Rev. **D65** (2002), 033002, hep-ph/0107261.
- [68] Super-Kamiokande, T. Kajita et al., private communication.
- [69] P. Huber, M. Lindner, M. Rolinec, T. Schwetz, and W. Winter, *Combined potential of future long-baseline and reactor experiments*, Nucl. Phys. Proc. Suppl. **145** (2005), 190–193, hep-ph/0412133.

- [70] M. Rolinec, private communication.
- [71] Super-Kamiokande, *Three flavor neutrino oscillation analysis of atmospheric neutrinos in Super-Kamiokande*, (2006), [hep-ex/0604011](#).
- [72] P. Huber, M. Lindner, and W. Winter, *Superbeams versus neutrino factories*, Nucl. Phys. **B645** (2002), 3–48, [hep-ph/0204352](#).
- [73] M. Galassi et al., *GNU Scientific Library Reference Manual*, second ed.
- [74] E. Anderson, Z. Bai, C. Bischof, S. Blackford, J. Demmel, J. Dongarra, J. Du Croz, A. Greenbaum, S. Hammarling, A. McKenney, and D. Sorensen, *LAPACK users' guide*, third ed., Society for Industrial and Applied Mathematics, Philadelphia, PA, 1999.
- [75] J. Stoer, *Einführung in die Numerische Mathematik*, fourth ed., Springer-Verlag, 1983.
- [76] W. H. Press, B. P. Flannery, S. A. Teukolsky, and W. T. Vetterlin, *Numerical Recipes in C*, Cambridge University Press, 1988.
- [77] J. Stoer and R. Bulirsch, *Einführung in die Numerische Mathematik II*, second ed., Springer-Verlag, 1978.
- [78] D. E. Groom, N. V. Mokhov, and S. I. Striganov, *Muon stopping power and range tables 10-MeV to 100-TeV*, Atom. Data Nucl. Data Tabl. **78** (2001), 183–356.